ABSTRACT

A MEASUREMENT OF THE POLARIZATION PARAMETER IN NEUTRON-PROTON CHARGE EXCHANGE SCATTERING FROM 2-12 GeV/c

Ву

Randal Charles Ruchti

This dissertation describes an experimental measurement of the polarization parameter in neutron-proton charge exchange scattering for incident momenta 2-12 GeV/c and four momentum transfers $0.01 \le |t| \le 1.0 \text{ (GeV/c)}^2$. Using a polarized target and a two-arm spectrometer, a sample of 1.1×10^7 triggers was collected from which 3×10^5 elastic events were extracted with a 3-constraint fit. The results show a polarization whose magnitude increases monotonically with |t| to roughly 60% for $|t| \ge 0.6 \text{ (GeV/c)}^2$ and which has relatively little energy dependence. A detailed comparison of the data with several current phenomenological models is made.

A MEASUREMENT OF THE POLARIZATION PARAMETER IN NEUTRON-PROTON CHARGE EXCHANGE SCATTERING FROM 2-12 GeV/c

Ву

Randal Charles Ruchti

A THESIS

Submitted to
Michigan State University
in partial fulfillment of the requirements
for the degree of

DOCTOR OF PHILOSOPHY

Department of Physics

1973



ACKNOWLEDGMENTS

Since a high energy physics experiment is truly a group effort, there are a number of people whom I wish to thank for their contributions or assistance: First I would like to thank my adviser Maris Abolins for his able leadership as spokesman for this experiment and for his guidance, encouragement, and friendship during my graduate career; second, I would like to thank fellow graduate student Jay Horowitz for his many contributions to experimental effort and data analysis; third I would like to thank Bill Reay for many helpful discussions on both phenomenology and experimental techniques, Noel Stanton for discussions on fast electronics, Ron Kammerud for discussions on chambers, Jon Pumplin for discussions on phenomenology, and M. T. Lin, Ken Edwards, Ed Miller, Kurt Reibel, Don Crabb, and John O'Fallon for their part in the experiment and for helpful discussions on hardware; and lastly, I would like to thank my wife Peggy for her support through the course of this work.

TABLE OF CONTENTS

																		Page
LIST OF TABL	ES			•		•		•	•	•	•	•	•	•	•	•	•	v
LIST OF FIGU	RES	•		•		•		•	•	•	•	•	•	•	•	•	•	vi
	MOTI INTR			-								D	•	•	•	•	•	1
II.	THE	EXP	ERIM	ENI	AL	CON	FIG	UR/	ATI	ON	•		•	•		•	•	7
	Α.	Inc	ider	nt E	eam			•	•	•	•		•	•	•	•	•	7
		2. I	3ean	n Cr	l M coss rge	Se	cti	on	Mo	ni	tc	r	•	•		•	•	10 12 14
:	В.	The	Pol	lari	zed	Ta	rge	t	•	•	•	•	•	•	•	•	•	17
		1. l 2. l			sms ed									•	•	•	•	17 22
		1	o. 7 c. 7 d. M	The The Micr	Gly Cry Mag Owa Det	ost net ve	at Sys	ter	n	•	•	•	•	•	•	•	•	22 24 26 26 26
(C.	The	Two	-Ar	m S	pec	tro	met	ter	•	•	•	•	•	•	•	•	33
•		1. 2. 3.	The	e Ne	roto eutr empl	on	Arm			•	•	•	•	•	•	•	•	33 37 39
III.	DATA	CO	LLEC	CTIC	N A	ND	AN A	LY	SIS		•		•	•	•	•	•	41
	Α.	The	On-	-lir	ne A	nal	ysi.	s	•	•	•	•	•	•	•	•	•	41
]	В.	The	Off	?-li	ne .	Ana	lys	is	•	•	•	•	•	•	•	•	•	44
	C.	The	Po]	lari	.zat	ion	Ca	lcı	ala	ti	on	l	•	•	•	•	•	47

CHAPTER			Page
	D.	Checks of the Data	50
		 Checks of the Experimental Measurement	50 57
		function of x^2	57
		4. Checks on consistency with other experiments	62
IV.	PRE	SENTATION OF THE DATA	69
v.	THE	ORETICAL INTERPRETATION	79
	Α.	Preliminaries	79
	В.	Models	82
		1. Elastic Amplitudes	84 85
VI.	CON	CLUSIONS OF THE EXPERIMENT	101
	Α.	Experimental Implication	101
	В.	Theoretical Implication	101
APPENDIX A.		KINEMATICS FOR THE n+p + p+n SYSTEM	102
APPENDIX B.		NMR POLARIZATION CALCULATION	107
APPENDIX C.		WIRE CHAMBER SPECIFICATION	110
APPENDIX D.		NEUTRON COUNTER SPECIFICATION	113
APPENDIX E.		PROTON MOMENTUM ANALYSIS	120
APPENDIX F.		FERMI MOMENTUM CONSIDERATIONS	122
APPENDIX G.		THEORY APPENDIX	124
APPENDIX H.		APPROXIMATE BEAM SPECTRUM	128
APPENDIX I.		PPT-II FIELD MAP	131
BIBLIOGRAPH	Υ.		133

LIST OF TABLES

TABLE				Page
1	Table of Percentage Backgrounds in the Neutron Counters as a Function of $ t $	•		. 48
2	Table of Polarization Data	•	•	. 70
3	Table of Results of Phenomenological Models	•	•	. 100
C-1	Wire Spark Chamber Specifications	•	•	. 111
E-1	Polynomial for Proton Momentum Determination	•	•	. 121

LIST OF FIGURES

FIGURE		Page
1	Definition of the Convention of the Normal to the Scattering Plane, $\hat{n} = (\vec{P}_1 \times \vec{P}_4) / \vec{P}_1 \times \vec{P}_4 ; z$ is the Beam Direction; y is the Target Quantization Axis	3
2	Polarization Data from Reference 1 and a Comparison with the SCRAM Model	4
3	Differential Cross Section Data from Reference 5 and Comparison with the SCRAM Model	6
4	The Experimental Layout	8
5	The 7° Neutral Beam Line	9
6	Beam Mapper Configuration and Beam Maps	13
7	X-Ray Source Configuration	16
8	Target Location Reconstructed from Straight Through Tracks into the Upstream Chambers	16
9	"Solid Effect" Energy Level Diagram	19
10	Polarized Target Cryostat	23
11	Cryogenic Systems	25
12	Target Temperature Vs. Cavity Vapor Pressure	25
13	Microwave Plumbing Arrangement	27
14	NMR Detector Circuit Diagram	29
15	NMR System Schematic	32

FIGURE		Page
16	Pulse Height Distributions for S1 and S2 Counters	34
17	Proton Arm Logic	36
18	Neutron Arm Logic	38
19	Two Arm Logic	40
20a	On-line Constraints for Px, Py, and Opening Angle	. 42
20b	On-line Constraint for Py Balance with Graphite Dummy Target Data Shaded	. 43
21a	Fitted Event χ^2 Distributions for Both Glycol and Graphite Samples for Short Counters	, 45
21b	Fitted Event χ^2 Distributions for Both Glycol and Graphite Samples for Long Counters	, 46
22a	Neutron Counter Consistency in the Region of Overlap for the Short Counters	, 52
22b	Neutron Counter Consistency in the Region of Overlap for the Long and Short Counters	53
23	Uniformity of Polarization in the Target	. 54
24	Comparison of the Polarization Parameter Values, Calculated for Each of the Data Taking Periods Individually: Phase I (Sept-Oct., 1971) and Phase II	
	(Nov-Dec., 1971)	, 56
25	Experimental t -Resolution	. 58
26	Polarization Parameter Plotted for Two Different Binning Schemes: (a) Actual Scheme used, (b) Complementary Scheme	. 59
27	$(NN+)$ vs χ^2 for $0 \le \chi^2 \le 50$. The Factor $(NN+)$ is Essentially P ₀ Except for Normalization	. 60
28	$P_0 \text{ vs } \chi^2 \text{ for } \chi^2 \le 2, 4, 6, 8, 10 \dots$	61

FIGURE		Pε	age
29	Po Calculated By Two Different Methods: (a) Method Shown in Chapter IV, (b) Method Used in Reference 25		63
30	Comparison of the Polarization with Previous Work: (a) This Experiment, (b) Data From Reference 1	•	64
31	Comparison of the Differential Cross Section with Previous Work: (a) Approximate Cross Section from this Experiment, (b) Data From Reference 5	•	67
32	$P_{O}(t)$ vs t for 2 \leq $P_{LAB} \leq$ 4 GeV/c	•	71
33	$P_{O}(t)$ vs t for 4 $\stackrel{\checkmark}{-}$ $P_{LAB} \stackrel{\checkmark}{-}$ 6 GeV/c	•	72
34	$P_{O}(t)$ vs t for 6 $\stackrel{<}{-}$ $P_{LAB} \stackrel{<}{-}$ 8 GeV/c	•	73
35	$P_{O}(t)$ vs t for 8 \leq $P_{LAB} \leq$ 10 GeV/c	•	74
36	$P_O(t)$ vs t for 10 $\stackrel{\checkmark}{-}$ $P_{LAB} \stackrel{\checkmark}{-}$ 12 GeV/c	•	75
37	Approximate Energy Variation of $P_{O}(t)$ as P_{LAB} Increases From 2-12 GeV/c	•	76
38	$P_O(P_{LAB})$ vs P_{LAB} for $0.01 \le t \le 1.0$	•	77
39	P _O (P _{LAB} ,t) vs P _{LAB} and t , Showing Experimental Acceptance		7 8
40	Helicity Picture for n+p → p+n	•	81
41	Helicity Amplitude Expansion in Terms of Particle Exchange	•	81
42	Fits to d_{σ}/dt with Various Choices of $m^{\text{eff}}(s,t)$	•	86
43	How Absorption Modifies a Helicity Amplitude	•	86
44	V-M Fits to $d\sigma/dt (n+p \rightarrow p+n) \dots$	•	90
45	V-M Fits to $P_0(n+p \rightarrow p+n)$	•	91
46	V-M Fits to $d\sigma/dt (\bar{p}+p \rightarrow \bar{n}+n)$	•	92

FIGURE		Page
47	V-M Prediction for $P_0(\bar{p}+p \rightarrow \bar{n}+n)$	93
48	Argand Plots of \$\psi_5^*\$ and \$\phi_0\$ for the SCRAM Model	94
49	Argand Plots of \$\displaystyle{5}{5}\$ and \$\displaystyle{6}{5}\$ for the V-M Model	95
50	HKV Fit to $d\sigma/dt$ (nip \rightarrow p+n)	96
51	HKV Fit to $P_0(n+p \rightarrow p+n)$	97
52	HKV Fit to d σ /dt (\bar{p} +p \rightarrow \bar{n} +n)	98
53	HKV Prediction to $P_0(\bar{p}+p \bar{n}+n)$	99
A-1	Scattering in the Center of Momentum Frame	104
A-2	Scattering in the Laboratory Frame	104
A-3	Coordinate Systems Used to Describe Particle Momenta: (a) Spherical Coordinates, (b) On-line Constraint Variables, (c) Off-line Variables. The Reference Axes are: x̂, Toward Neutron Arm; ŷ, the PPT Magnetic Field Axis; ẑ, the Surveyed Beam Direction	106
C-1	Proton Arm Resolution	112
D-1	Neutron Counter Acceptance, A(PLAB,t)	115
D - 2	Target Absorption Function for Neutrons, T(t)	116
D-3	Neutron Counter Detection Efficiency, E(t)	117
D-4	Neutron Arm Resolution	118
D-5	Neutron Counter Design	119
E-1	Polynomial Coordinates	121
H-1	Neutron Beam Spectrum, I(PLAB)	129
H-2	Neutron Beam Resolution	130
I-1	PPT-II Magnetic Field Map for H = 25kG	132

CHAPTER I

MOTIVATION FOR THE EXPERIMENT AND INTRODUCTION TO EXISTING DATA

In neutron-proton charge exchange scattering, both the incident and target nucleons have spin 1/2, and one expects polarization effects to influence the final state distribution of events. A typical method for experimentally measuring the polarization parameter is to use an unpolarized neutron beam and a polarized proton target.

At the Argonne Zero Gradient Synchrotron, the neutron beam has a broad momentum spectrum which depends on production angle and is usually contaminated with Y-rays and a few K_L mesons. The polarized target, which consists of glycol or similar organic material as well as a cryostat structure, generates a large background of events from the diversity of material present. These complications can be accommodated nicely however, first by careful collimation and filtration of the incident beam, and second by using a two-arm spectrometer which measures completely the four-momenta of the final state particles.

The yield of events from a polarized target is given by

$$\frac{d\sigma}{dt} = \frac{d\sigma}{dt} \cdot (1 + \vec{T} \cdot \hat{n}P_0)$$

where $(d\sigma/dt)_0$ is the unpolarized differential cross section, $\stackrel{\rightarrow}{T}$ is the target polarization, \hat{n} is the normal to the scattering plane specified by convention, and P_0 is the polarization parameter. The direction \hat{n} is chosen as

$$\hat{n} = (\hat{P}_1 \times \hat{P}_4)/|\hat{P}_1 \times \hat{P}_4|$$

where $\vec{P_1}$ and $\vec{P_4}$ are the incident and outgoing neutron momenta respectively (see Figure 1 and Appendix A), a choice which is consistent with that of np elastic scattering. The polarization parameter is a measure of the asymmetry exhibited by the distribution of final state events when the target polarization \vec{T} is parallel (+) and antiparallel (+) to the vector \hat{n} :

$$P_{O} = \frac{1}{|\vec{T}|} \quad \frac{\frac{dg}{dt} + - \frac{dg}{dt} +}{\frac{dg}{dt} + \frac{dg}{dt} +}$$

There exists only one previous set of measurements of the polarization parameter, 1 covering a momentum domain 1-5 GeV/c; the data are shown in Figure 2. The same convention for \hat{n} was used, and the polarization values obtained were consistent with zero in the forward direction and monotonically decreasing with |t| to |t| ~.5, the acceptance limit. Over the measured energy range, the polarization parameter was approximately independent of energy. The data have interesting implications for theory, and although a detailed discussion of phenomenology is deferred until chapter 5, there are some salient features worth mentioning here.

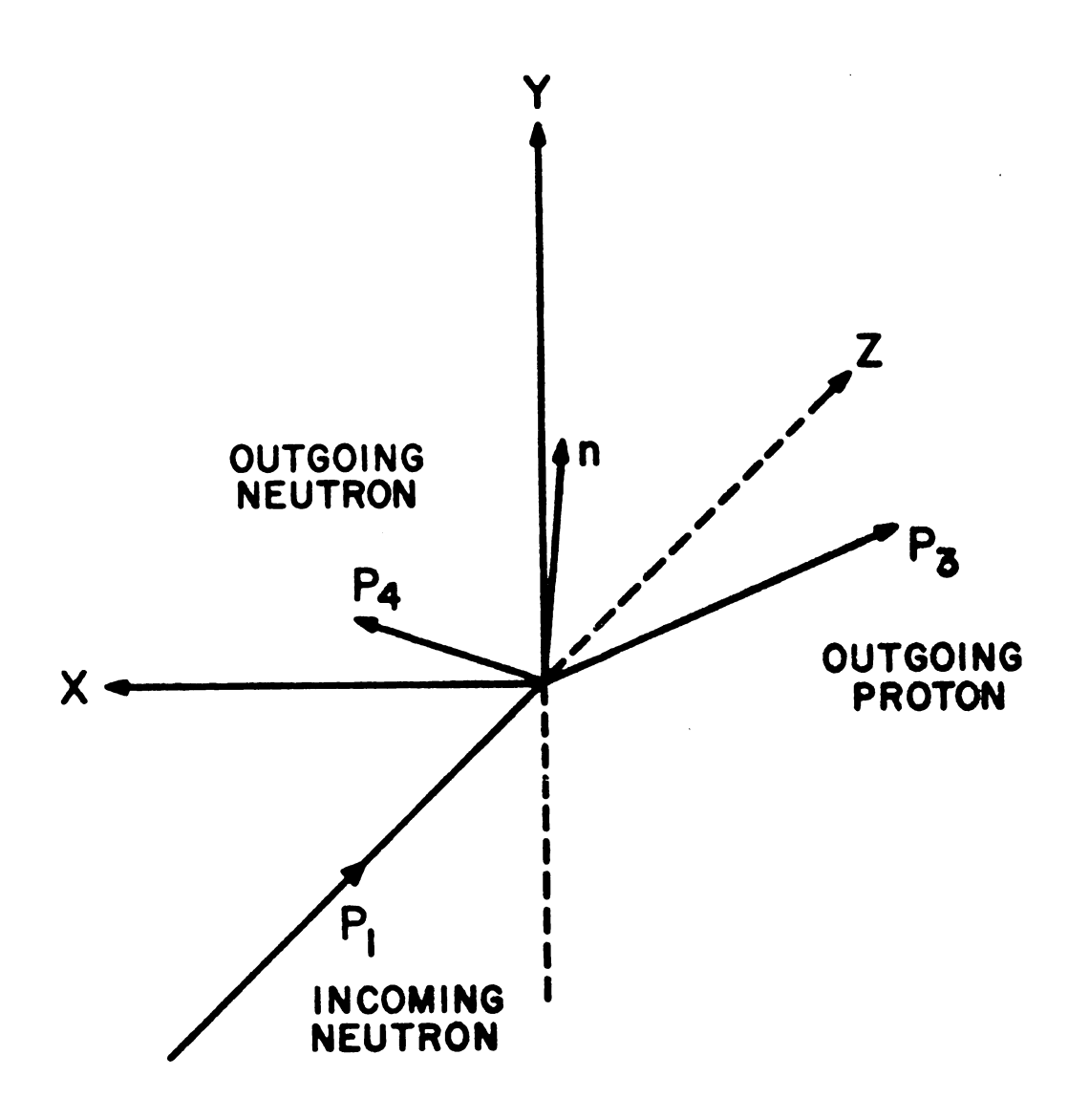
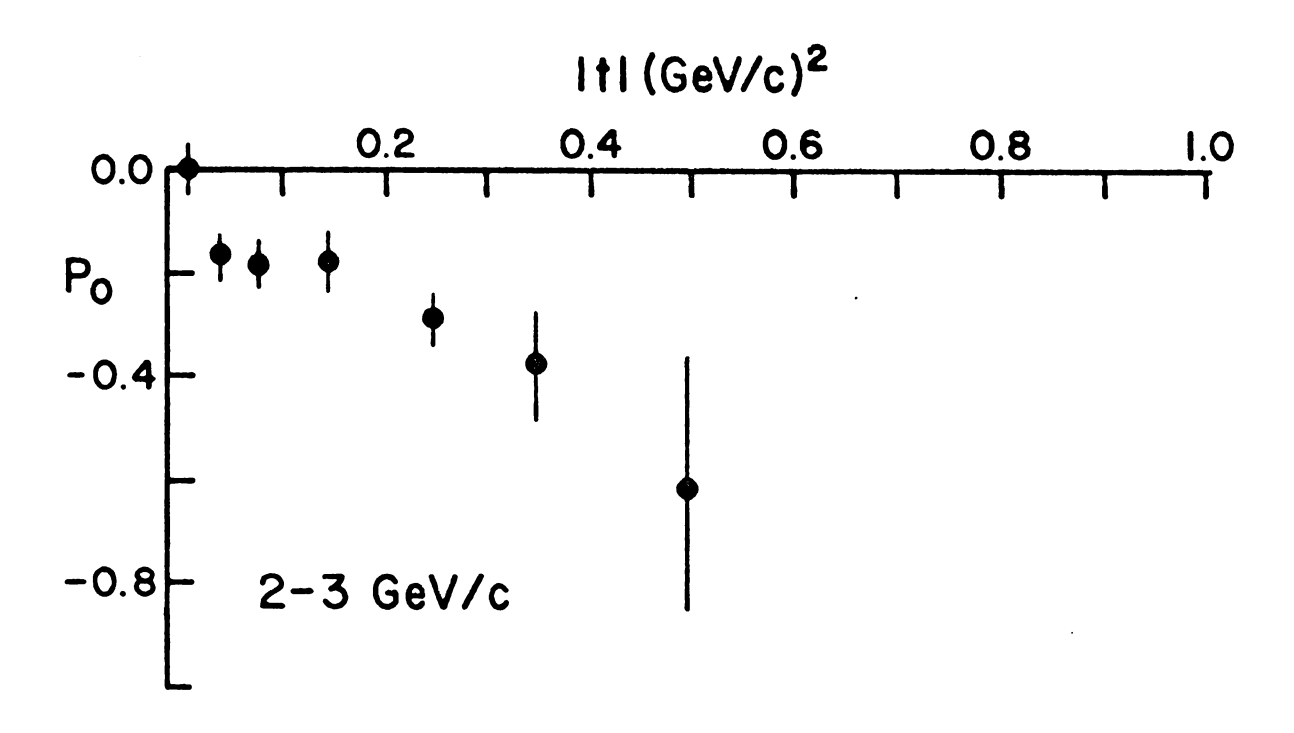


Figure 1. Definition of the Convention of the Normal to the Scattering Plane, $\hat{n} = (\vec{P}_1 \times \vec{P}_4) / |\vec{P}_1 \times \vec{P}_4|; \text{ z is the Beam Direction; y is the Target Quantization Axis.}$



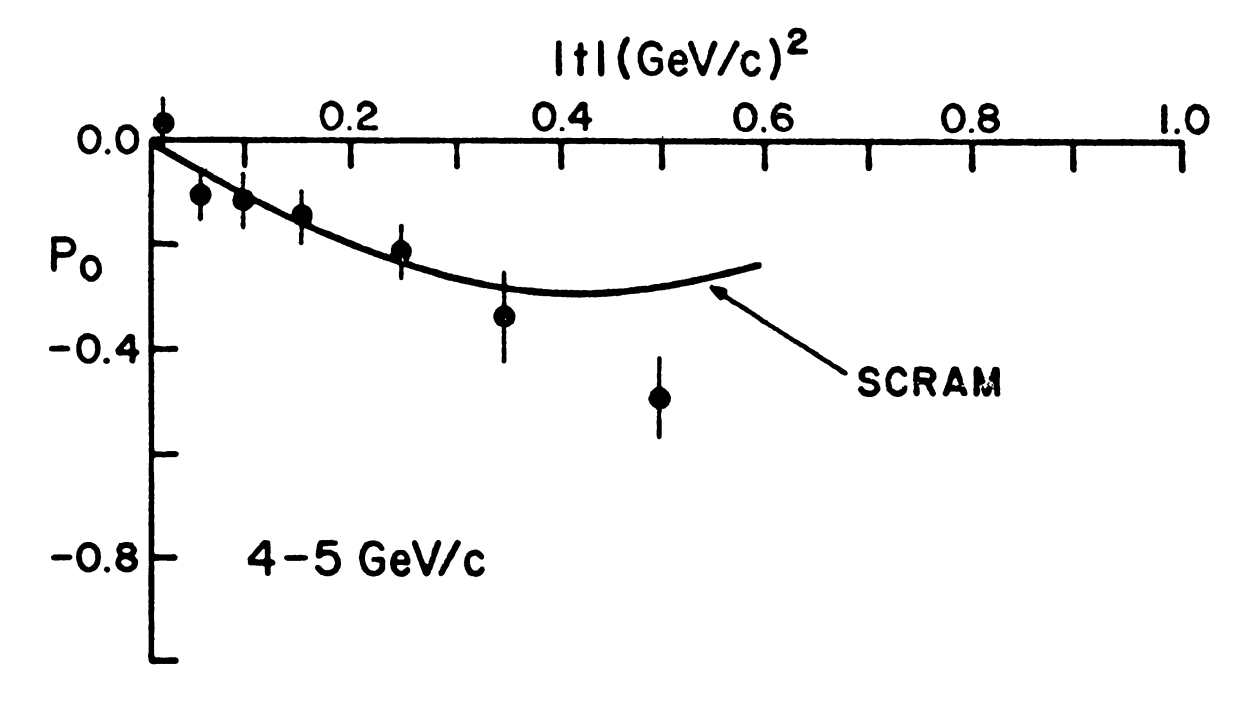


Figure 2. Polarization Data from Reference 1 and a Comparison with the SCRAM Model.

A non-zero polarization requires contributions from ρ and A_2 exchange (and possibly lower lying trajectories) in the $n+p \rightarrow p+n$ reaction. Using these as well as π - exchange, a recent model, the Strong Cut Reggeized Absorption Model (SCRAM), was able to follow the trend of the Robrish data out to a |t| of roughly 0.5 (GeV/c) where the data ended. SCRAM was also able to fit the differential cross section for $|t| \le 0.4$ (GeV/c) but proved to be in error for larger momentum transfers (see Figure 3).

A polarization measurement with broad energy and momentum transfer coverage would provide a better test of phenomenology -- especially in the interesting region $0.4 \le |t| \le 1.0 (\text{GeV/c})^2$, and could determine if the apparent energy independence of the polarization parameter persists for higher incident momenta. This dissertation describes such an experiment, the measurement of the polarization parameter in np charge exchange scattering for incident neutron momenta 2-12 GeV/c and four-momentum transfers $0.01 \le |t| \le 1.0 (\text{GeV/c})^2$, the particulars of which are now discussed.

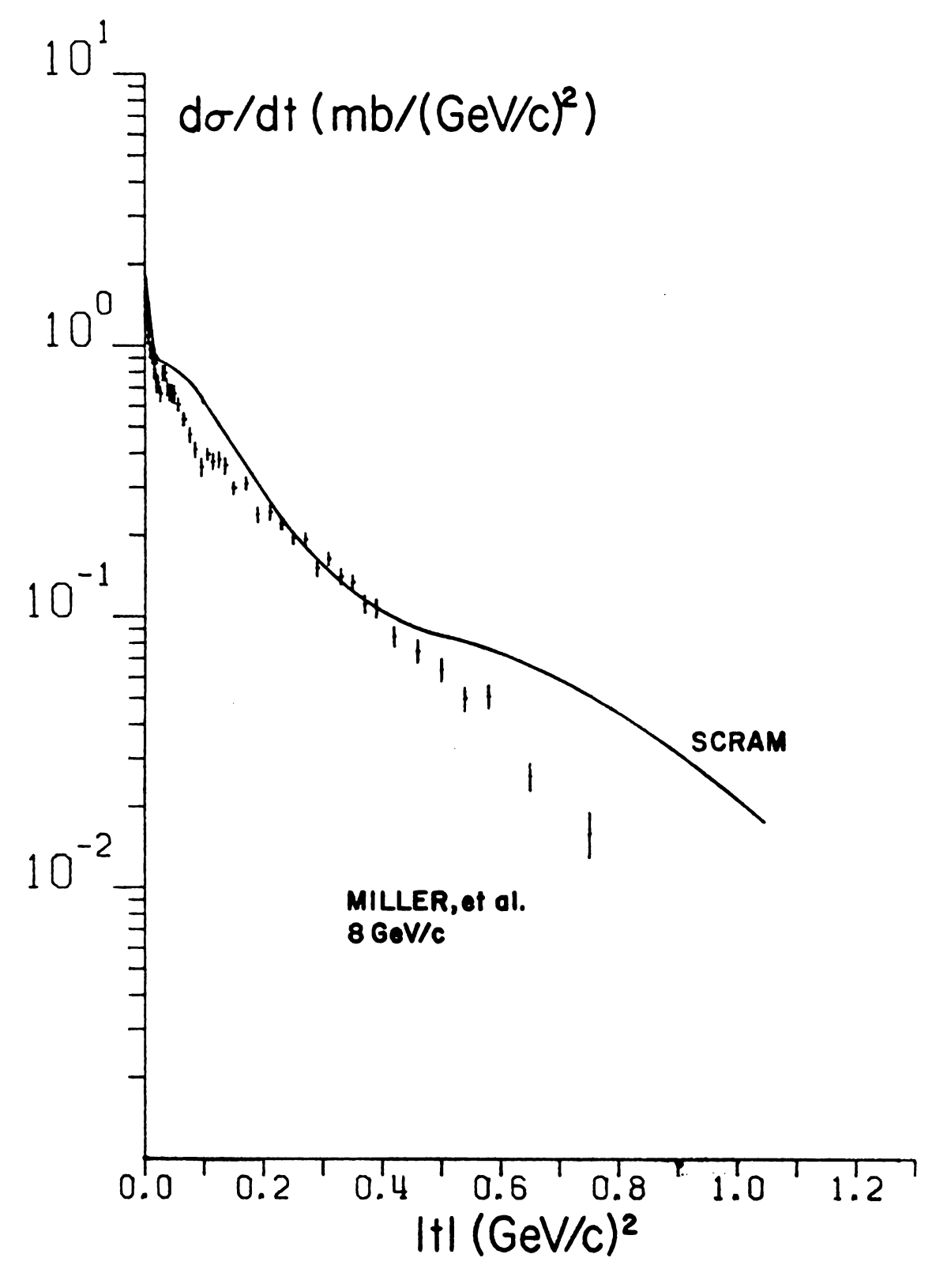


Figure 3. Differential Cross Section Data from Reference 5 and Comparison with the SCRAM Model

CHAPTER II

THE EXPERIMENTAL CONFIGURATION

Before covering the details of the apparatus a brief summary of the experimental arrangement is appropriate (see Figure 4). A neutron beam of broad momentum spectrum was incident on a polarized target. Of the initial particles only the four-momentum of the target proton $(m_2, 0)$ was known (see Appendix A for kinematics). The final state neutron and proton were detected by a conventional two-arm spectrometer which completely measured their three-momenta. This information allowed us to make a 3-constraint fit on our data sample, permitting a clean separation of elastic events from background.

A. Incident Beam

The experiment was performed in the 7° neutral beam at the Argonne ZGS (see Figure 5). By scraping the circulating proton beam with a 0.25" long beryllium target, a beam of neutrons was produced at 3/4° with a broad momentum spectrum peaked near 11 GeV/c⁷, 8 (see Appendix H). This targeting scheme produced roughly 10 neutrons per 4 x 10¹¹ protons incident on the internal target. The external beam was cleared of charged contaminants by several sweeping

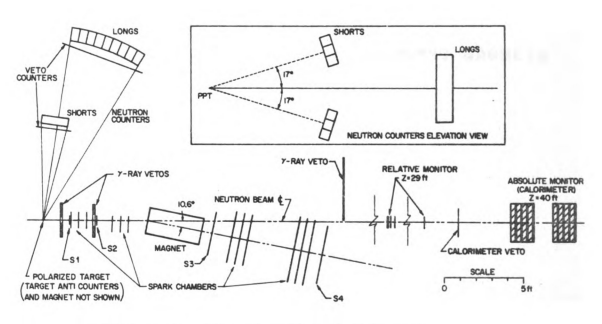


Figure 4. The Experimental Layout.

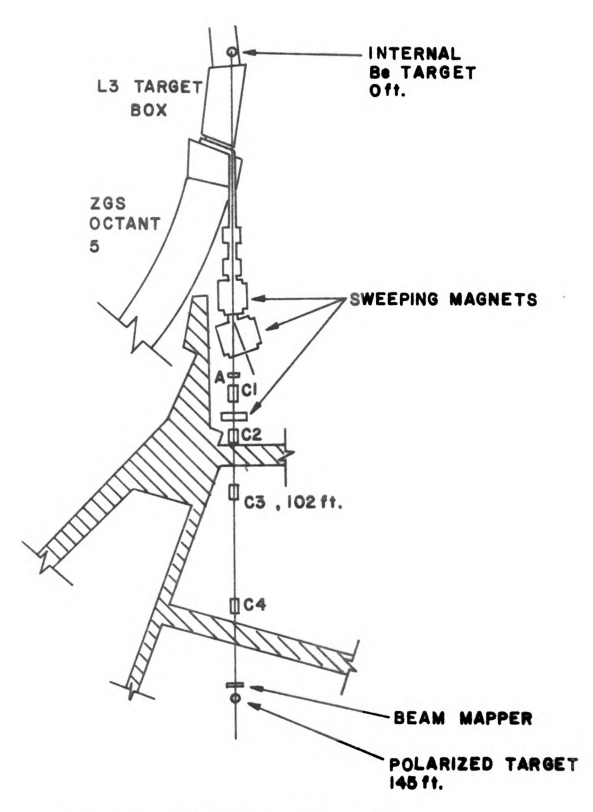


Figure 5. The 7° Neutral Beam Line

magnets and passed through a γ-ray filter (A) of two radiation lengths of lead. Laterally the beam was shaped by four overdefining collimators (C1-C4), creating a 0.94 x 1.25 in² spot at the position of the polarized target, 145 ft. downstream of the internal ring target. To reach the polarized target, the neutron beam passed through a hole in the PPT magnet yoke. This scheme allowed optimal placement of detectors around the target cryostat.

Two characteristics of the beam were important: First a measurement of the total neutron flux was required for event normalization; second a cross sectional map of the beam was required just upstream of the target to make certain that the beam and target were matched and to assure that no obstructions lay in the beam, casting shadows in the target vicinity. To measure these characteristics several counter arrangements were used.

1. Integral Monitors

The simplest method of measuring intensity is to stop the entire beam in some thick converter and detect conversion products in scintillation counters. However high beam rates and high inelasticity of the interactions in the detector produce a rate dependence in this type of monitor. An alternative is to put a thin converter into the beam and sample a fraction of the neutrons. Since counting rates are much lower the rate problem is avoided, but the low detection efficiency for neutrons requires that this type of monitor be continuously checked relative to some measure of the total flux

to guard against changes in beam characteristics. The problem is resolved by using both types of monitors.

The first relative monitor OMON consisted of three 0.25 x 6 x 6 in scintillators. The counter OM1 served as charged particle veto; counters OM2 and OM3 detected conversion products from a .25 in. thick aluminum sheet placed upstream of OM2. Omon logic was satisfied if OMON=OM1·OM2·OM3 obtained. Typical counting rates were 2.5 K per ZGS pulse and neutron detection efficiency was ~ 2%.

By including into coincidence with OMON an additional $0.25 \times 6 \times 6$ in 3 counter OM4 located 60 in. downstream of OM1, the relative monitor HIMON was formed: HIMON=OMON·OM4. The longer axial length of the conversion telescope allowed sensitivity to beam neutrals of higher momenta since only highly collimated interaction products could satisfy the logic. As it monitored a more limited region of the momentum spectrum, its ratio relative to OMON was an indication of internal targeting changes.

The final integral monitor was the calorimeter which was designed to detect beam neutrons with 98% efficiency. It consisted of eight 3.25 x 25 x 25 in layers of iron and 0.375 x 25 x 25 in layers of scintillator forming a giant sandwich. Just upstream of the apparatus was placed an 0.375 x 25 x 25 in scintillation veto counter to guarantee that only conversions from incident neutrals would be counted within the calorimeter volume. The calorimeter logic was defined as: $CAL=\overline{CA}\cdot(C1+C3+C5+C7)\cdot(C2+C4+C6+C8)$ which specified

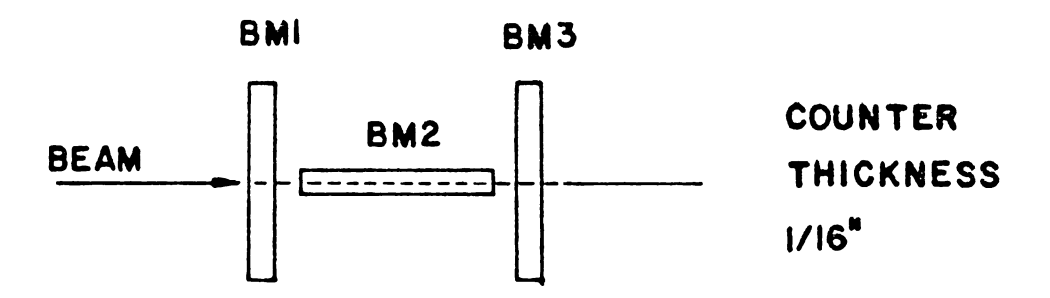
a 3.25 in. minimum range for charged conversion products from an n-Fe interaction. To minimize the anticipated rate problem, the photomultiplier pulses were clipped short right at the counter. Reflection problems from the clipping were minimized by attenuating the signals input to the calorimeter fast logic and by raising the discriminator levels on each of the units to reject low pulses. Typical counting rates for CAL were 1.1×10^5 per ZGS pulse.

The calibration of OMON relative to CAL was performed at low beam intensity to avoid any rate dependence in CAL. Then the ratios CAL/OMON and HIMON/OMON provided the stability criterion for the relative monitor OMON, and OMON was used as the normalization for the experimental events.

2. Beam Cross Section Monitor

At a location six feet upstream of the polarized target, the relative magnitude and lateral extent of the beam were measured with a beam mapper, a mechanically moveable telescope of three 0.063 x l x 4 in³ scintillation counters arranged as shown in Figure 6. The upstream counter BM1 acted as a charged particle veto; counter BM2 was itself the converter and, coupled with BM3, formed the conversion telescope: BM=BM1·BM2·BM3. The telescope was moved horizontally and vertically through the beam, and profiles were recorded (see Figure 6).

Once a profile was taken, the counter telescope was positioned at the nominal beam center with a transit or level scope. The spatial distance between this point and



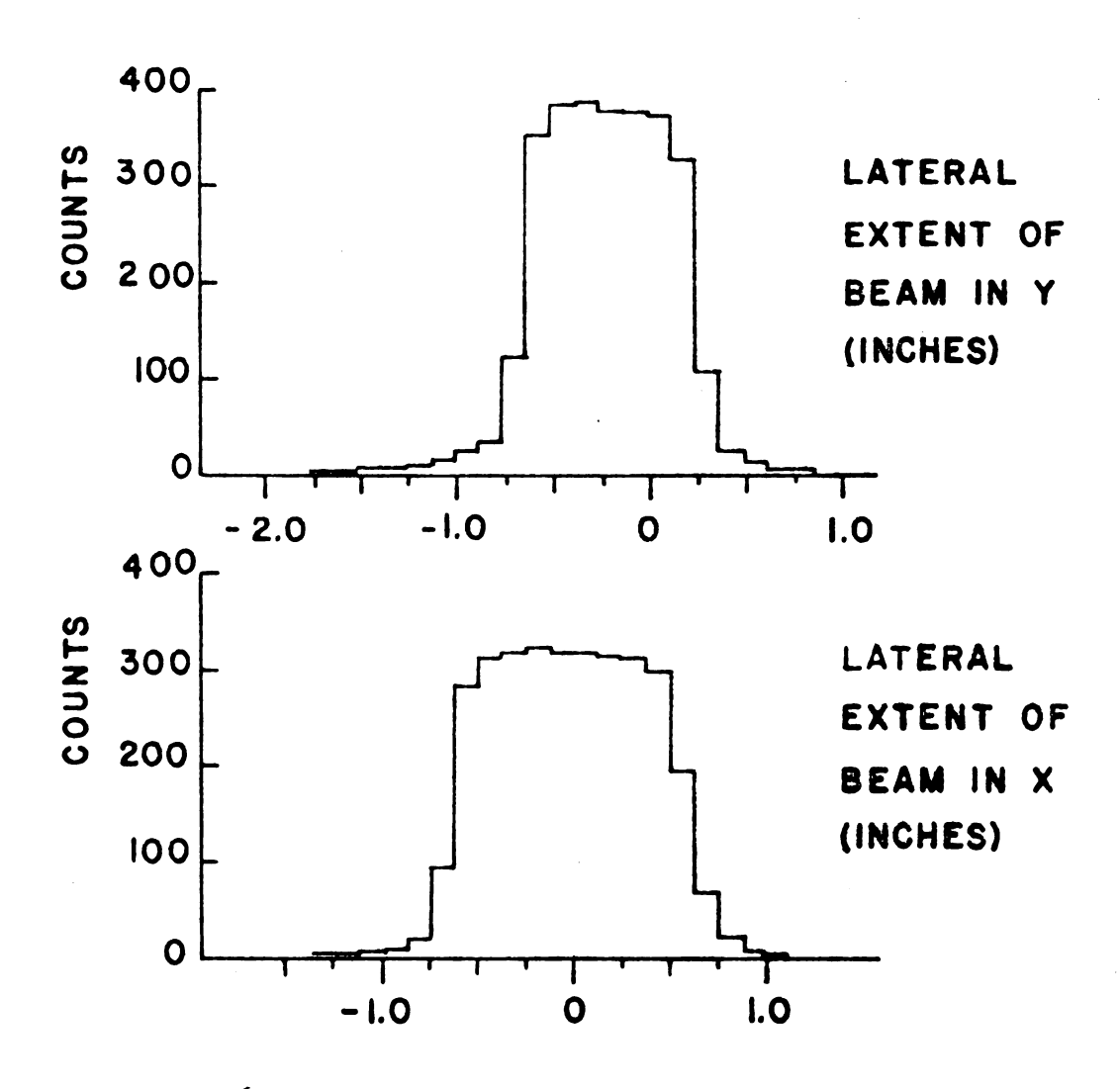


Figure 6. Beam Mapper Configuration and Beam Maps.

the midpoint of the counter distribution determined the physical displacement of the actual beam center from the surveyed 7° neutral line. The width of the distributions determined the lateral extent of the beam near the target. With this device we were able to collimate the beam onto the target with a spot 0.94 x 1.25 in² to within ± .03 in. accuracy (roughly one counter thickness).

3. Beam-Target Matching

The experimental target of dimensions $0.8 \times 1.0 \times 2.0$ in 3 was located 145 ft downstream from the internal beryllium target. Since it was situated within a cryostat, conventional survey techniques could not determine if it was correctly positioned in the beam.

An initial check of the target location was made using an x-ray source (see Figure 7). Tungsten crosshairs were surveyed into position on the beam line up and downstream of the target. An uncollimated, point x-ray source was placed in the beam line just upstream of the crosshairs and allowed to expose polaroid film downstream. After a few trials with the x-ray unit in different locations, the crosshairs were aligned on the film, implying that the source was positioned directly on beam line center. The glycol polarized target also appeared in the exposures, and its position relative to beam center could be determined by measurement on the film.

During actual experimental running, the target location was checked whenever a new one was installed in the

Figure 8. Target Location Reconstructed from Straight Through Tracks into the Upstream Chambers.

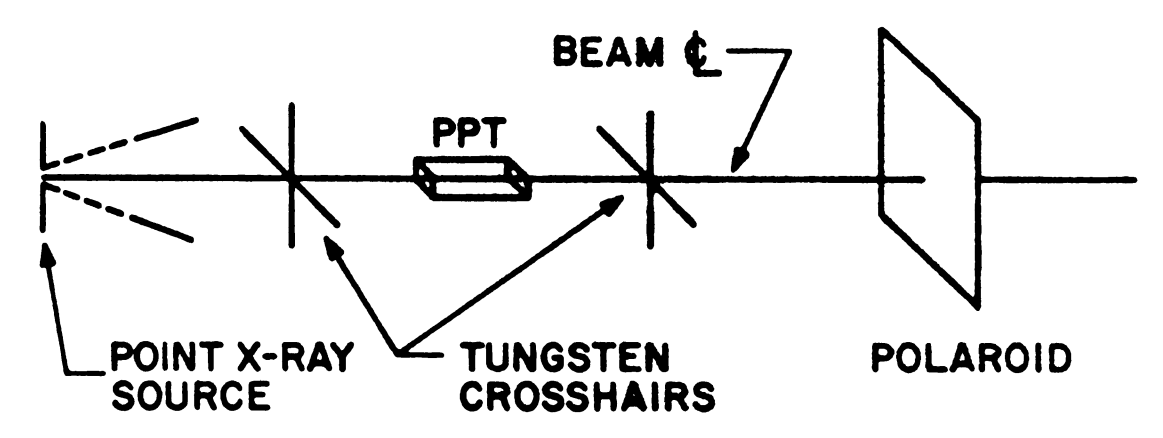


Figure 7. X-Ray Source Configuration

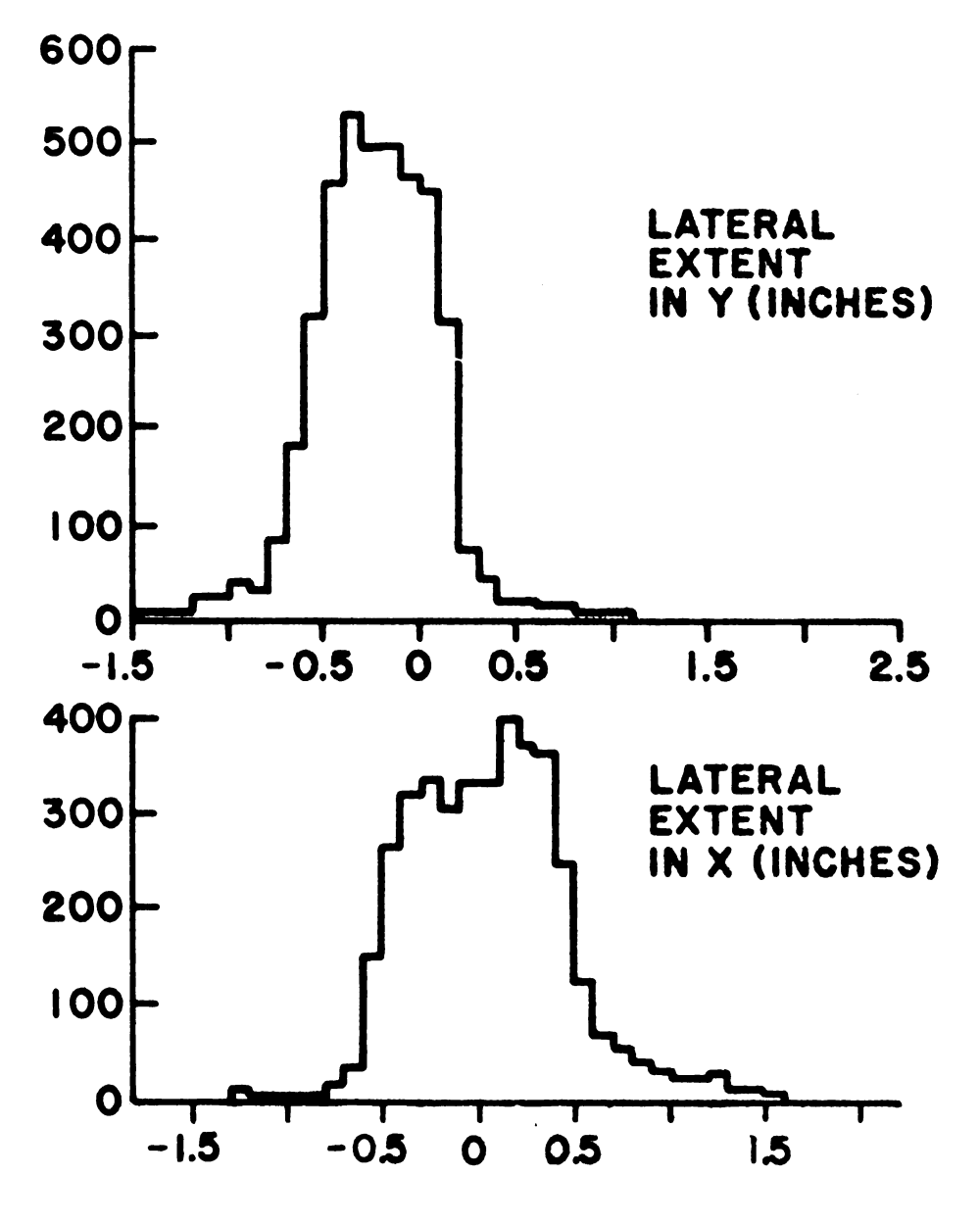


Figure 8

cryostat by turning off the polarized target and bending magnets and allowing the spark chambers to trigger on straight charged particle tracks. These tracks were then extrapolated back to the target position in a computer analysis and directly measured the effective target size and hence the extent to which the beam and target lateral areas were matched (Figure 8).

B. The Polarized Target

The polarized target used in the experiment was the Argonne Polarized Target Facility PPT-II⁹ consisting of potassium-dichromate doped ethylene glycol at liquid ⁴He temperature and 25 kG field.

The discussion naturally splits into two sections:

What is the mechanism for proton polarization, and what hardware does one need to achieve it. I will temporarily defer
equipment aspects and proceed with a qualitative discussion
of the "theory".

1. Mechanisms of Polarization

Targets typically consist of two main components, a source of free protons to be polarized and a doping agent which provides unpaired electron spins. When the sample is placed in a magnetic field the electron level is split in two with level separation $\hbar\omega_e$, ω_e being the electron Larmor frequency. In addition, for each particular electron level there are two sublevels corresponding to the two possible spin orientations of the proton.

Dynamic orientation of nuclei involves manipulation of electron spin states to achieve a desired proton spin configuration. The simplest illustration of this type of scheme is the "solid effect", shown in Figure 9. 10, 11 Suppose we have the electron and proton system in a strong magnetic field \vec{H} with Larmor frequencies \vec{e} and \vec{n} respectively. If the electron line is sufficiently narrow, one can distinguish the two sublevels $\overset{\leftarrow}{w}_{e}+\omega_{n}$, $\overset{\leftarrow}{w}_{e}-\omega_{n}$, and there are three classes of possible transitions:

(i) transitions with single electron flip, no proton flip (CA, DB).

These transitions occur rapidly as the electron spin is relaxed yielding a phonon of energy $\omega = \omega_{\rm CA} = \omega_{\rm DB} \ \, \text{to the target lattice.}$

(ii) transitions with single proton flip, no electron flip (DC, BA).

Nuclear relaxation occurs more slowly than electron relaxation (i).

(iii) transitions with simultaneous electron and proton flip (DA, CB).

In the absence of electron-nucleon dipolar couplings these are forbidden.

To produce a desired proton polarization through the "solid effect", one uses microwave rf to force one of the

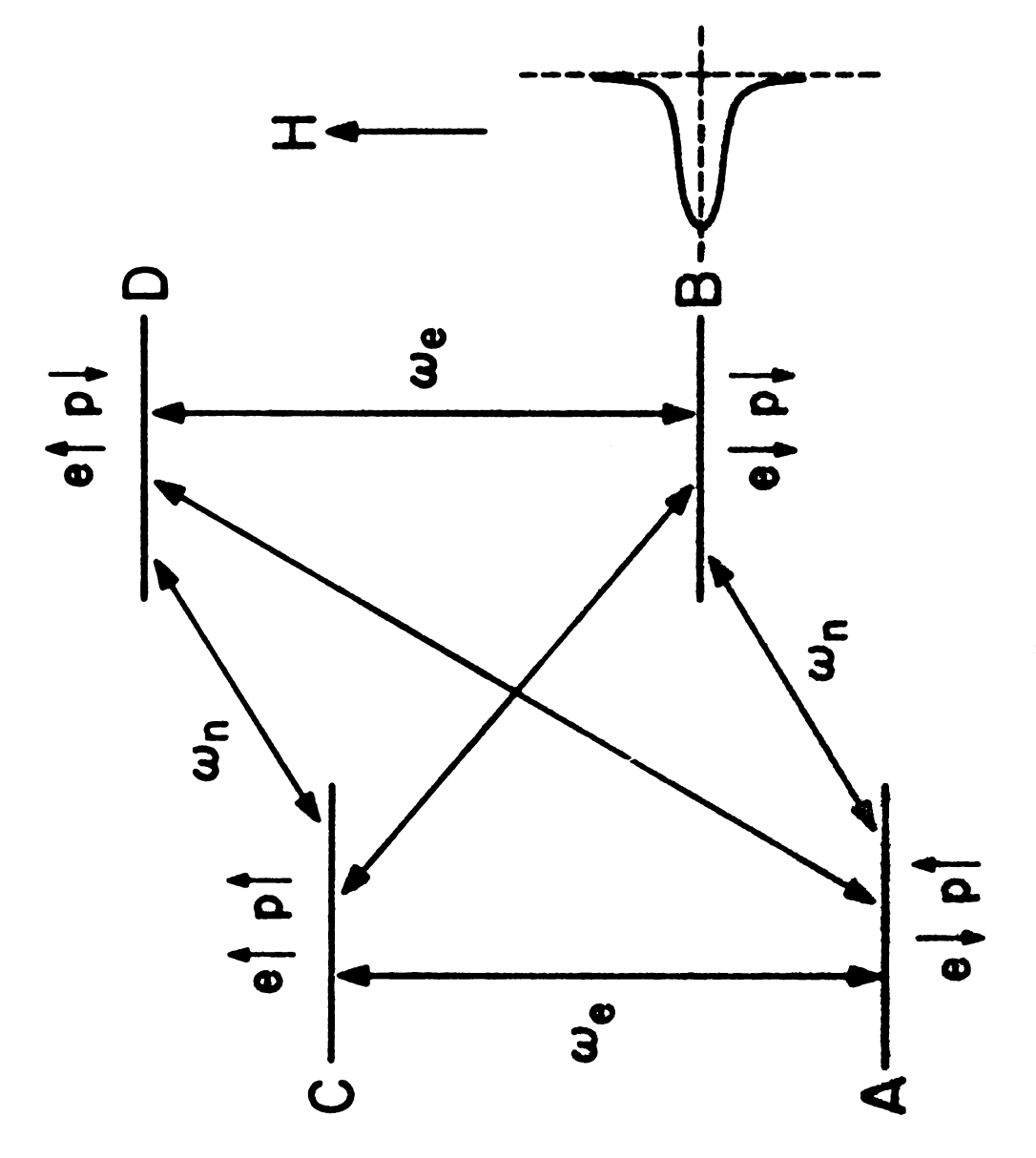


Figure 9. "Solid Effect" Energy Level Diagram

forbidden transitions AD or BC to occur. Since the type (i) transition is swift, the excited electron quickly relaxes to its ground state with the proton spin in the final orientation desired.

This simple explanation works fine for targets such as $LMN(La_2Mg_3(NO_3)_2 \cdot 24 H_2O)$ doped with neodymium because for that material the electron resonance line is sufficiently narrow that the proton sublevels are resolved. 11 Ethylene glycol presents a more difficult problem simply because the electron line width is ~150 gauss broad, leaving the two proton sublevels unresolved. An immediate consequence is that applying rf to the electron state can populate both nuclear spins since transitions BC and AD will both be induced. there are additional complications from the presence of other electrons nearby. First the Larmor frequencies for the electrons in the target are all assumed to be ω_{a} . This is justified to the extent that our magnetic field is uniform over the target volume (±3 Gauss) and potassium dichromate doped ethylene glycol has isotropic properties (a fairly reasonable assumption considering that $g_{eff}^{CrV} = 1.99$ and $S_{eff} = 1/2$ for this material, very close to free electron values). 12 Should there be an anisotropy of either external magnetic field or target composition, additional mechanisms for dynamic nuclear polarization are possible. 11 Second, the electron spin we are dealing with is not an isolated entity, but can be expected to have spin-spin interactions with neighboring unpaired lattice electrons. If one collects these "neighbors" into a spin-spin interaction reservoir and defines a Boltzmann temperature for the system, it can be shown that electron spin-spin interactions and rf-induced spin-spin interactions can lower the collective temperature. If one describes the protons collectively as a nuclear Zeeman reservoir, then the previously forbidden transitions AD, CB provide the thermal contact between the Zeeman and spin-spin systems and tend to equalize their temperature.

Hence by inducing forbidden transitions with rf, one not only produces proton polarization through a poorly resolved "solid effect", but also by the cooling of the nuclear Zeeman temperature through thermal contact with a low temperature electron spin-spin reservoir. For a specific setting of the external magnetic field, a particular microwave frequency will maximize the proton spin up population, another the spin down population.

Having qualitatively described some possible mechanisms for dynamic nuclear orientation, it remains to show how the polarization was experimentally created, maintained, and measured.

The polarized target facility consisted of five major components: the target, cryostat and cryogenic support systems, magnet, microwave rf system, and NMR detection system. All of the details of the systems are contained in various Argonne reports 9 so only salient features will be considered.

2. Polarized Target System

a. The Glycol Target

The target material was ethylene glycol (CH₂OH)₂ doped with 10% by weight of potassium dichromate K₂Cr₂O₇. The glycol acts as the source of free protons, the potassium dichromate as the source of unpaired electrons through the presence of the Cr^V radical. This particular target is liquid at room temperature and hence requires a containing material prior to cool down in the cryostat. The choice was air-mattress-like tubular bags of FEP (fluorinated-ethylene polymer) which were easily folded into the target shape required, yet permitted a large amount of surface area to be exposed to the liquid ⁴He bath, essential to uniform cooling.

The target shape was parallelepiped, 5 cm long by 2 cm high by 2.5 cm wide, a shape dictated by the desired thickness of the target in the beam direction (5 cm.) and the available space for the target material within the existing PPT-II cryostat which was of the horizontal continuous flow type (see Figure 10). These requirements were resolved by placing the cryostat at a 50° angle with respect to the beam center-line.

The target weight was 31 grams of which 3 grams were the FEP container bags. Since the bags were folded to form the target, a considerable amount of the target volume contained no glycol at all. After accounting for the packing fraction of the target, the effective density of the glycol was 0.85 gm/cm³. Once the slight overmatch of the beam area

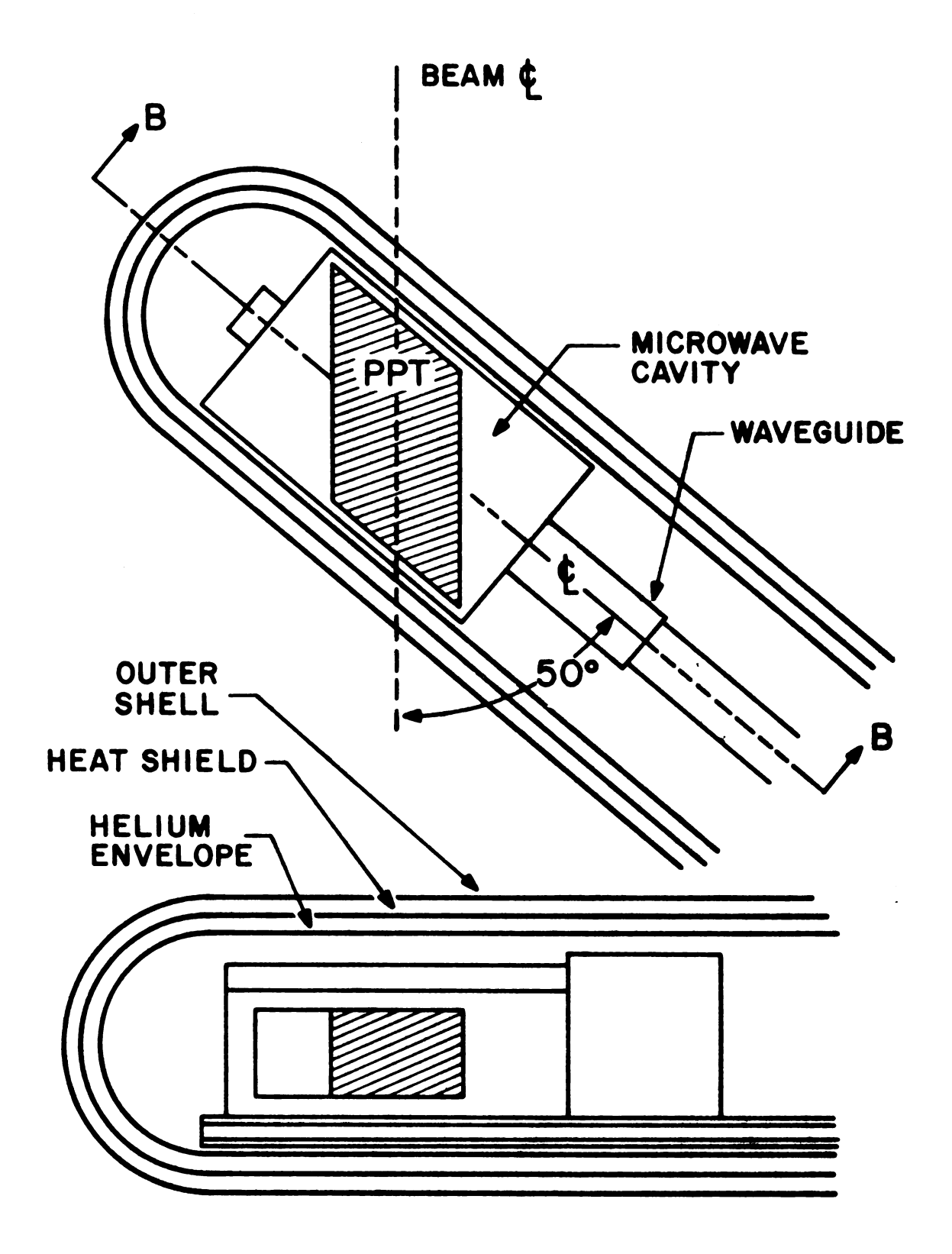


Figure 10. Polarized Target Cryostat

to the target area was included, the effective number of target protons was $2.04 \times 10^{23}/\text{cm}^2$.

b. The Cryostat

The cryostat within which the target and its 5 mil thick Be-Cu microwave cavity were placed was composed of several coaxial shells (Figure 10): The innermost shell was the liquid helium jacket of 12 mils stainless steel; the intermediate liquid nitrogen insulating jacket was of 5 mils Cu; the outer shell was a 16 mil aluminum vacuum jacket. In all the beam had to pass through .23g/cm² of cryostat structure in order to reach the target, which removed about 0.6% of the incident neutrons.

Liquid ⁴He was continuously transferred from a 50 liter storage dewar to the cavity. The role of the helium and separator vacuum systems ¹³⁻¹⁴ (Figure 11) was to maintain adequate cavity liquid level and vapor pressure. At typical pumping rates (27 gas ⁴He lpm), the cavity pressure measured by Mcleod gauge ranged between 150-350 microns corresponding to a target temperature of 1.0-1.15 ⁰K (see Figure 12).

Although liquid ⁴He temperatures are not the last word in polarized target technology, enough thermal effects were suppressed to allow roughly 40% of the target protons to be polarized.

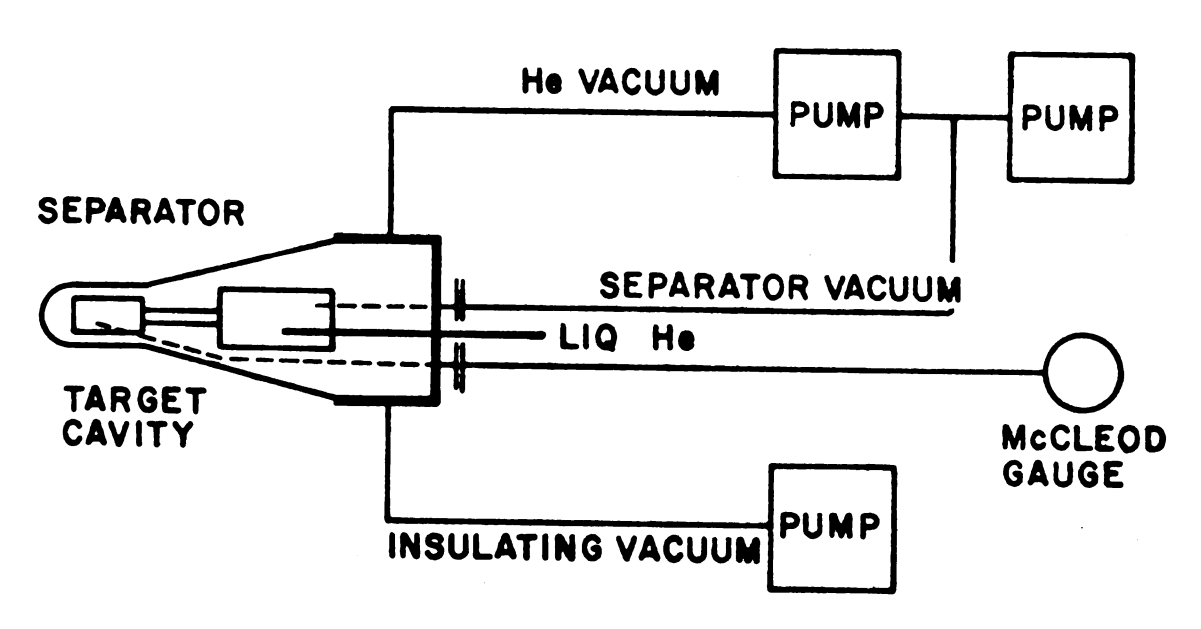


Figure 11. Cryogenic Systems

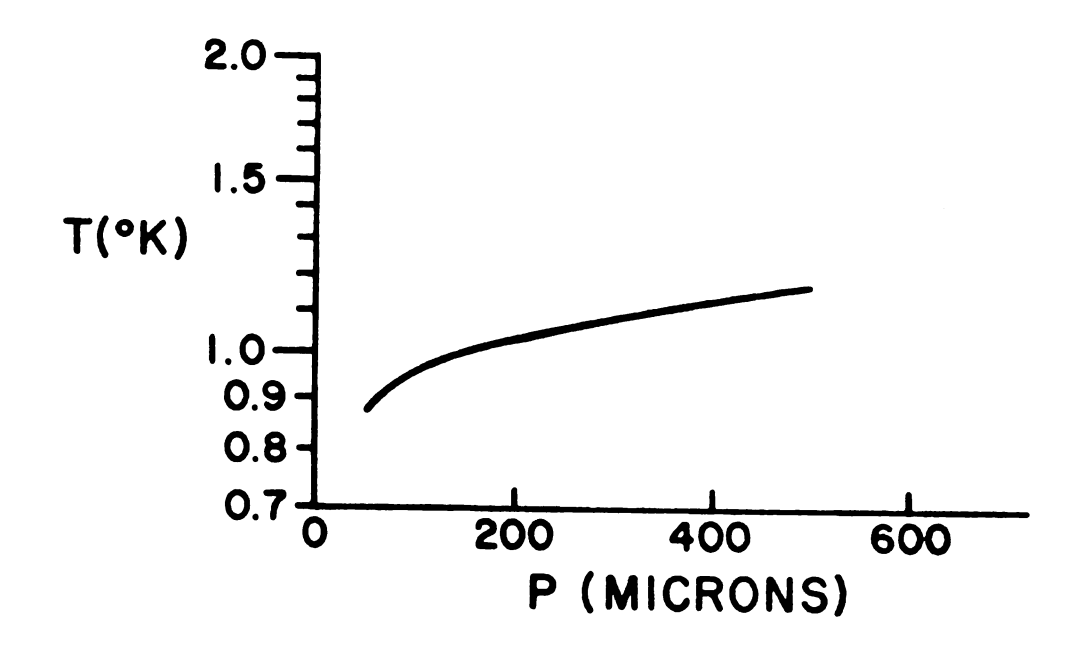


Figure 12. Target Temperature Vs. Cavity Vapor Pressure.

c. Magnet

The glycol target sat in the center of a 3 in. gap between the pole tips of a Varian magnet. The field was maintained at 25 kG with a measured inhomogeneity of ± 3 Gauss over the target volume. The field was measured and stabilized to ±.1 Gauss by means of a Hall probe feedback system and a map of the radial field is presented in Appendix I.

d. Microwave System

The source of microwaves for spin pumping was a French built COE4¢B carcinotron, a back-wave oscillator. In this device microwaves are generated by passing a beam of electrons through a copper interaction structure. By suitably tuning the electron beam one can adjust the power and frequency delivered to the wave guide, typically 1.5 Watts at -70.6 GHz during running conditions. The microwaves of appropriate frequency then passed through a standard plumbing arrangement to the target cavity (Figure 13). A phase sensitive feedback amplifier in combination with wavemeters in the waveguide system then maintained the carcinotron at a stable line voltage, which insured a stable output frequency. 16

e. NMR Detection

The actual value of the polarization was measured by nuclear magnetic resonance. The NMR system was a standard RLC circuit in which the target, wrapped with five turns of

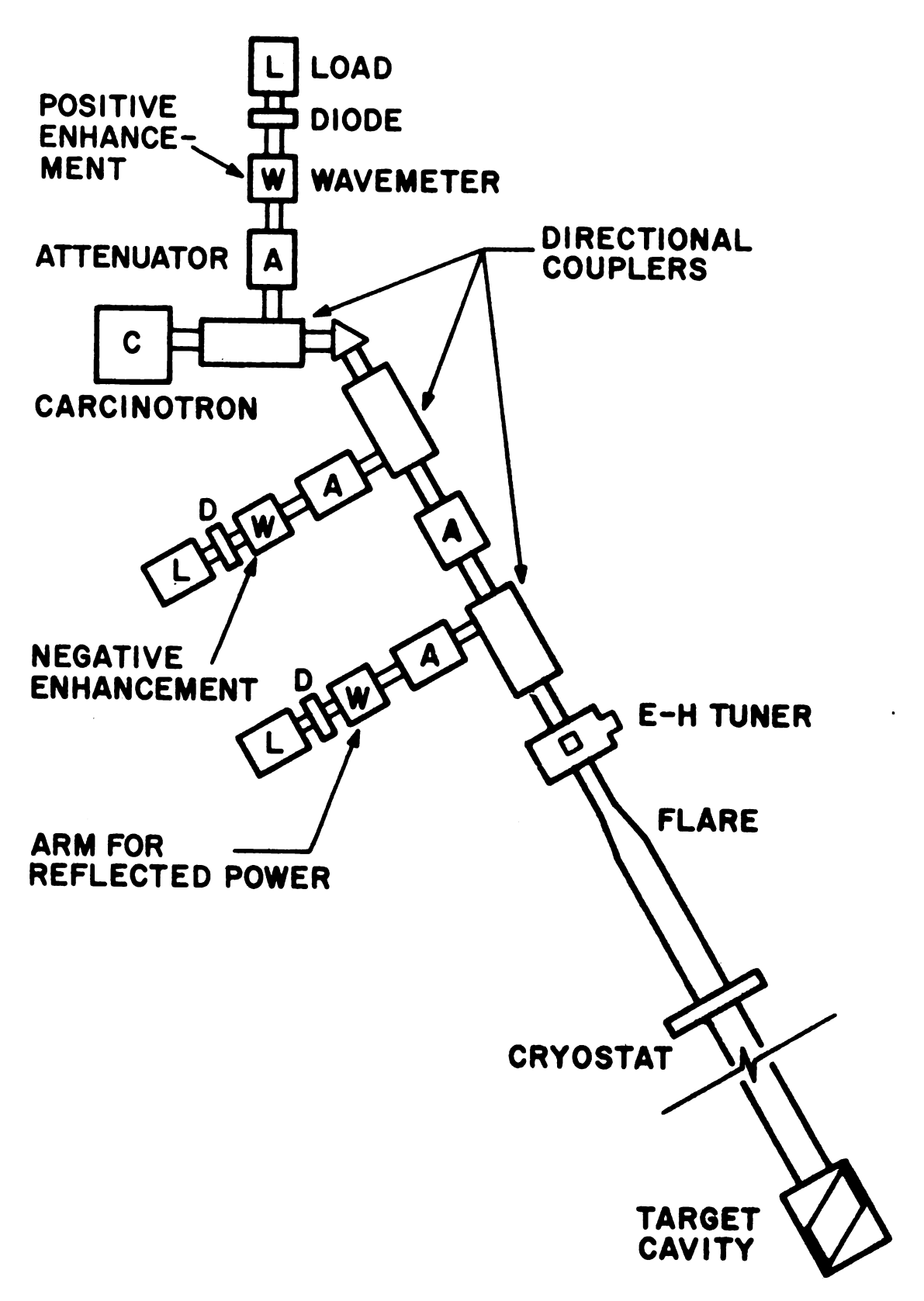


Figure 13. Microwave Plumbing Arrangement

wire, was a component with equivalent circuit shown in Figure 14. The large external resistance $R_{\rm E}$ (7.5 k Ω) essentially determined the current -- hence the NMR system was a constant current Q-meter. ¹⁷

Proton spins in the target absorb energy from the circuit as the frequency of the signal generator passes through the proton resonant frequency, ω_n . This energy absorption is described electrically as a complex susceptibility, and the target-coil system is assigned a complex inductance:

$$L = L_0(1 + 4 \pi n x) = L_0(1 + 4 \pi n (x' - ix''))$$

where η is the filling factor, the amount of volume within the coil that the target occupies, and χ ' and χ " are the real and imaginary parts of the susceptibility χ . The frequency average of χ " is proportional to the amount of power absorbed from the circuit, and hence to the degree of spin alignment of the protons:

$$T = \xi \int_{0}^{\infty} \chi''(\omega) d\omega \qquad (1)$$

where P is the magnitude of the target polarization, $T = |\overrightarrow{T}|$ and ξ is a proportionality constant. In Appendix B it is shown that $\chi''(\omega)$ may be approximated as:

$$\chi''(\omega) = -\frac{1}{4\pi Q} \frac{V(\omega) - V_{\odot}}{V(\omega)}$$
 (2)

where Q = $\omega_n L_0/R$, V(ω) is the voltage measured by the NMR detector for signal generator frequency ω (see Figure 14 for the schematic), and V_O is the base line voltage of the NMR detector when the frequency ω is far from resonance value ω_n . The constant ξ is determined from an NMR measurement of the

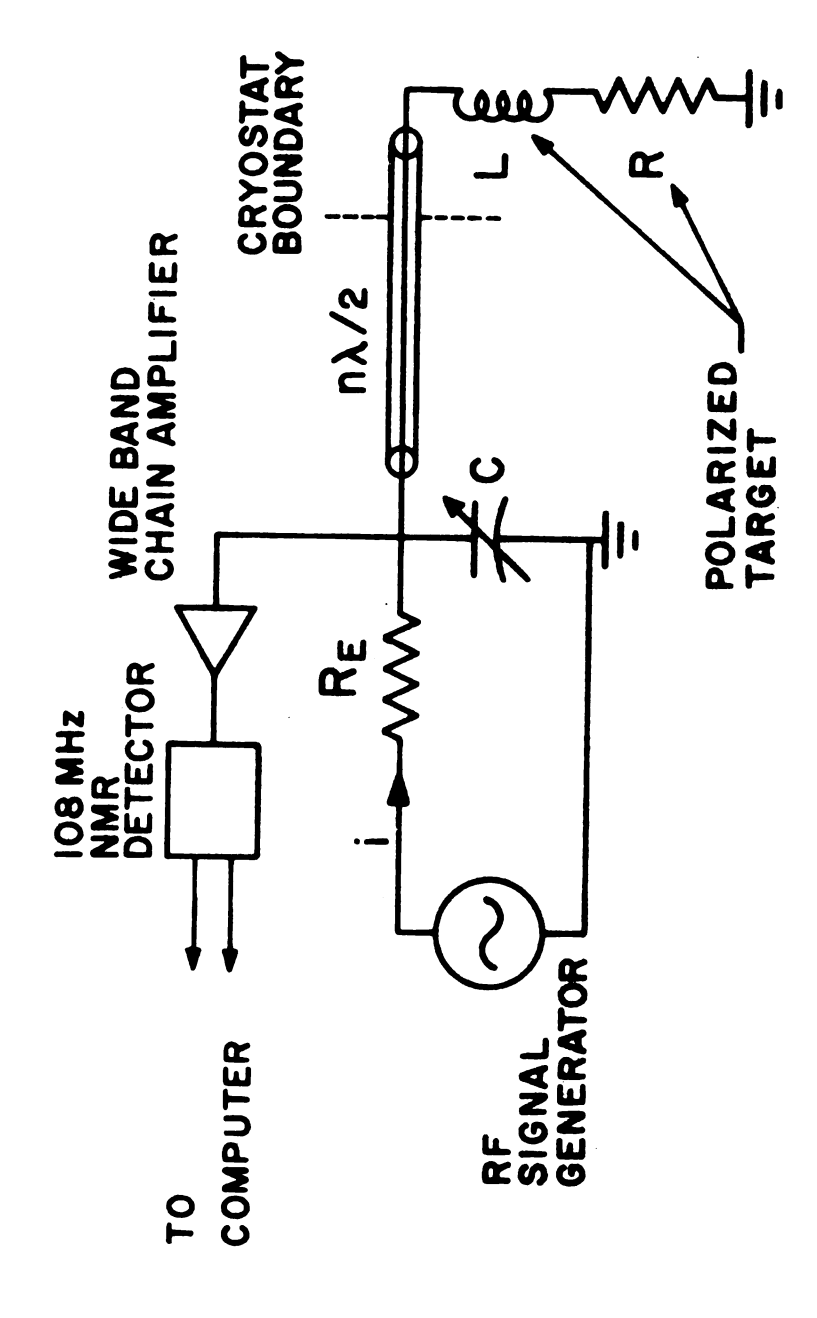


Figure 14. NMR Detector Circuit Diagram.

target polarization at thermal equilibrium (microwaves off), given by the Boltzmann distribution. 18

$$P_{TE} = \frac{-\xi}{4 \pi Q} \int_{0}^{\infty} \frac{V_{TE}(\omega) - \tilde{V}_{O}}{V_{TE}(\omega)} d\omega = t \sinh (+g \beta II/2kT)$$
 (3)

where g is the g factor for the proton, $\beta = e\hbar/2mc$ is the nuclear magneton, k is the Boltzmann factor, and T is the target temperature in ${}^{O}K$.

The expression for the enhanced polarization (1) is then given by:

$$T = P_{TE} \frac{\int_{0}^{\infty} \frac{V(\omega) - V_{O}}{V(\omega)} d\omega}{\int_{0}^{\infty} \frac{V_{TE}(\omega') - \tilde{V}_{O}}{V_{TE}(\omega')} d\omega'}$$

The proton resonance was swept every five minutes by the NMR system, and signals for both the voltage $V(\omega)$ and its derivative with respect to frequency $dV(\omega)/d\omega$ were sent to the electronics trailer. The $dV(\omega)/d\omega$ signals were generated by a set of "tickler" coils on the pole tips of the magnet, and were used extensively in the measurement of the target polarization because of their sensitivity in the proton resonance region $\omega \approx \omega_n$. For example, rather than rely on a direct measurement of $V_{TE}(\omega')$ whose size is very small, one uses instead

$$V_{TE}(\omega') = \int_{0}^{\omega'} \frac{dV_{TE}(\omega'')}{d\omega''} d\omega''.$$

The $V(\omega)$ and $dV(\omega)/d\omega$ signals were recorded in two ways: first, on paper tape for use in an off-line analysis

developed by the Argonne staff, and second, by fast logic interfaced to the on-line DDP-24 computer which optically displayed the polarization and wrote the NMR values onto magnetic tape as a part of the experimental data vector. The actual calculation of the target polarization was performed by calculating the various integrals as Riemann sums. In the fast logic scheme, two points on an NMR sweep were recorded during the first event trigger of a given ZGS beam spill, and four numbers per point were read into blind scalers: The NMR frequency ω , the V(ω) signal, the dV/d ω signal, and a 1 MHz clock. The latter number was used to normalize the other three, to insure equal $\Delta\omega$ spacing in the Riemann sums. How this system was tied into the existing NMR system is shown in Figure 15.

Several paper tape recordings were made during each data run (~3 hrs. in length) as a check of the interfaced online scheme which monitored the polarization continuously. The two methods agreed to within $\Delta T = 2\%$. Once every twenty-four hours, ten target thermal equilibrium sweeps were recorded to calibrate the NMR system and determine ξ . For these measurements the microwaves were turned off, and the data taking was suspended temporarily. The polarization direction of the target was reversed every successive data run to eliminate any experimental bias; within each run, the polarization fluctuated by $\pm 4\%$.

On the basis of the NMR measurement, the average target polarization was determined to be 39% for positive enhancement

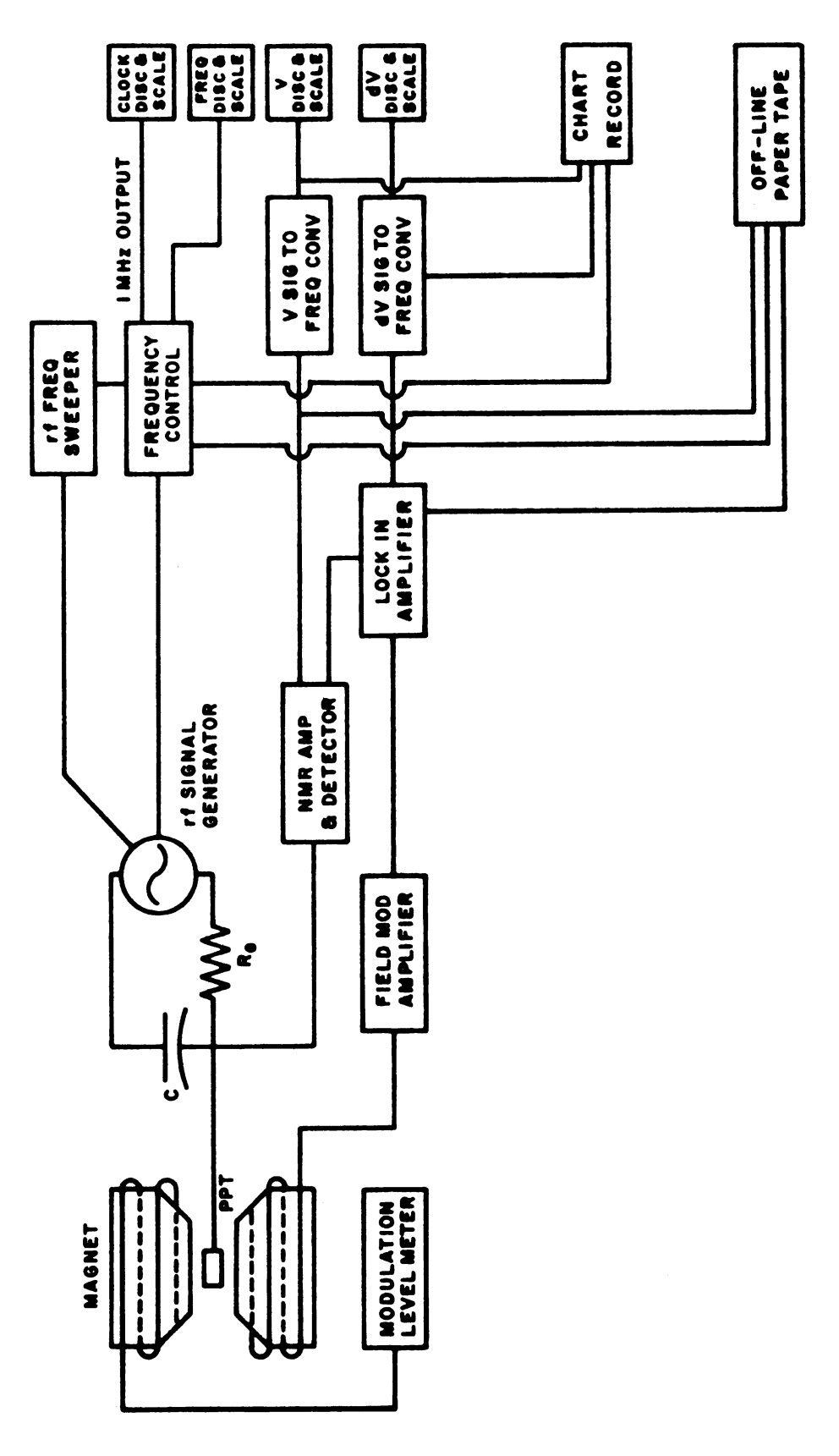


Figure 15. NMR System Schematic

and 40% for negative enhancement.²⁰ Relative to an absolute calibration of the target polarization by a double scattering experiment, the NMR measurement was accurate to 7% of the target polarization value: $\langle P \rangle \approx 40 \pm 3\%$.²¹⁻²³

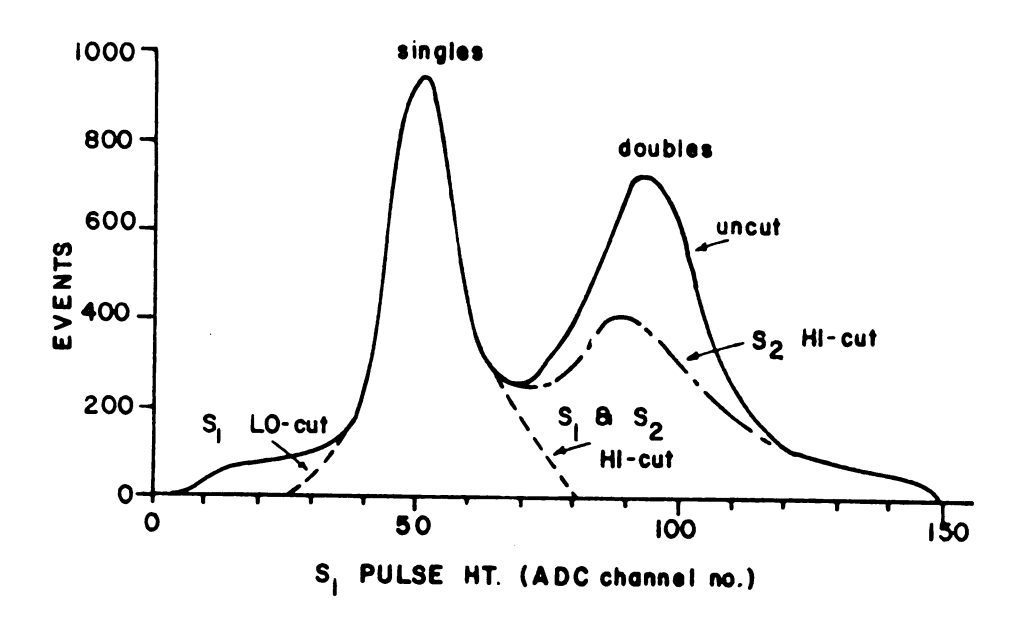
C. The Two-Arm Spectrometer

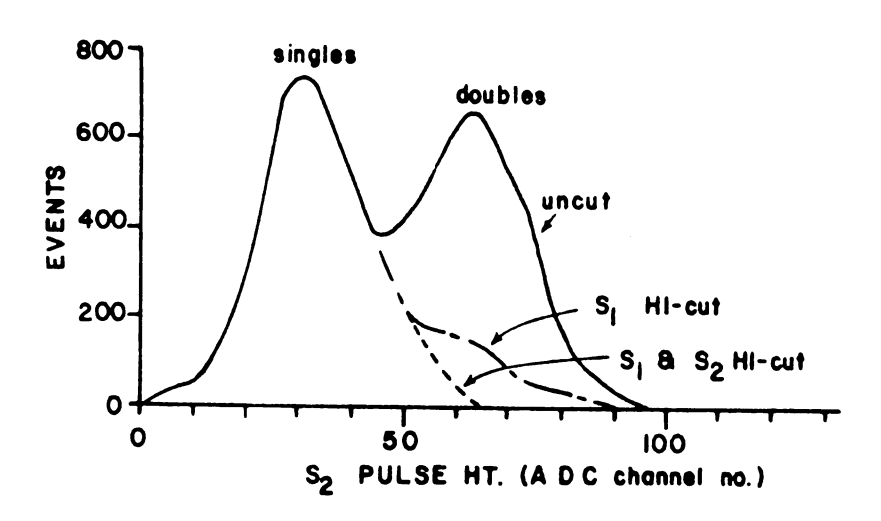
The detection of the final state neutron and proton was performed with a two-arm spectrometer.

1. The Proton Arm:

The proton was detected by a coincidence between four counters, S1, S2, S3, S4 and had its momentum and direction specified by a wire chamber magnetic spectrometer. The corridor for protons into the upstream chambers was defined by counters S1(1/8" x 3" x 5") and S2(1/8" x 5" x 7") located 21 in. and 41 in. from the target respectively. Single protons were selected by pulse height cuts on these two dE/dx counters which rejected multiply ionizing events; approximately five percent of the S1 and two percent of the S2 singly ionizing distributions were cut out by this method (see Figure 16).

To minimize triggers on final states of higher multiplicity, anti-counters were extensively employed. In the vicinity of the target, wide angle charged particles were vetoed by a group of four 0.125 in. thick scintillation counters which formed a tight fitting box around the cryostat except for a small downstream opening to allow protons into the forward spectrometer. The rejection of events in the upstream





S-COUNTER PULSE HT. SPECTRA

Figure 10. Pulse Height Distributions for S1 and S2 Counters.

chambers containing γ -rays and divergent charged particles was effected with two γ -sensitive hole counters $\Gamma 1$, $\Gamma 2$ consisting of 0.5 in. lead converter and 0.375 in. scintillator with apertures which allowed particles within the proton corridor to pass unhindered. A large γ -sensitive counter $\Gamma 3$ vetoed strays on the side of the beam line opposite to the proton spectrometer.

A schematic of the proton arm logic is shown in Figure 17. The quantity $\overline{T}S$ was the proton trigger, whereas the ratio $\overline{T}:S/S$ (where $\overline{T}:S$ is \overline{T} delayed 120 nsec relative to S) was a measure of random blocking by all veto counters (except those near the neutron counters); from such blocking, approximately 10% of the possible triggers were lost.

The spark chambers were arranged in four modules containing three x and y (horizontal and vertical) planes each. Spark and fiducial information were read out magnetostrictively, preamplified at the wands, and sent to the computer trailer. Each chamber was viewed by a number of scalers, allowing the digitization of four sparks per plane in the chamber modules upstream of the magnet, two per plane in the modules downstream (spark chamber specifications are presented in Appendix C). Fringe fields near the two magnets necessitated the shielding of some of the magnetostrictive wands in the upstream chamber modules to prevent signal attenuation or inversion.

Once a complete track was indicated by the chambers, the proton momentum was calculated using a 14-term polynomial

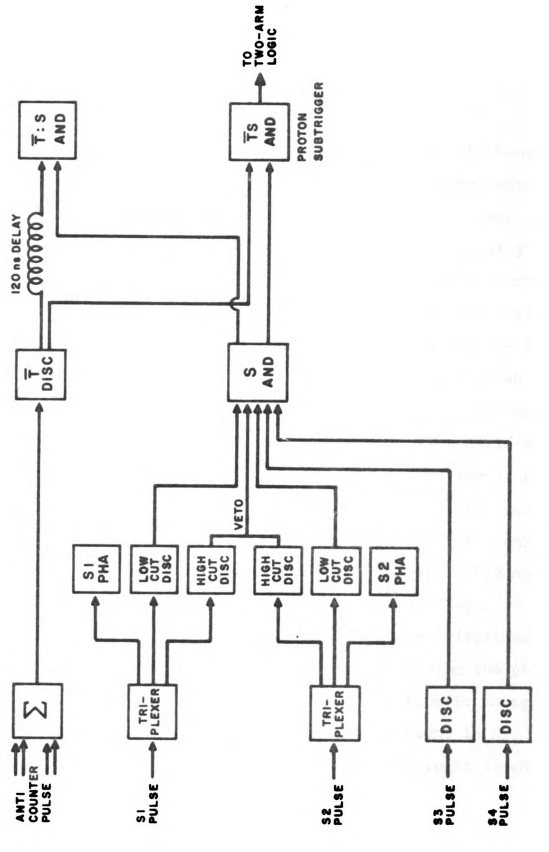


Figure 17. Proton Arm Logic

(see Appendix E) which returned momentum values accurate to better than 1.5% full width at half maximum. Resolution for the proton arm is shown in Appendix C.

2. The Neutron Arm:

The slow recoil neutron was detected by two banks of thick scintillation counters, each covering a different range of momentum transfers but with enough overlap to check consistency. In close to the target were the horizontally stacked short counter arrays (each 6 x 6 x 20 in³) which were sensitive to neutrons with $0 \le |t| \le 0.2$. The more distant long counters were arranged vertically and covered the range $0.03 \le |t| \le 1.0$ (neutron counter acceptances are shown in Appendix D). Since the neutron counters were run at thresholds low enough to detect neutrons with 2 MeV kinetic energy (theorem 2.006 (GeV/c²)), they were vulnerable to low energy room background. To alleviate this problem a wall of anti-counters was placed between each array and the target to veto any charged particles from beam line spray; elsewhere the neutron counters were shielded by a house of concrete block.

Laboratory angles for the neutron were determined by which counter fired and end-to-end timing between the photo-tubes on each end of that counter; neutron kinetic energy was determined by time-of-flight relative to a count in Sl. A simplified schematic of the neutron arm fast logic is shown in Figure 18, and resolution for the neutron arm is shown in Appendix D.

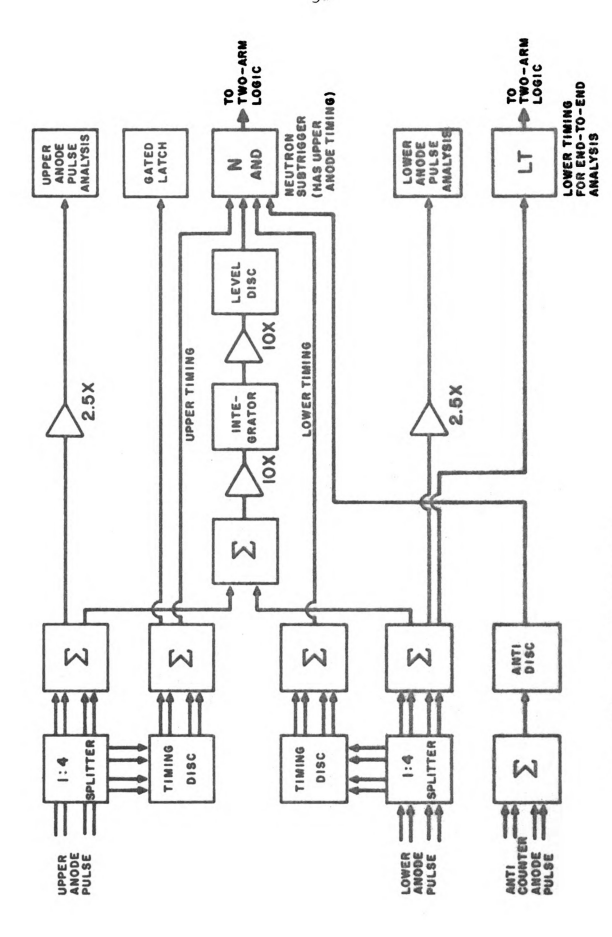


Figure 18. Neutron Arm Logic

3. The Complete Trigger:

With a coincidence between neutron and proton arms in the two-arm logic (Figure 19), the complete trigger was satisfied, firing the spark chambers. Digitized chamber information, neutron counter pulse heights and timing information, and NMR information were then read into an on-line DDP-24 computer which recorded the data on magnetic tape and which, between beam spills, analyzed a portion of the data and displayed monitors of equipment and event constraints.

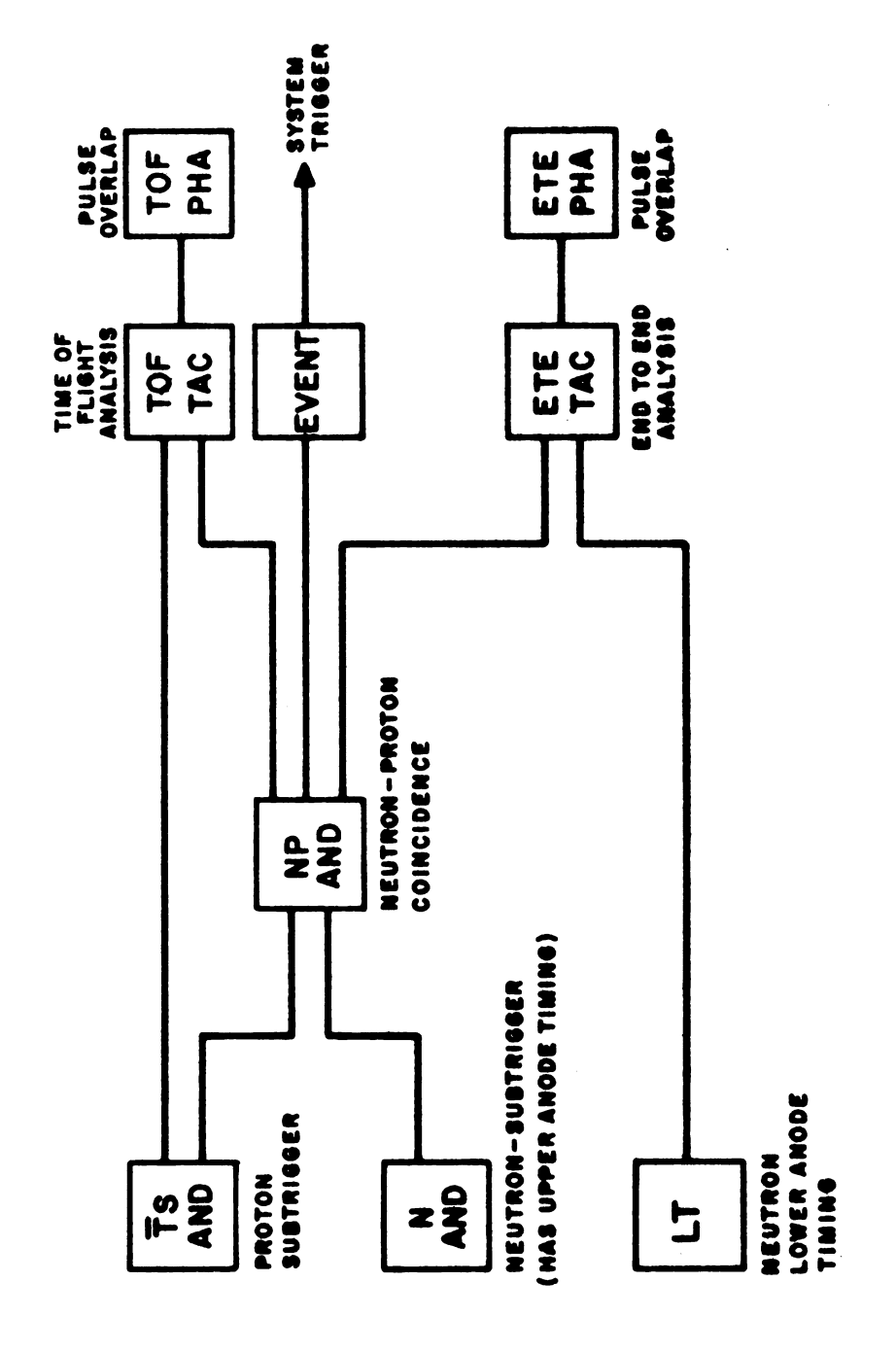


Figure 19. Two Arm Logic

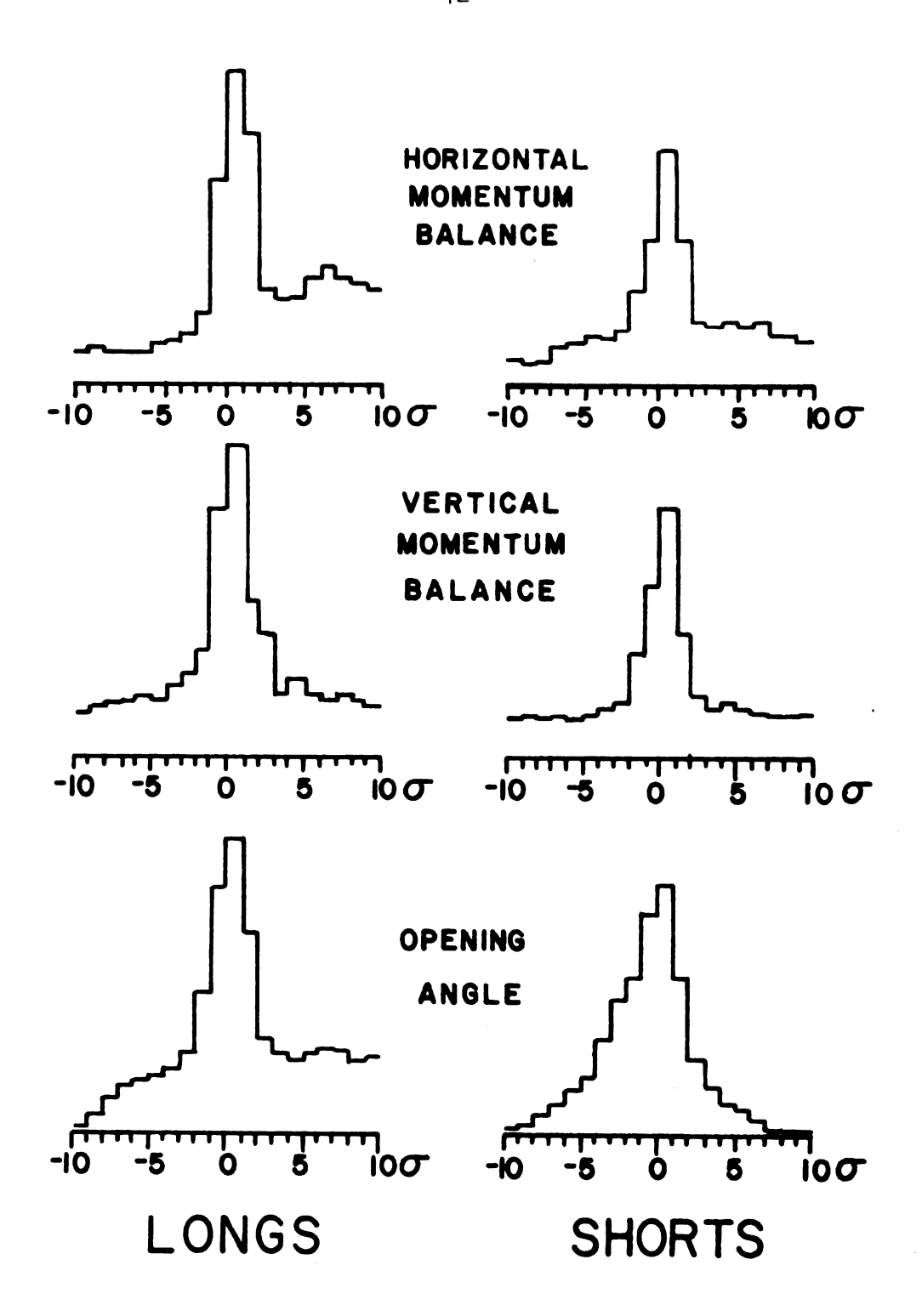
CHAPTER III

DATA COLLECTION AND ANALYSIS

During the three months of data taking 11.1×10^6 acceptable triggers were obtained with the polarized target and 2.2×10^6 triggers with the glycol target replaced by a graphite dummy target which contained no free protons. Two separate analyses were performed: One was a partial analysis of the data using the on-line computer, the other involved a full off-line kinematic fit for all the data on the Michigan State University CDC 6500 system.

A. The On-line Analysis

In the on-line analysis, the four second interval between beam spills allowed the DDP-24 computer to analyze 50% of the events. No time consuming kinematic fit was performed here; instead the three carefully selected constraints of x and y-momentum balance and opening angle between the outgoing particles (see Appendix A for definitions of variables) allowed a clean separation of elastic events from background (Figure 20). The y-momentum balance was particularly sensitive, and the background subtraction was made by extrapolating the wings of the constraint distribution under the peak.



ONLINE CONSTRAINTS

Figure 20a. On-line Constraints for Px, Py, and Opening Angle.

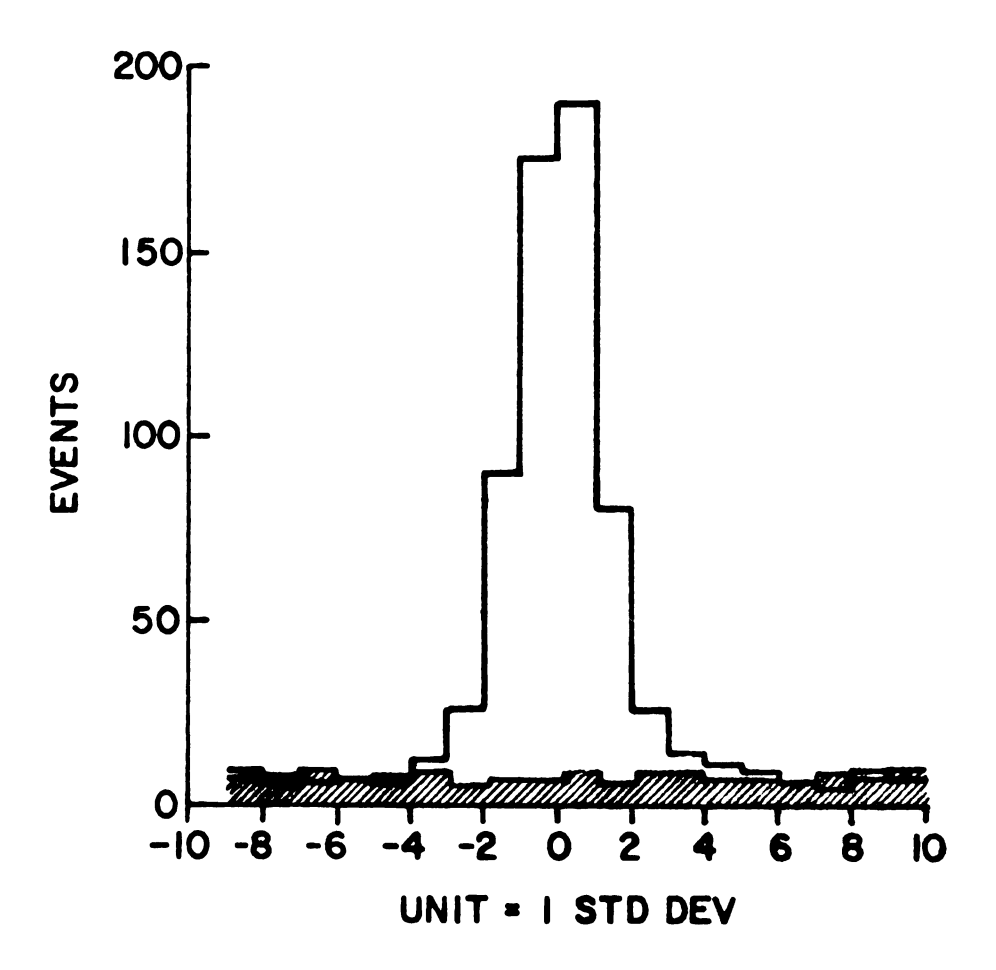


Figure 20b. On-line Constraint for Py Balance with Graphite Dummy Target Data Shaded.

This treatment was useful as a preliminary investigation of the data, but the complexity of the glycol target $(CH_2OH)_2$ required a careful study of background to check the possible effects of quasi-elastic events, for example events from bound protons. This was left to the off-line analysis.

B. The Off-line Analysis

The purpose of the off-line analysis was two-fold:

First, the data were subjected to a kinematic fit, and second,
a careful study and subtraction of background was performed.

A full kinematic fit with 3 degrees of freedom (variable choices shown in Appendix A) was applied to both the glycol and graphite dummy target data. χ^2 -distributions were obtained for each sample, |t|-bin, and neutron counter type (several are shown in Figure 21). If the data sample was purely elastic, the distribution of events would have the following statistical form:

$$dN/d\chi^2 = C\chi \exp(-\chi^2/2),^{24}$$

where C is an event normalization and dN/dx^2 is the x^2 density of events. Experimentally, the distributions were characterized by the following forms:

$$dN/dx^2(glycol) = Ax \exp(-bx^2) + xB(x^2)$$

 $dN/dx^2(graphite) = x\tilde{B}(x^2)$,

where A is an event normalization, b is the slope of the elastic peak (typically 0.4 \leq b \leq 0.5 experimentally and 0.5 ideally²⁴), and B(χ^2), $\tilde{B}(\chi^2)$ are background distributions, a

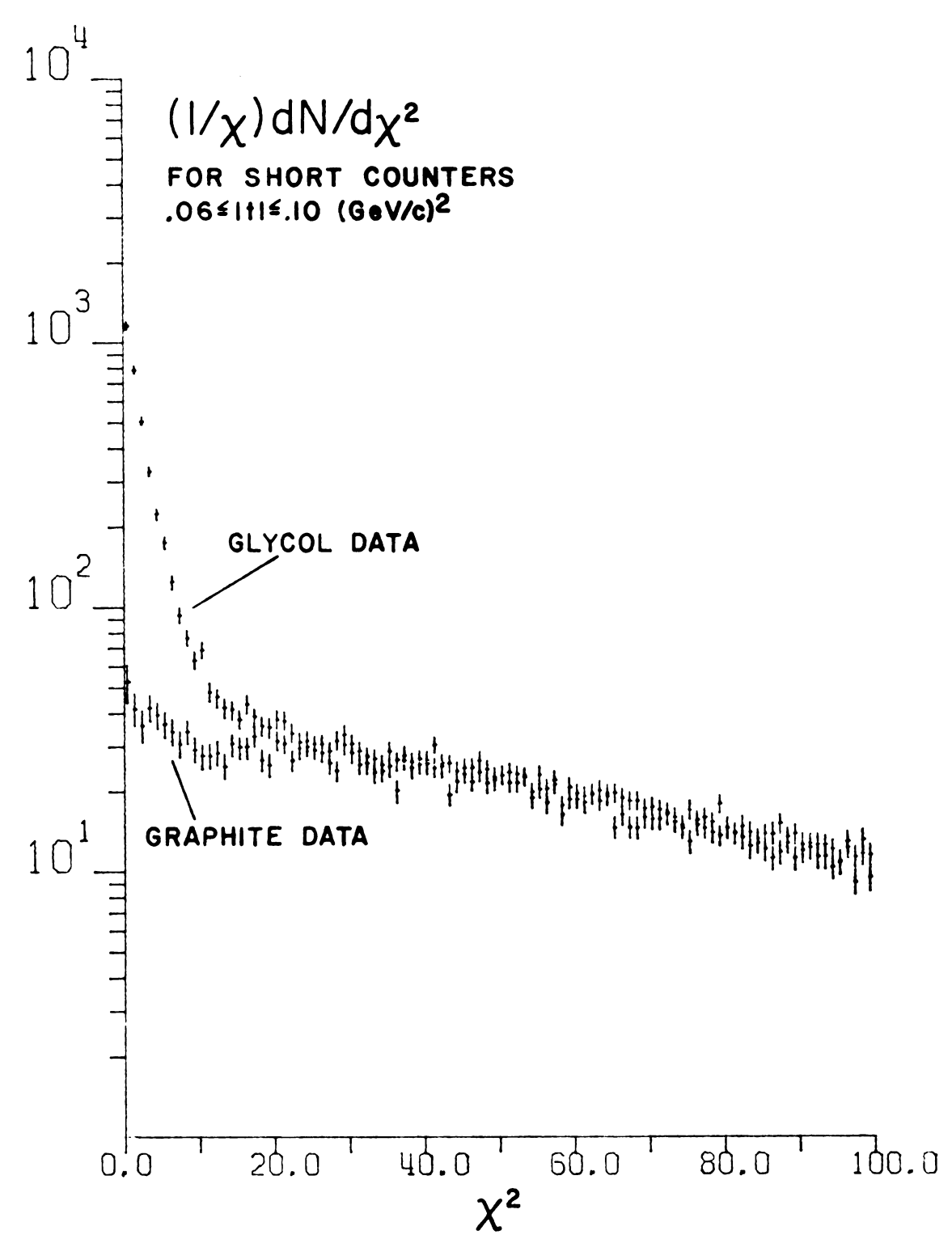


Figure 21a. Fitted Event x^2 Distributions for Both Glycol and Graphite Samples for Short Counters.

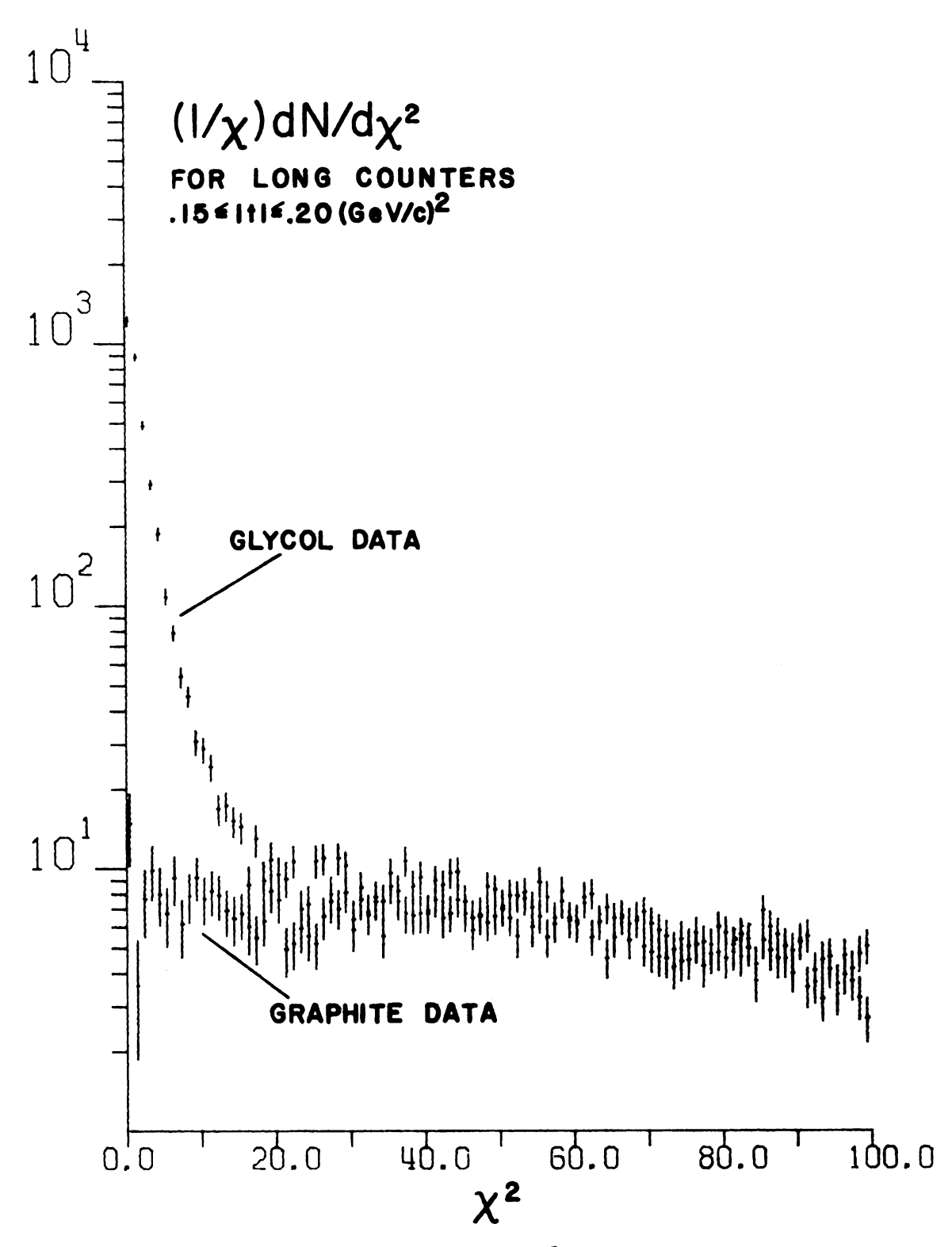


Figure 21b. Fitted Event x² Distributions for Both Glycol and Graphite Samples for Long Counters.

major portion of which are neutron collisions with bound protons in the target. With our experimental resolution, the Fermi momentum of such protons distributes the resulting np events over all x^2 , $0 \le x^2 \le 100$ (see Appendix F for a discussion of these effects).

A comparison of the normalized dN/dx^2 distributions for the glycol and graphite samples reveals that, to well within statistics $\tilde{B}(x^2) = B(x^2)$ for $15 \le x^2 \le 100$. This consistency suggests that the normalized graphite data correctly represents the background at all x^2 . Hence the following method was used to remove the background: For all events with $x^2 \le 10$, an event-by-event subtraction of the graphite data from the glycol data was performed, yielding a final elastic sample of 300,000 events from which the polarization parameter was determined.

Typical percentage backgrounds for various |t | values and counter type are presented in Table 1.

C. The Polarization Calculation

In this section the polarization parameter and unpolarized event rate are calculated using experimentally measured quantities.

For a given run (i) with target spin up along the y-axis and a given data bin (ΔP_{LAB} , Δt), the number of events observed at an angle λ above (or below) the horizontal (x, z) plane is:

$$N_{i}^{+} = O_{i}^{+}N_{o}(1 + T_{i}^{+}P_{o}\cos \lambda) + \beta_{i}^{+}$$
 (1)

Table 1. Table of Percentage Backgrounds in the Neutron Counters as a Function of $\left|t\right|$

.0103		
_	33	-
.0306	14	5
.0610	11	4
.1015	13	2
.1520	25	2
.2025	-	5
.2535	-	6
.3545	-	7
.4560	-	17
.6075	-	36
.75-1.0	-	58

where 0_1^+ , β_1^+ , and T_1^+ are the number of OMON counts, background counts, and target polarization magnitude respectively for the run (i), N_0 is the unpolarized event rate (measured in events per OMON), and P_0 is the polarization parameter. Similarly for a run (j) with target spin down along y:

$$N_{j}^{-} = O_{j}^{-}N_{O}(1 - T_{j}^{-}P_{O}\cos \lambda) + \beta_{j}^{-}$$
 (2)

Since P_0 and N_0 are relevant to the elastic samples only, we now subtract out background and define

$$\eta_i^+ = N_i^+ - \beta_i^+ \tag{3}$$

where the subtraction is performed in the manner delineated in the previous section, event-by-event. The justification for not having a polarization term $(1 + T P_0 \cos \lambda)$ for background will be given in the next section, where it will be shown that the background was unpolarized:

$$\beta_{i}^{+}/O_{i}^{+} = \beta_{j}^{-}/O_{j}^{-}$$

Hence we can safely subtract out the backgrounds altogether and deal with the elastic samples n_i^+ , n_j^- only.

Summing over all positive runs (i) in equation (3) and over all negative runs (j) in equation (4) we obtain:

$$\sum_{i} \eta_{i}^{+} = N_{0} \sum_{i} O_{i}^{+} + N_{0} P_{0} \cos \lambda \qquad \sum_{i} O_{i}^{+} T_{i}^{+}$$
(5)

$$\sum_{j} \bar{\eta}_{j} = N_{0} \sum_{j} \bar{0}_{j} + N_{0} P_{0} \cos \lambda \sum_{j} \bar{0}_{j} T_{j}$$
 (6)

These equations may be solved immediately for N_o and P_o :

$$P_{O}(P_{LAB}, \Delta t) = \frac{1}{\cos \lambda} \frac{\sum O^{-} \Sigma \eta^{+} - \Sigma O^{+} \Sigma \eta^{-}}{\sum O_{j}^{-} T_{j}^{-} \sum \eta^{+}_{i} + \sum O_{i}^{+} T_{i}^{+} \sum \eta^{-}_{j}}$$
(7)

$$N_{O}(P_{LAB}, \Delta t) = \begin{array}{c} \sum_{j=1}^{\Sigma O^{-}T^{-}} \sum_{j=1}^{\Sigma O^{+}} \frac{1}{2} + \sum_{j=1}^{\Sigma O^{+}} \frac{1}{2} + \sum_{j=1}^{\Sigma O^{-}} \frac{1}{2} \\ \sum_{j=1}^{\Sigma O^{-}} \sum_{j=1}^{\Sigma O^{+}} \frac{1}{2} + \sum_{j=1}^{\Sigma O^{-}} \frac{1}{2} \\ \sum_{j=1}^{\Sigma O^{-}} \sum_{j=1}^{\Sigma O^{+}} \frac{1}{2} + \sum_{j=1}^{\Sigma O^{-}} \frac{1}{2} \end{array}$$
(8)

We have the desired expression for the polarization parameter in $P_O(\ P_{\rm LAB}, \Delta \, t)$. The differential cross section may be obtained from $N_O(\ P_{\rm LAB}, \Delta t)$, but additional information of the incident beam spectrum and acceptance corrections is necessary. These problems are considered in the next section in addition to a number of checks of the polarization measurement.

D. Checks of the Data

The extent to which the $\chi^2 \leq 10$ cut was appropriate and the extent to which the data were free of systematic errors were carefully tested. The analysis included consistency checks of the experimental measurement, checks of the binning scheme used to display the polarization, checks of the polarization parameter as a function of χ^2 cut, and checks of the data with previous work -- for both the polarization and differential cross section.

1. Checks of the experimental measurement:

The checks of the experimental measurement involved tests of neutron counter consistency, polarization uniformity

within the target, and stability of the polarization measurement with time.

Comparisons were made of the data from the neutron counter banks to determine if they gave similar results for the polarization parameter in the momentum transfer regions where they overlapped. To within statistics it was found that the long and short counters were consistent in their region of overlap $0.03 \le |t| \le 0.2(\text{GeV/c})^2$, and that all the shorts were consistent with one another in their common region $0.0 \le |t| \le 0.2(\text{GeV/c})$ (see Figure 22).

An important experimental question was whether the proton polarization was uniformly distributed over the volume of the target, or whether some regions, for example the center, were relatively depolarized. To test this the target was subdivided into nine sectors, breaking the data sample into nine parts depending upon event origin. The polarization parameter $P_{\rm O}$ was then calculated for each individual sector using only its constituent events (Figure 23). To within statistics the target was uniformly polarized.

The check of the stability of the polarization measurement with time was crucial because, over the six months in which the experiment was operational, data was taken in two separate intervals of one-and-one half months each. The polarization parameter was calculated for both of these periods individually, and the results are compared in Figure 24. The consistency of the Po values attests to the stability of the monitors used.

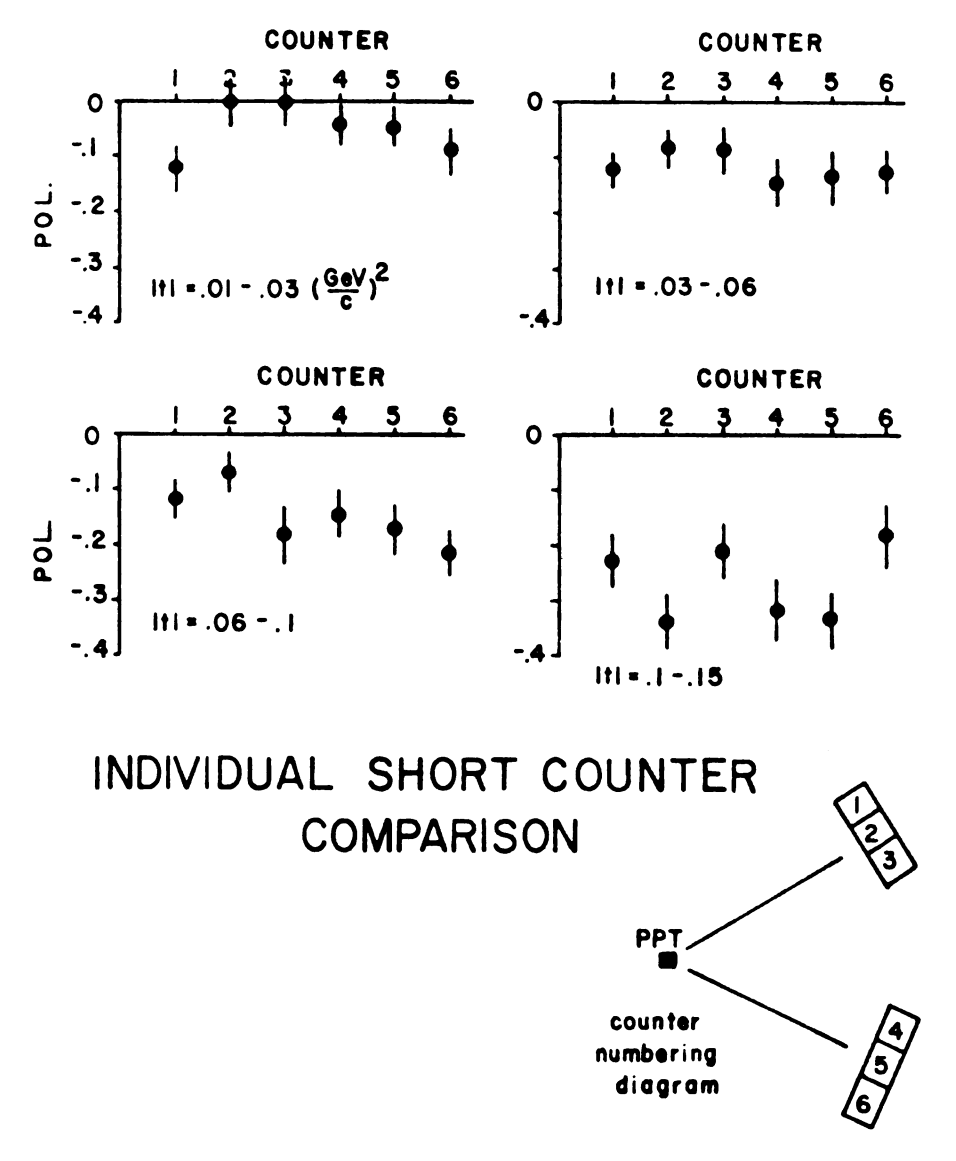
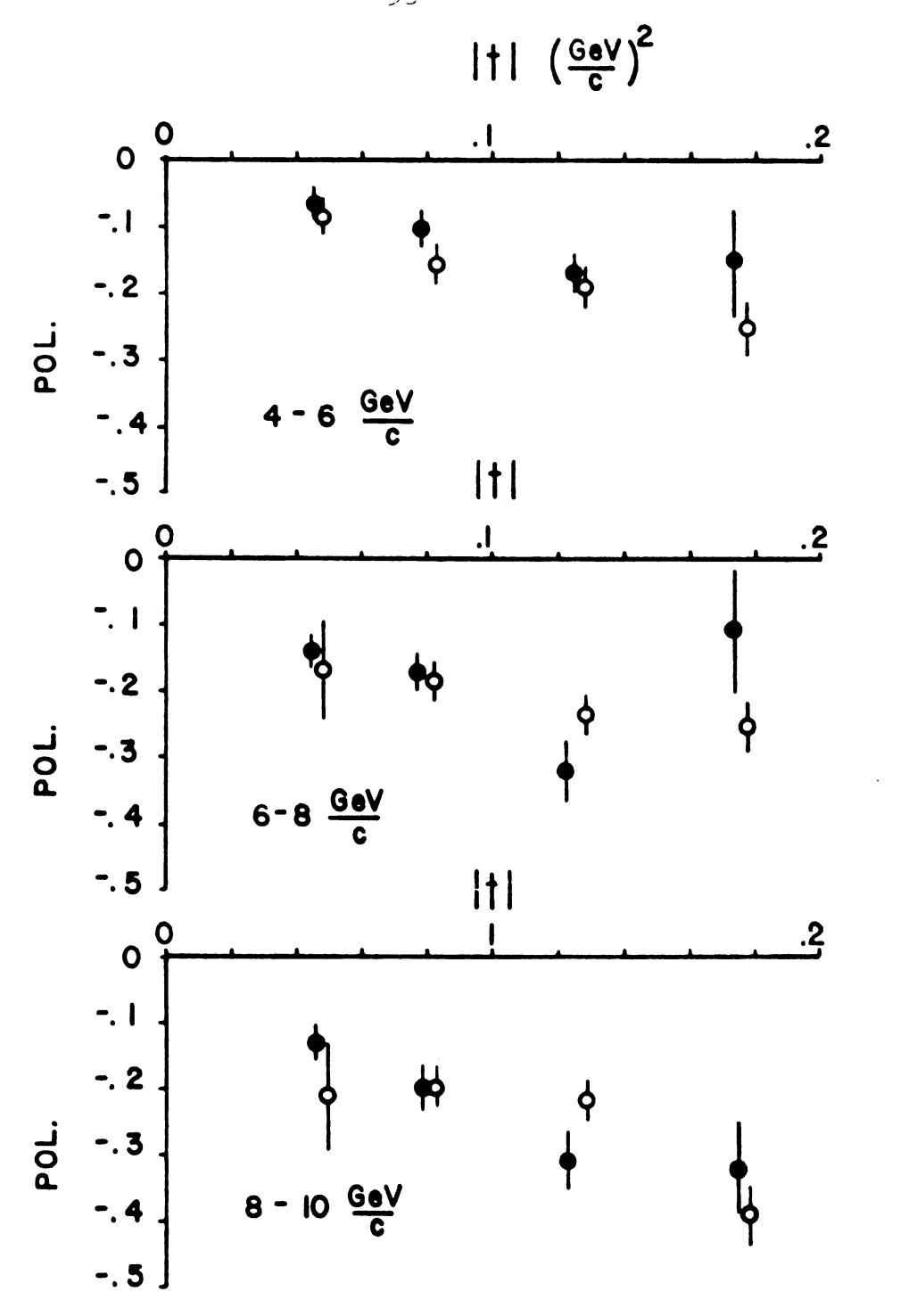


Figure 22a. Newtron Counter Consistency in the Region of Overlap for the Short Counters.



♦ SHORT AND ♦ LONG COUNTER COMPARISON

Figure 22b. Nextron Counter Consistency in the Region of Overlap for the Long and Short Counters.

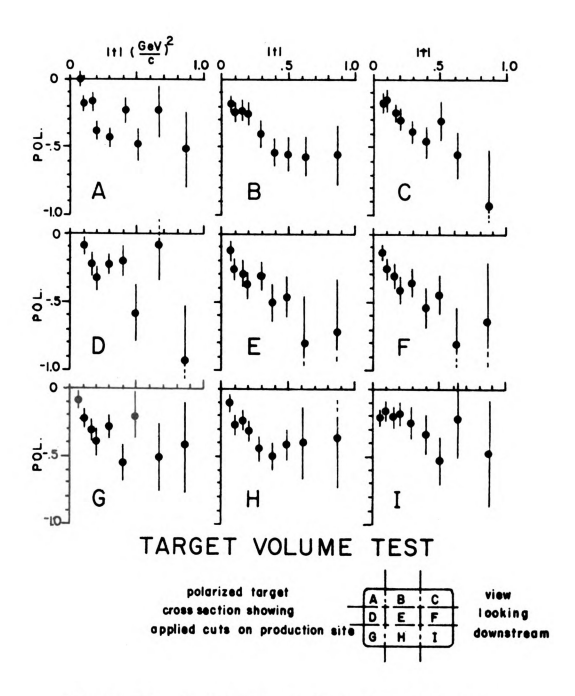
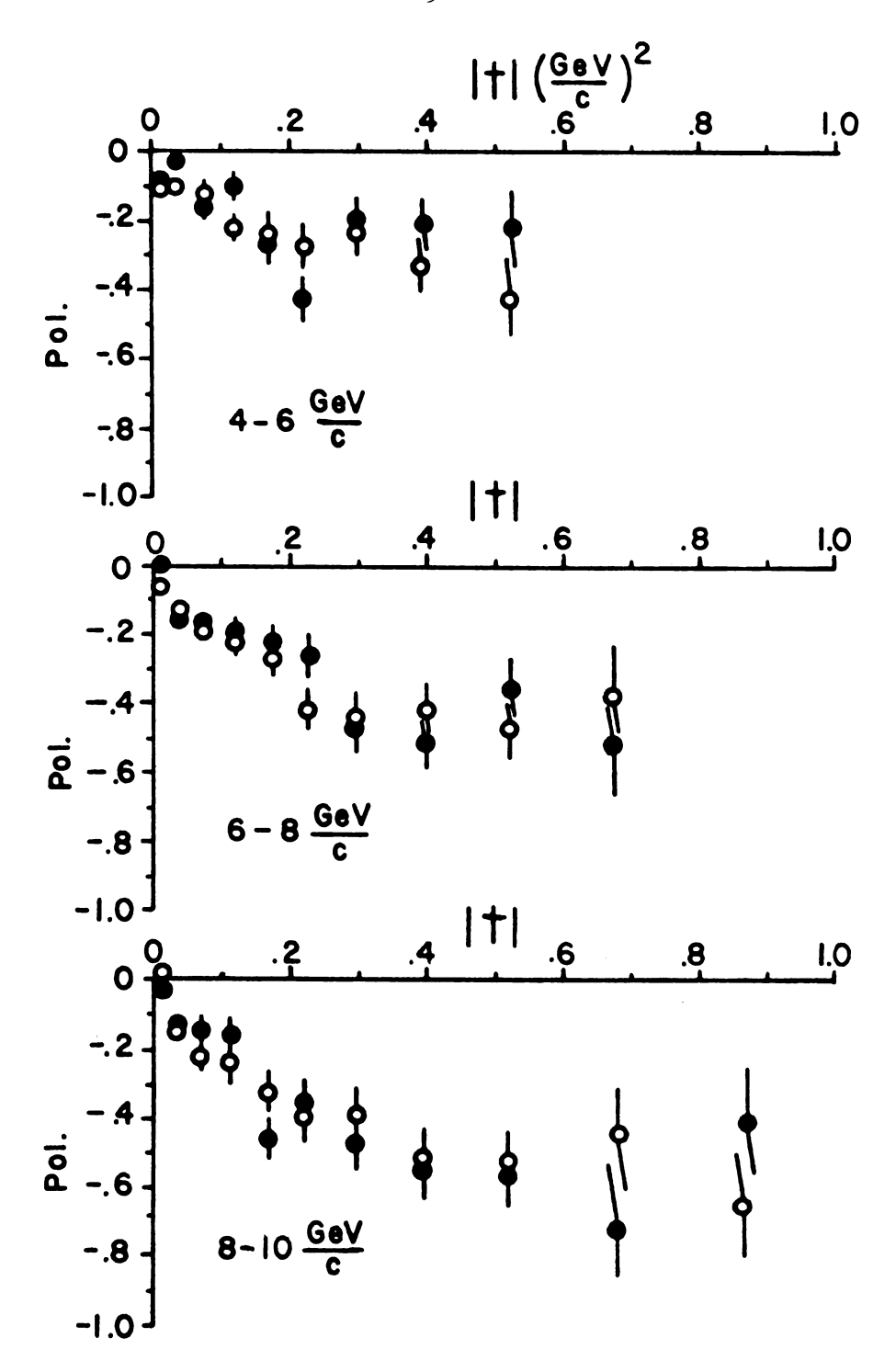


Figure 23. Uniformity of Polarization in the Target.

Figure 24. Comparison of the Polarization Parameter Values, Calculated for Each of the Data Taking Periods Individually: Phase I (Sept-Oct., 1971) and Phase II (Nov-Dec.,1971).



♦ PHASE I → COMPARISON

Figure 24

2. Checks of the Binning Scheme:

The binning scheme used in plotting the polarization parameter is valid only if the |t| resolution of the experiment is much smaller than the bin size chosen. To show that this was indeed the case, our resolution as a function of |t| is plotted in Figure 25 and is also shown on a plot of P_0 vs |t| as horizontal error bars.

To be certain that the binning scheme in | t | did not mask any important structure, a complementary choice was made in which the data were rebinned into intervals centered mid-way between the old ones. Within statistics the two binning schemes were equivalent (Figure 26).

3. Checks of the Polarization as a function of x^2 :

The first question was whether or not the background was polarized. Examination of Figure 27 reveals that the polarization for both counter types disappears for values of χ^2 much above 10. The polarization for a sample of 30,000 events with 15 $\leq \chi^2 \leq$ 100 was determined to be 2.0 \pm 3.0% overall (consistent with being unpolarized, and hence the background rates were equal: $g^+/0^+ = g^-/0^-$.

That the polarization calculated for the elastic sample did not change for more refined cuts on χ^2 is shown in Figure 28 where the polarization parameter is plotted for $\chi^2 \le 2$, 4, 6, 8, 10. The results show that retaining the elastic events with $\chi^2 \le 10$ was a good choice.

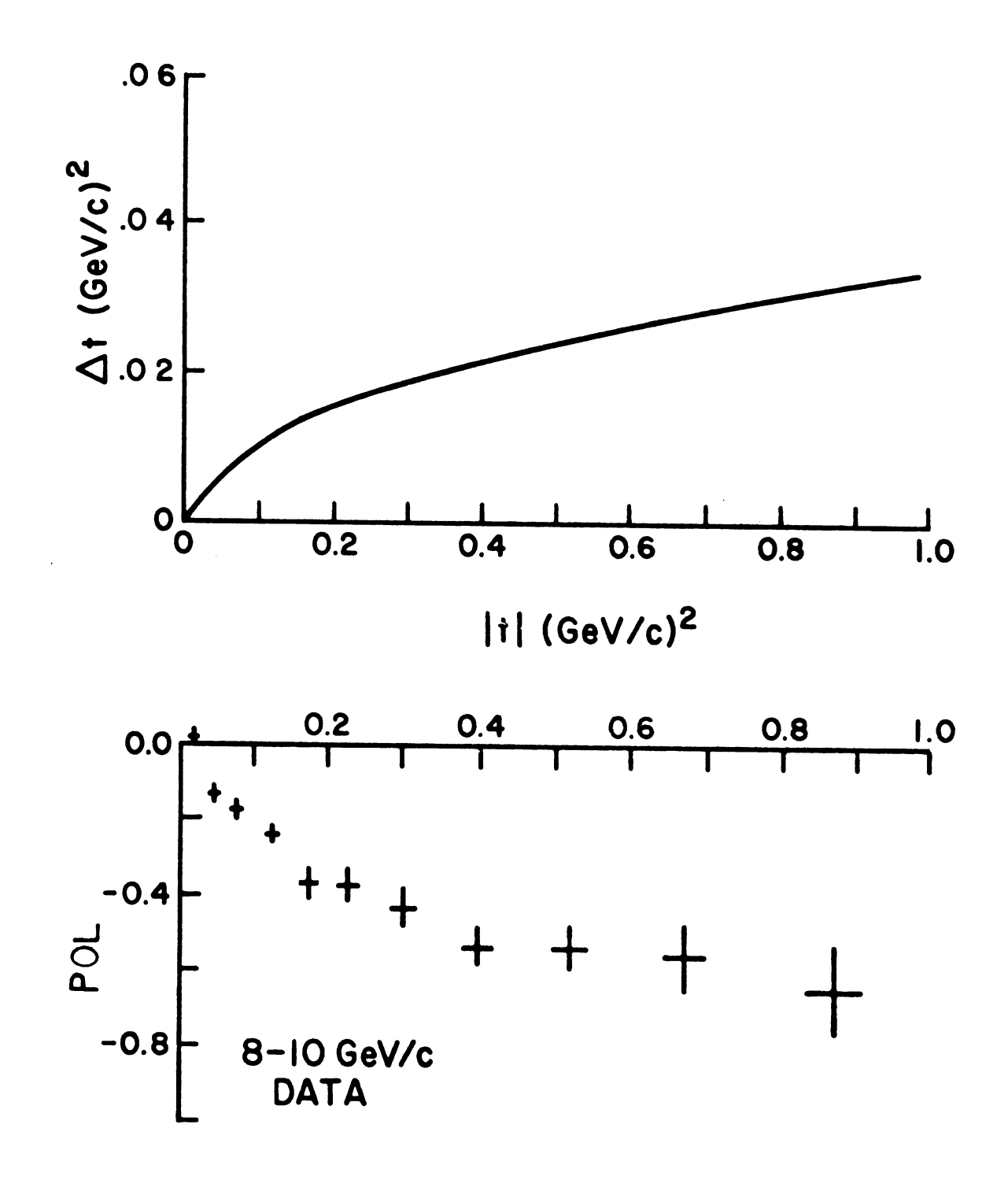
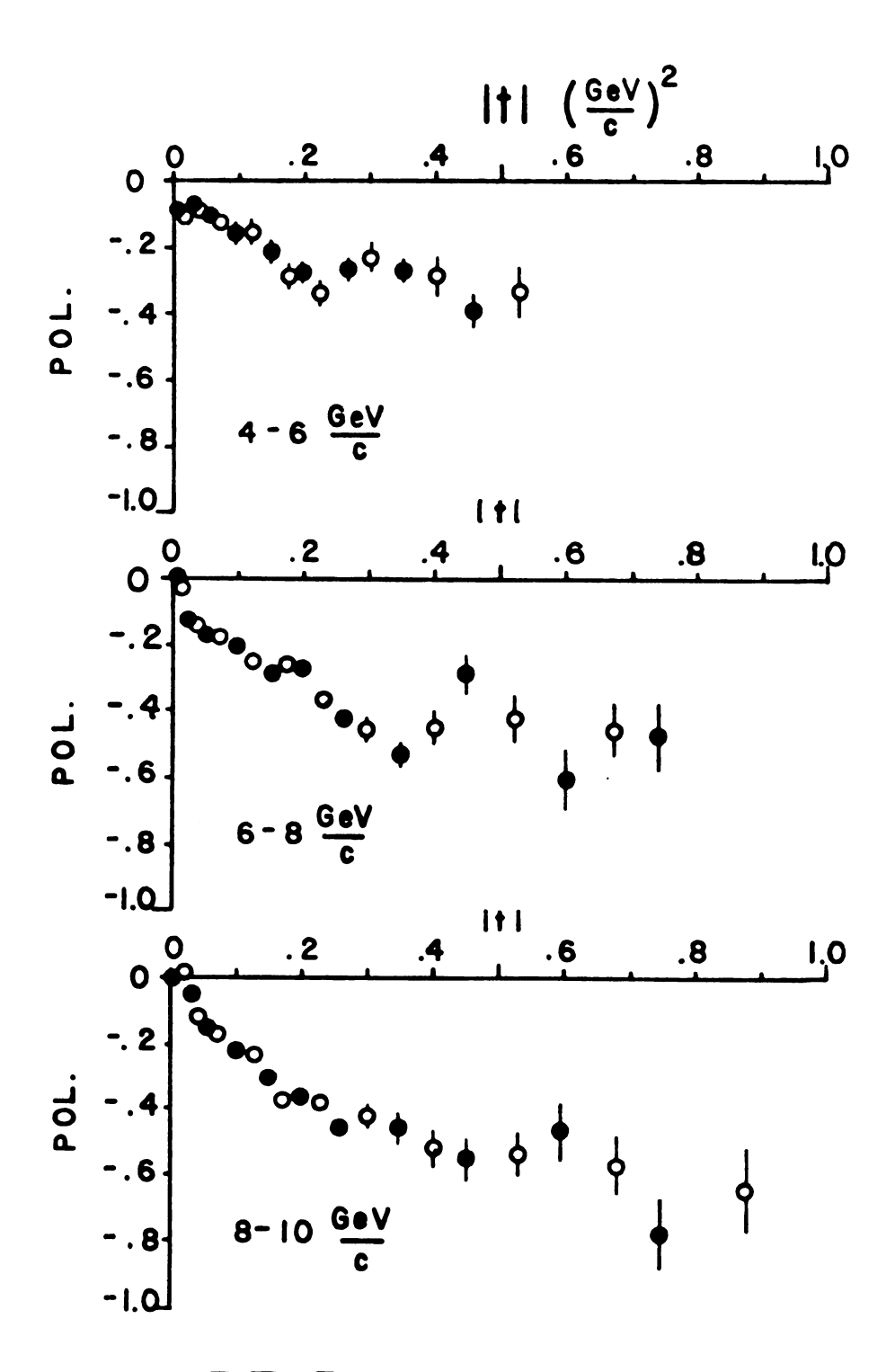


Figure 25. Experimental |t| -Resolution



RE-BINNING TEST

Figure 26. Polarization Parameter Plotted for Two Different Binning Schemes: (a)Actual Scheme used, (b) Complementary Scheme.

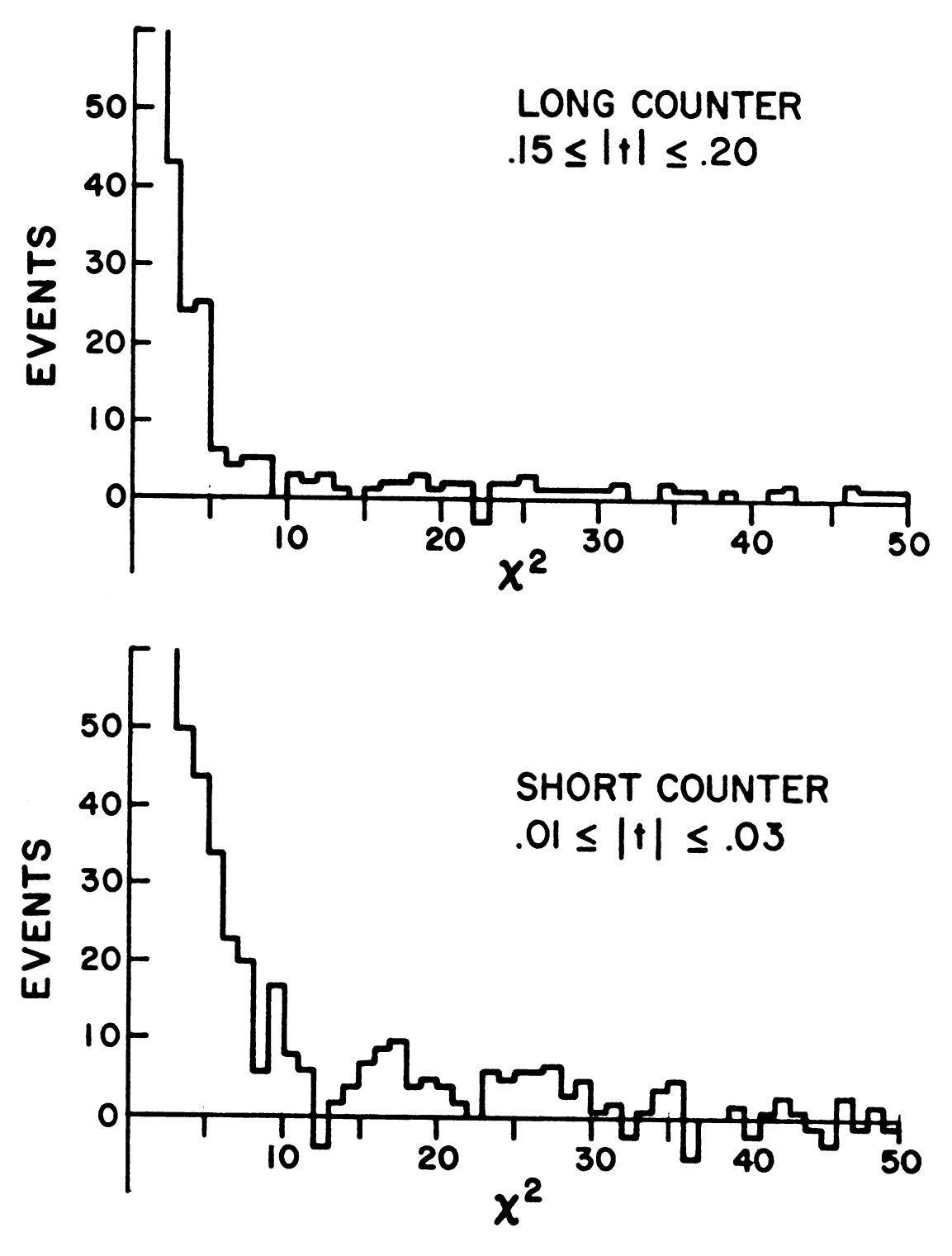


Figure 27. $(N_- - N_+)$ vs χ^2 for $0 \le \chi^2 \le 50$. The Factor $(N_- - N_+)$ is Essentially Poexcept for Normalization.

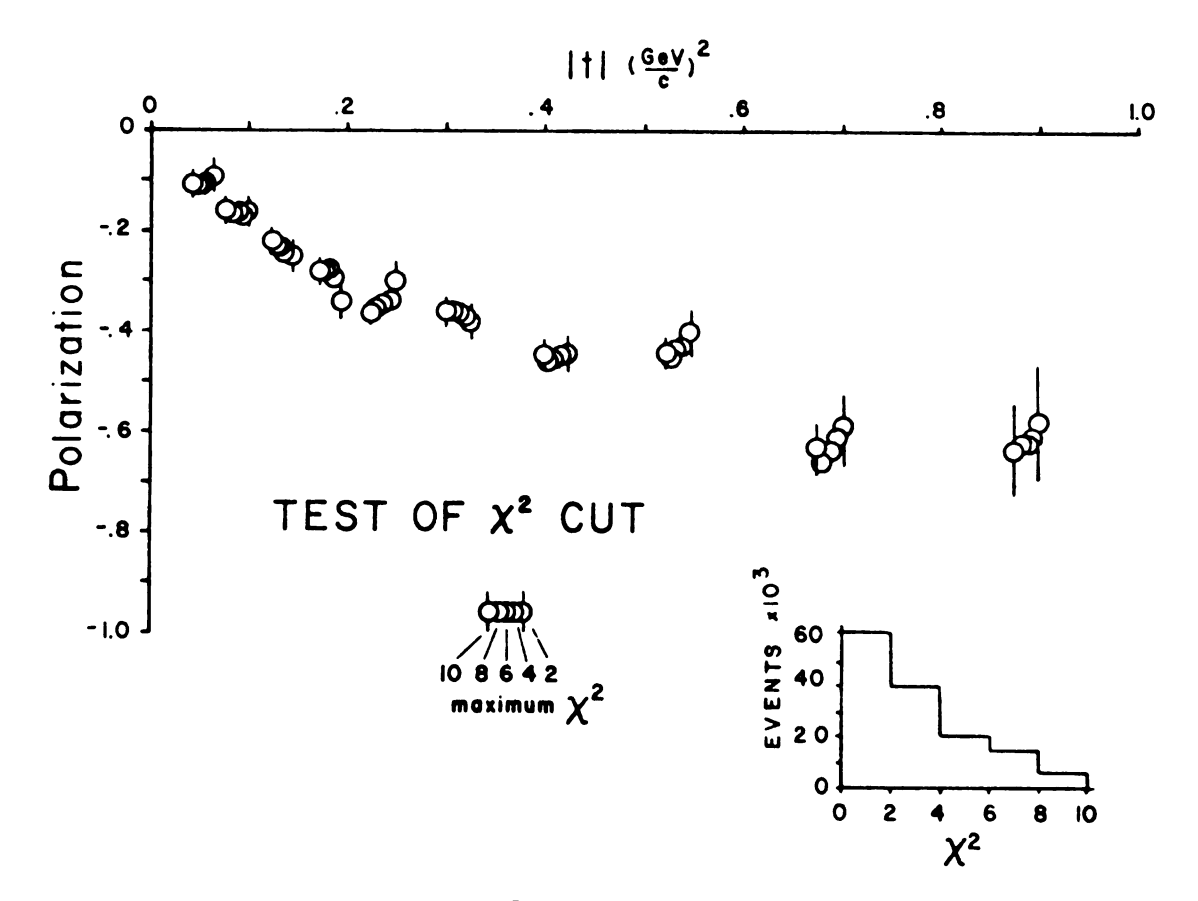


Figure 28. $P_0 \vee s \chi^2$ for $\chi^2 - 2, 4, 6, 6, 10$.

4. Checks on consistency with other experiments:

The method of computing the polarization parameter discussed in Section C is different than that of Robrish, et al., 25 but the two techniques turn out to be numerically equivalent at our level of statistics as shown in Figure 29, where the polarization is determined from our data using both schemes. Once this check was made, our polarization data were then compared with the data of Robrish, et al., for the two momentum bins where the experimental data overlap (Figure 30). Although the momentum coverage is slightly different, the results are consistent.

Finally the data samples for positive and negative target polarization were used to calculate $N_{0}(\Delta s, \Delta t)$, the unpolarized event rate, and hence the differential cross section.

The experimental expression for do/dt is:

$$\frac{d_{\sigma}}{dt} \left(\Delta P_{LAB}, \Delta t \right) = \frac{N_{O}(\Delta P_{LAB}, \Delta t)}{I(\Delta P_{LAB})} \cdot \frac{1}{\sigma_{TGT}} \cdot \frac{1}{C_{N}(\Delta P_{LAB}, \Delta t)} \cdot \frac{1}{C_{D}}$$

where the several terms are defined as follows:

 $N_{\text{O}}(\Delta P_{\text{LAB}}, \Delta t)$ is the unpolarized event rate calculated in Section C.

I(${}^{\Delta P}_{\rm LAB})$ is the incident beam flux measured in neutrons per OMON (see Appendix I).

 $\sigma_{\rm TGT}$ is the effective number of target centers per unit area (2.04 x $10^{23}/{\rm cm}^2$).

 $C_{\mathrm{N}}(\Delta P_{\mathrm{LAB}}, \Delta t)$ is a composite correction factor for the neutron arm given as:

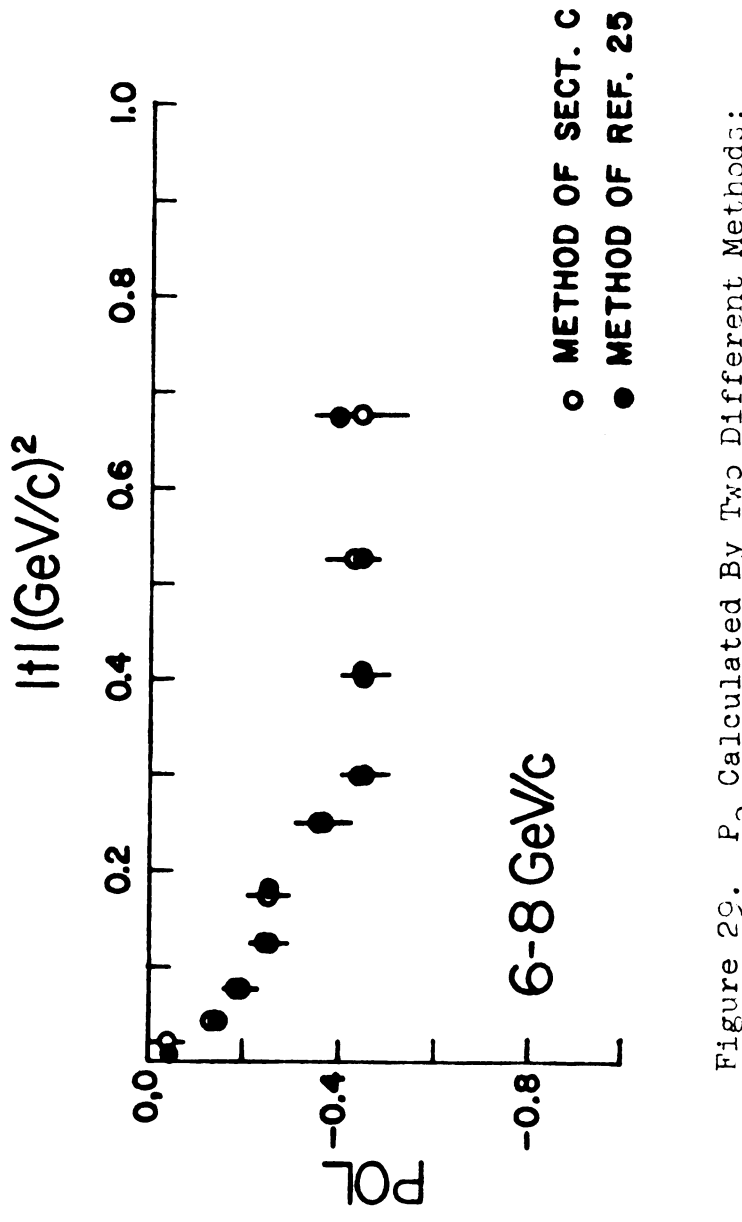
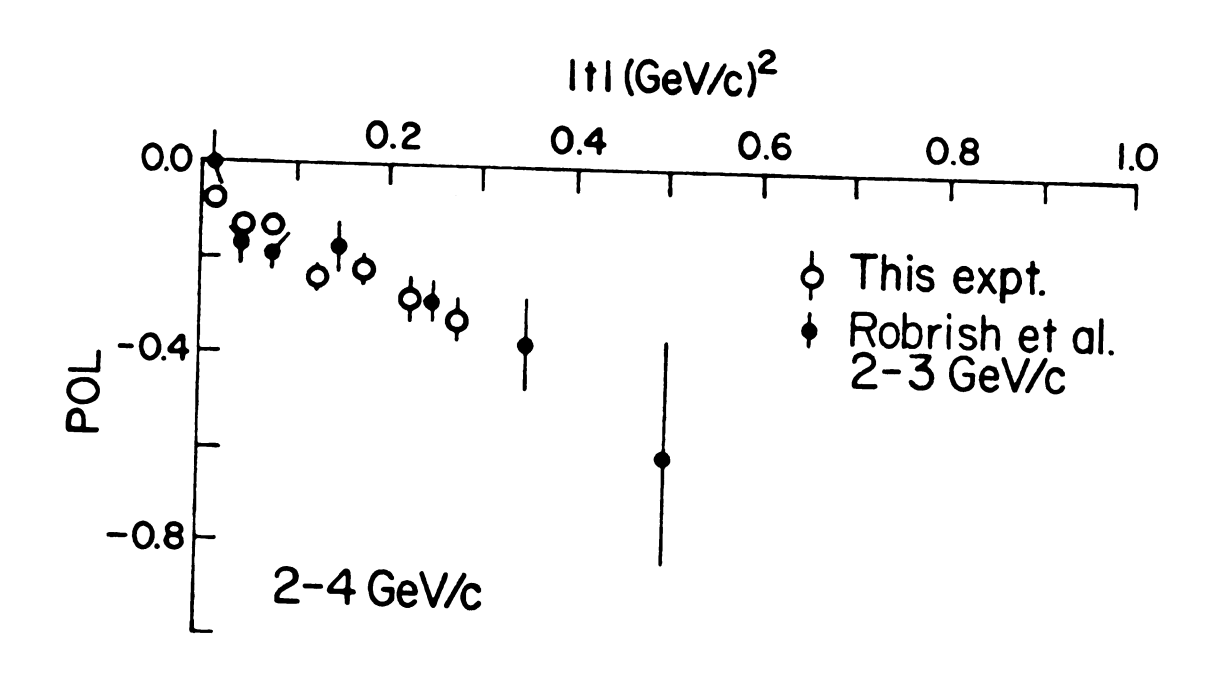


Figure 29. P_o Calculated By Two Different Methods: (a) Method Shown in Chapter IV, (b) Method Used in Reference 25.



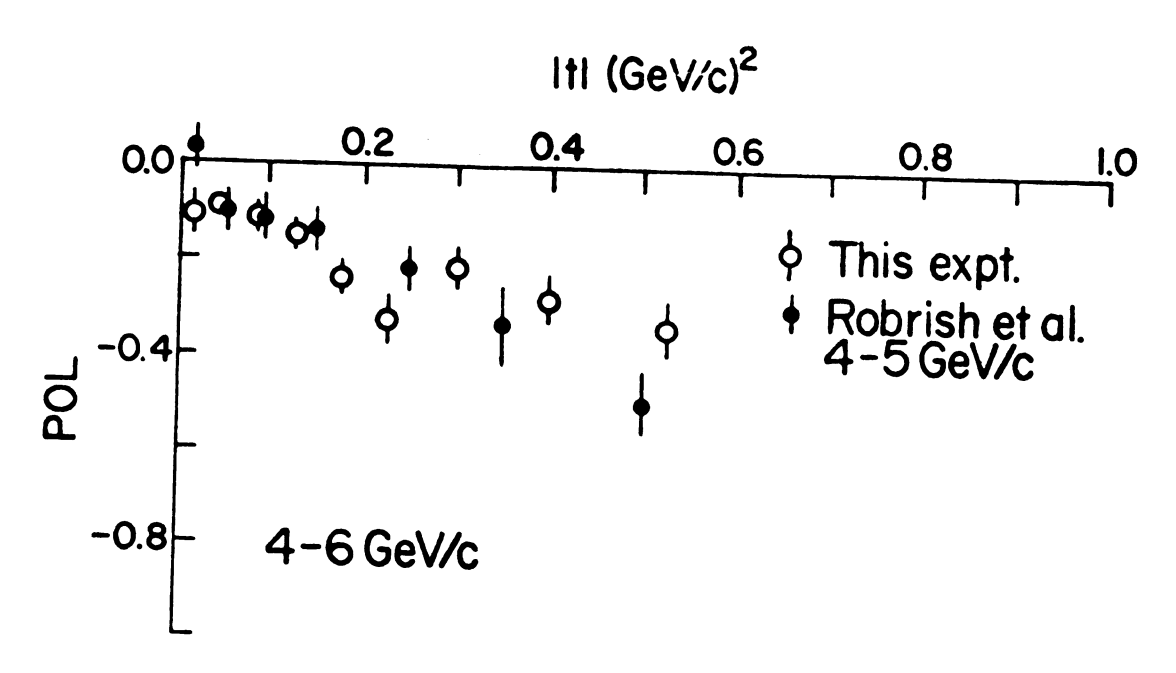


Figure 30. Comparison of the Polarization with Previous Work: (a) This Experiment, (b) Data From Reference 1.

 $C_N(\Delta P_{LAB}, \Delta t) = A(\Delta P_{LAB}, \Delta t) d\Omega(NTYPE, \Delta t) T(\Delta t) E(\Delta t)$ where:

- $A(\Delta P_{\rm LAB}, \Delta t)$ is the neutron counter acceptance for the bin $(\Delta P_{\rm LAB}, \Delta t)$. (See Appendix D).
- $d\Omega$ (NTYPE, Δ t) is the solid angle subtended by the particular neutron counter array (NTYPE) at the target.
- $T(\Delta t)$ is the target absorption correction calculated for the long and short neutron counters (see Appendix D).
- $E(\Delta t)$ is the detection efficiency of the neutron counters. (See Appendix D).
- c_p is a composite correction factor for the proton arm given as: $c_p = c_{p1} \cdot c_{p2}$

where:

- C_{pl} is the correction for pulse height cuts on the two dE/dx counters in the proton arm: 0.95 for S1 and 0.98 for S2.
- C_{p2} is the correction for the spark chamber spectrometer efficiency (0.98).

Since the differential cross section was to be used as a check on the polarization measurement, several simplifying assumptions were made: First, the incident momentum spectrum $I(\Delta P_{LAB})$ was assumed to be the same as that measured by E. L. Miller, et al., ⁵ a fair assumption since the ZGS internal targeting scheme was the same for both experiments (quoted error on $I(\Delta P_{LAB})$ is $\pm 10\%$). Second, the absorption $T(\Delta t)$ of

the slow recoil neutrons from the charge exchange process (by cryostat walls, liquid helium, target veto counters, etc.) was calculated for the horizontal (x, z) scattering plane only; the same absorption was presumed to hold for neutrons emitted at various angles λ above and below the horizontal plane, where $\lambda = 17^{\circ}$. The uncertainty introduced into do/dt by this assumption is |t| dependent, worst for small |t| where neutrons have a better than 50% chance of being lost, and best for higher $|t| \stackrel{>}{\sim} 0.1(\text{GeV/c})^2$ where the absorption becomes small. Estimated uncertainty in the value of the absorption is $\delta T/T = \pm 10\%$ for $0.01 \le |t| \le 0.1(\text{GeV/c})^2$ and δT/T =±5% for larger |t| values. Third, the neutron counter acceptance A(P_{LAR} , Δt) was estimated from the graph in Appendix D rather than from an event monte carlo, with uncertainty $\delta A/A = \pm 5\%$. Hence the differential cross section calculated here should have an uncertainty of roughly ±20%. Since the above approximations hold best for events detected in the long neutron counters, the cross sections obtained should be most trustworthy for $|t|^2 = 0.1(\text{GeV/c})^2$.

The results of this analysis were compared with the Miller data (Figure 31). For $|t| \ge 0.1 (\text{GeV/c})^2$, the two sets of data agree in both P_{IAB} and |t| dependence to within 20%. On the other hand, the small |t| short neutron counter data, sensitive to the slowest recoil neutrons and events above and below the horizontal plane, do not show as good an agreement indicating a failure in the approximation

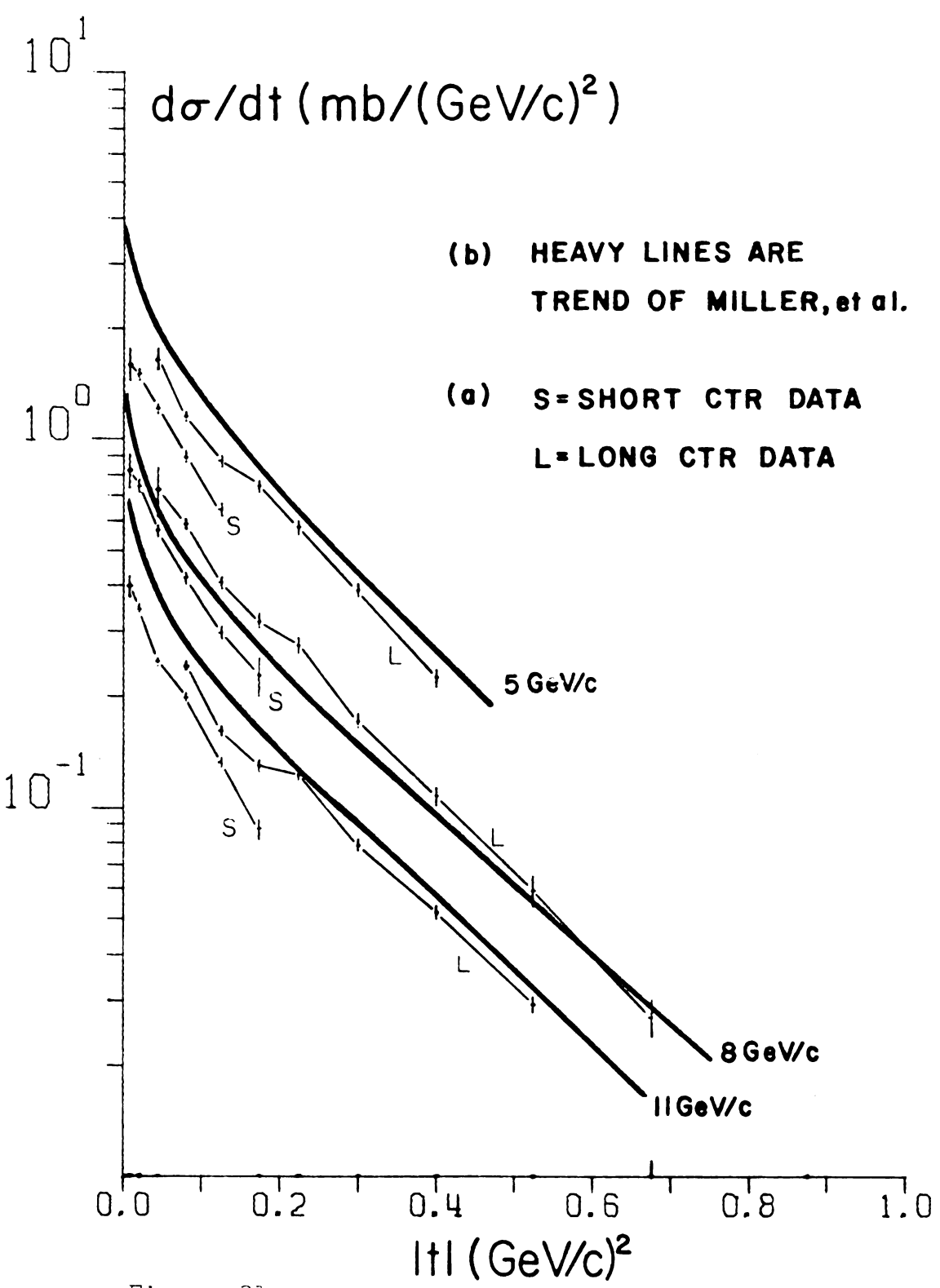


Figure 31. Comparison of the Differential Cross
Section with Previous Work: (a) Approximate Cross Section from this Experiment,
(b) Data From Reference 5.

arguments for small |t|. However in the region where the approximations hold best, $|t| \stackrel{>}{\sim} 0.1 (\text{GeV/c})^2$, the results suggest that we really have np charge exchange events.

CHAPTER IV

PRESENTATION OF THE DATA

The 300,000 elastic events with χ^2 - 10 were then used to calculate the polarization parameter. The results, binned into five different intervals of laboratory momentum, are presented in Table 2 and Figures 32-36. The distinctive features are: For fixed energy, the polarization magnitude grows monotonically with |t|; for fixed momentum transfer |t|, a slight energy dependence is exhibited, with evidence of a trend toward larger polarization magnitudes as P_{LAB} increases. In particular if one draws the empirical curve suggested by Robrish, et al.

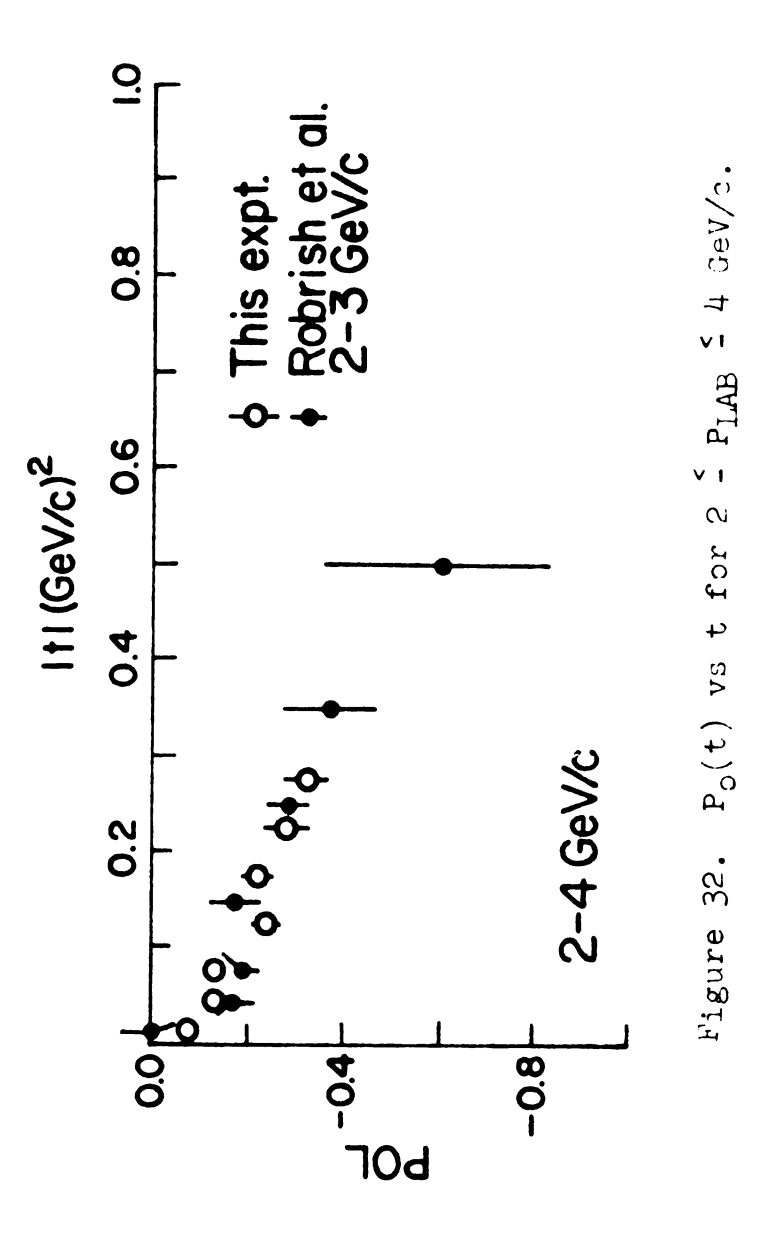
$$|P_0| = \frac{\sqrt{|t|}}{2m_n}$$

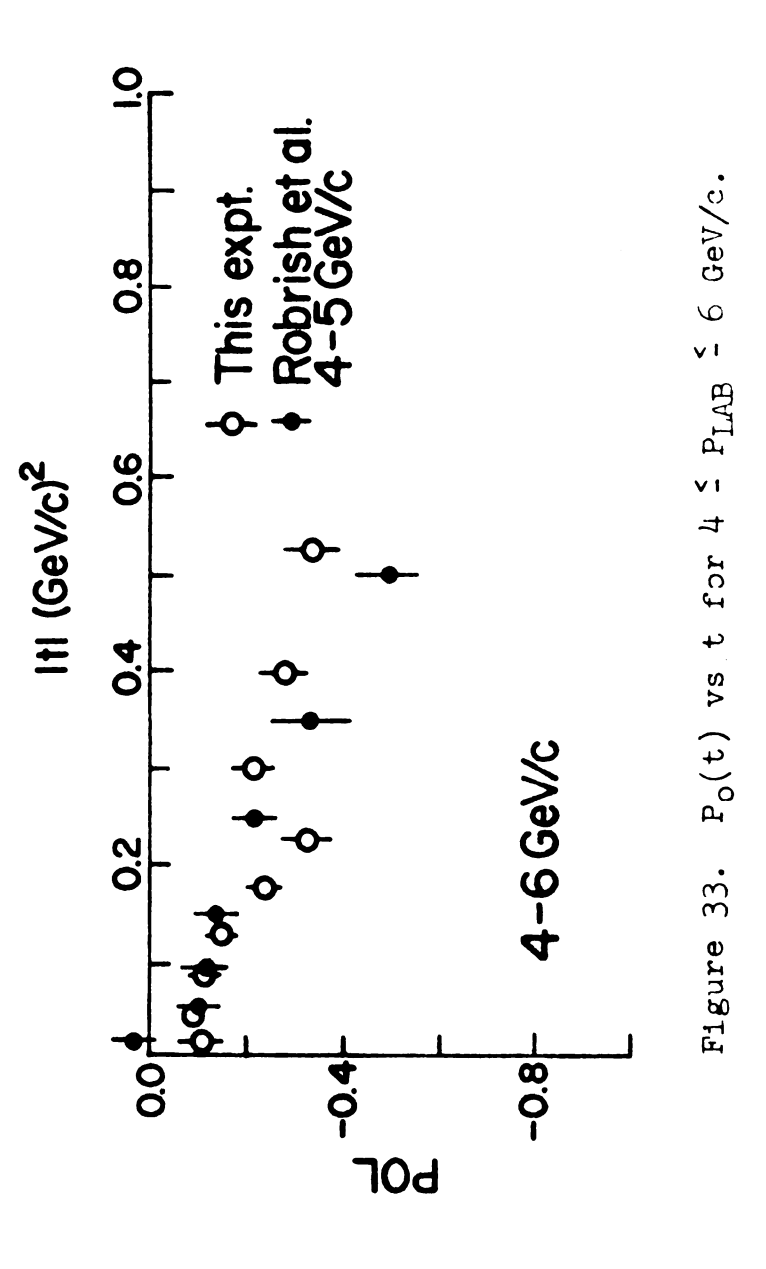
on the plots of the data (Figure 37), the agreement is no longer good for $P_{LAB} > 6$ GeV/c, indicating a trend toward rising polarizations. For example at $|t| = .7(\text{GeV/c})^2$, $\Delta |P_0|/\Delta P_{LAB} = .03(\text{GeV/c})^{-1}$ for the momentum range $4 \le P_{LAB} \le 12$ GeV/c. Attempts at parametrizing the energy dependence of P_0 shown in Figure 38 by simple functions of P_{LAB} all resulted in equally poor x^2 values for the fits. Hence no definitive conclusions on the exact form of the energy dependence were drawn. A three dimensional summary of $P_0(P_{LAB}, \Delta t)$ is shown in Figure 39.

Table 2. Table of Polarization Data

\dr	APLAB	5 - 4	9 - 4	9 - 8	8 - 10	10 - 12
.0103 (a)*	(a)*	079 ±.027	101±.036	026±.038	+.006 ±.038	0 +.035
.0306	(q)	121 ±.019	078±.028	139±.034	128±.034	156±.034
.0610	(c)	140 ±.019	115±.020	181±.020	175±.020	190±.020
.1015	(p)	244 ±.025	151±.028	250±.030	230±.030	285±.033
.15 .20	(e)	210 ±.037	240 +.040	250±.046	367±.048	376 ±.049
.2025	(f)	282 ±.054	325±.047	364±.053	375 ±.050	442 ±.050
.2535	(g)	319 ±.064	212 ±.041	-,450±,046	-,427 ±,046	388±.048
.3545	(h)		276 ±.056	450±.058	523 ±.055	529 ±.059
.4560	(1)		33 8±.033	417±.068	537 ±.067	410 ±.072
.6075	(j)			442±.108	555 ±.106	797 ±.125
.75-1.0	(K)				643 ±.114	509 ±.155

 * Letters in parenthesis refer to Figure 38.





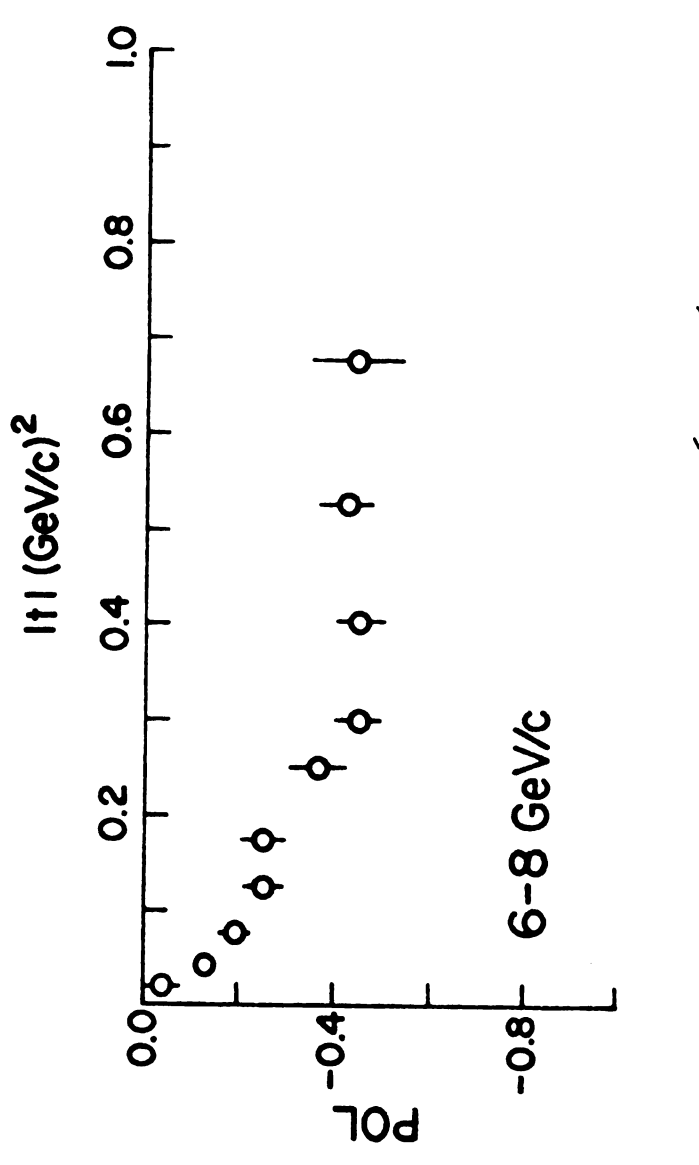
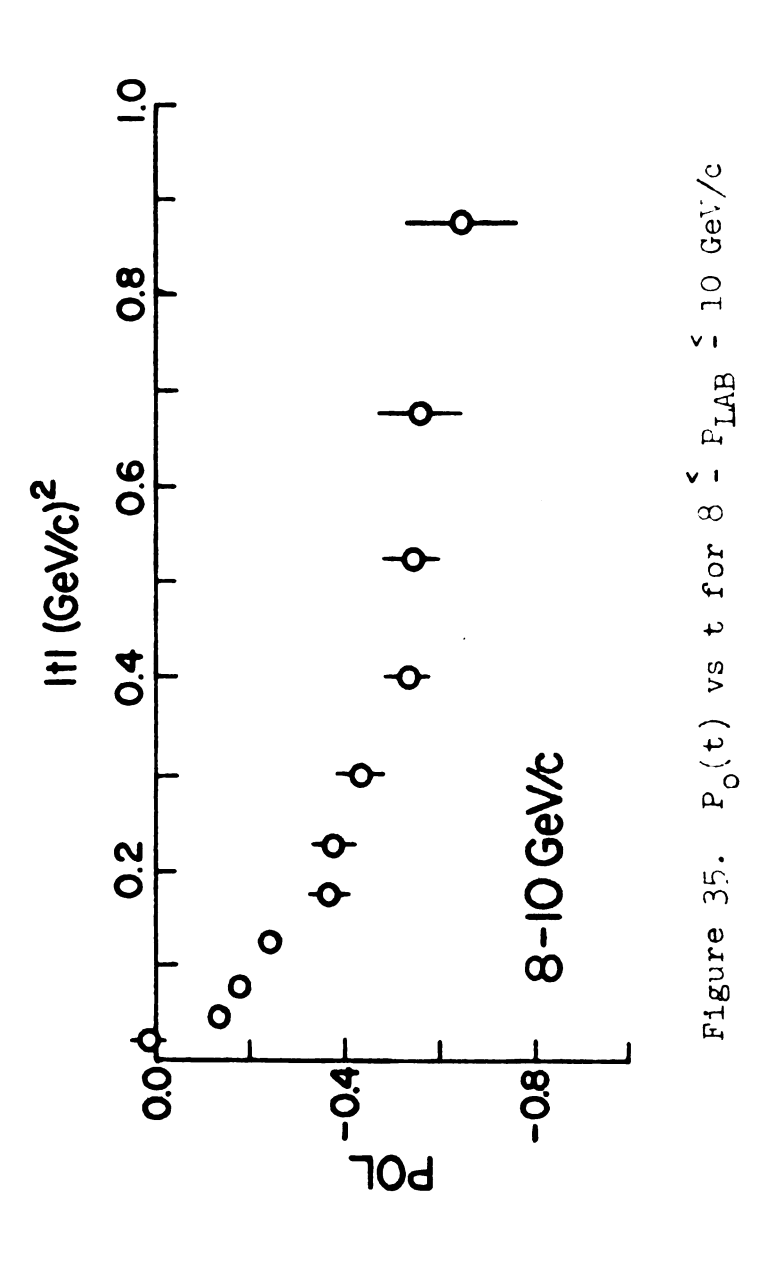
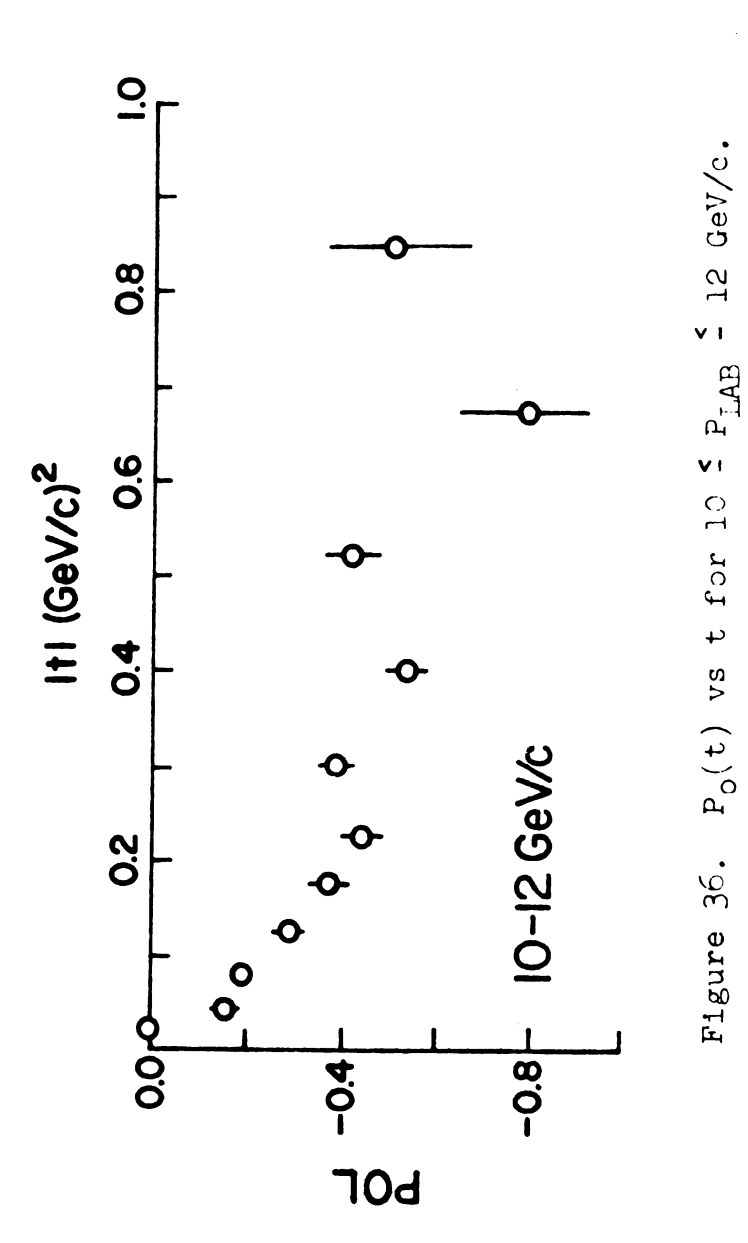


Figure 34. $P_o(t)$ vs t for 6 2 P_{LAB} 2 8 GeV/c.





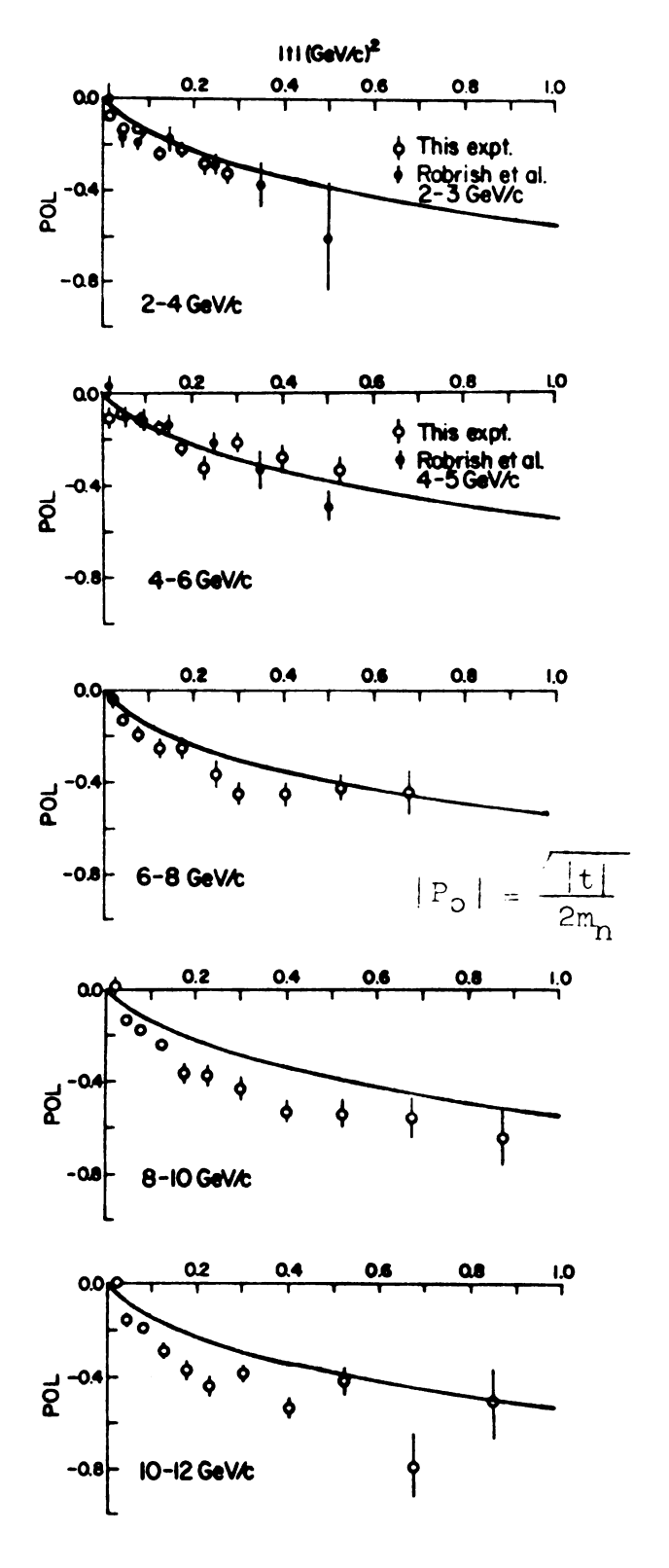


Fig. re 3%. Approximate Energy Variation of $P_{o}(t)$ as $P_{I,AB}$ Increases From 2-12 GeV/c.

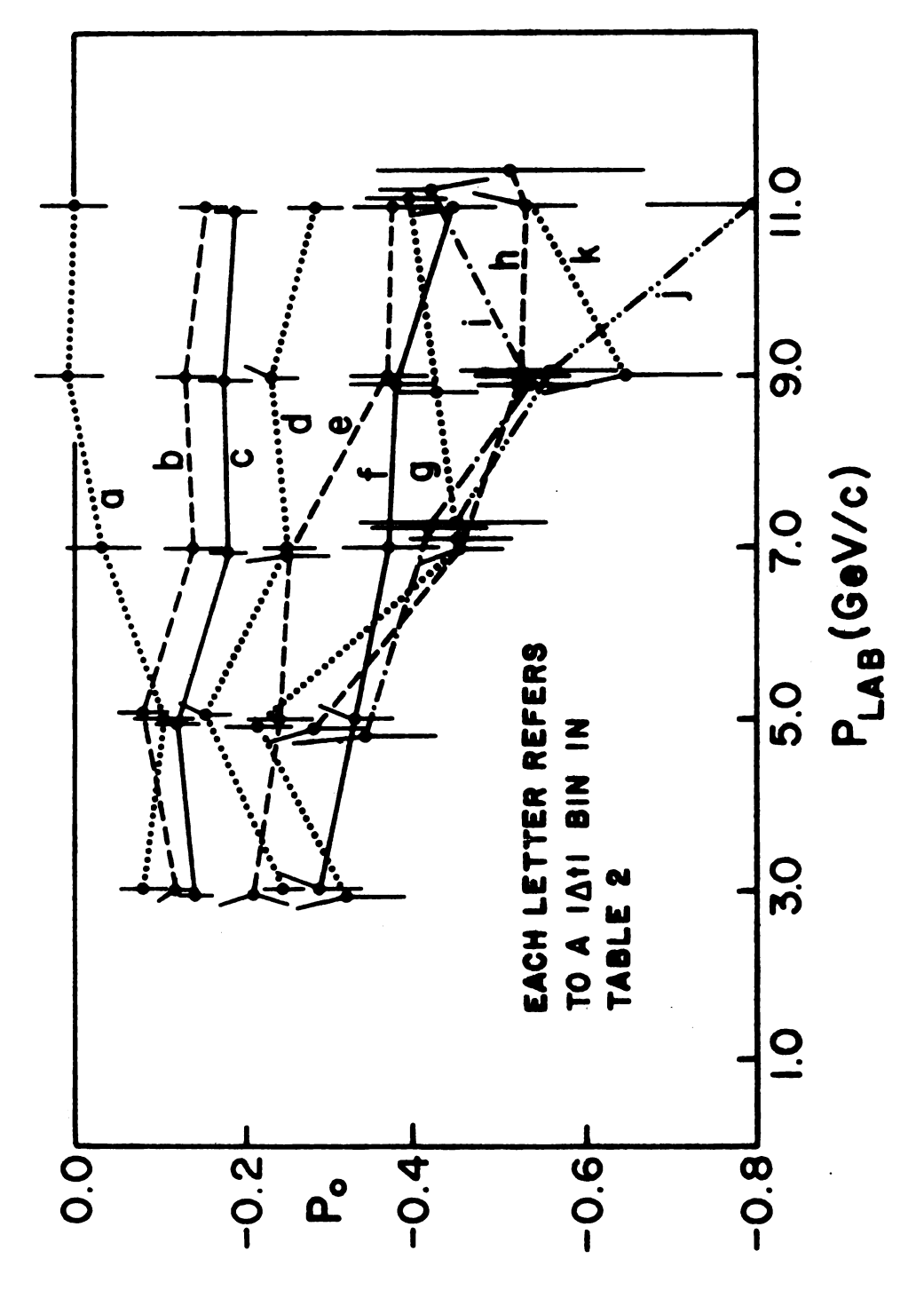


Figure 38. $P_{2}(P_{LAB})$ vs P_{LAB} for 0.01 \leq | t| \leq 1.0.

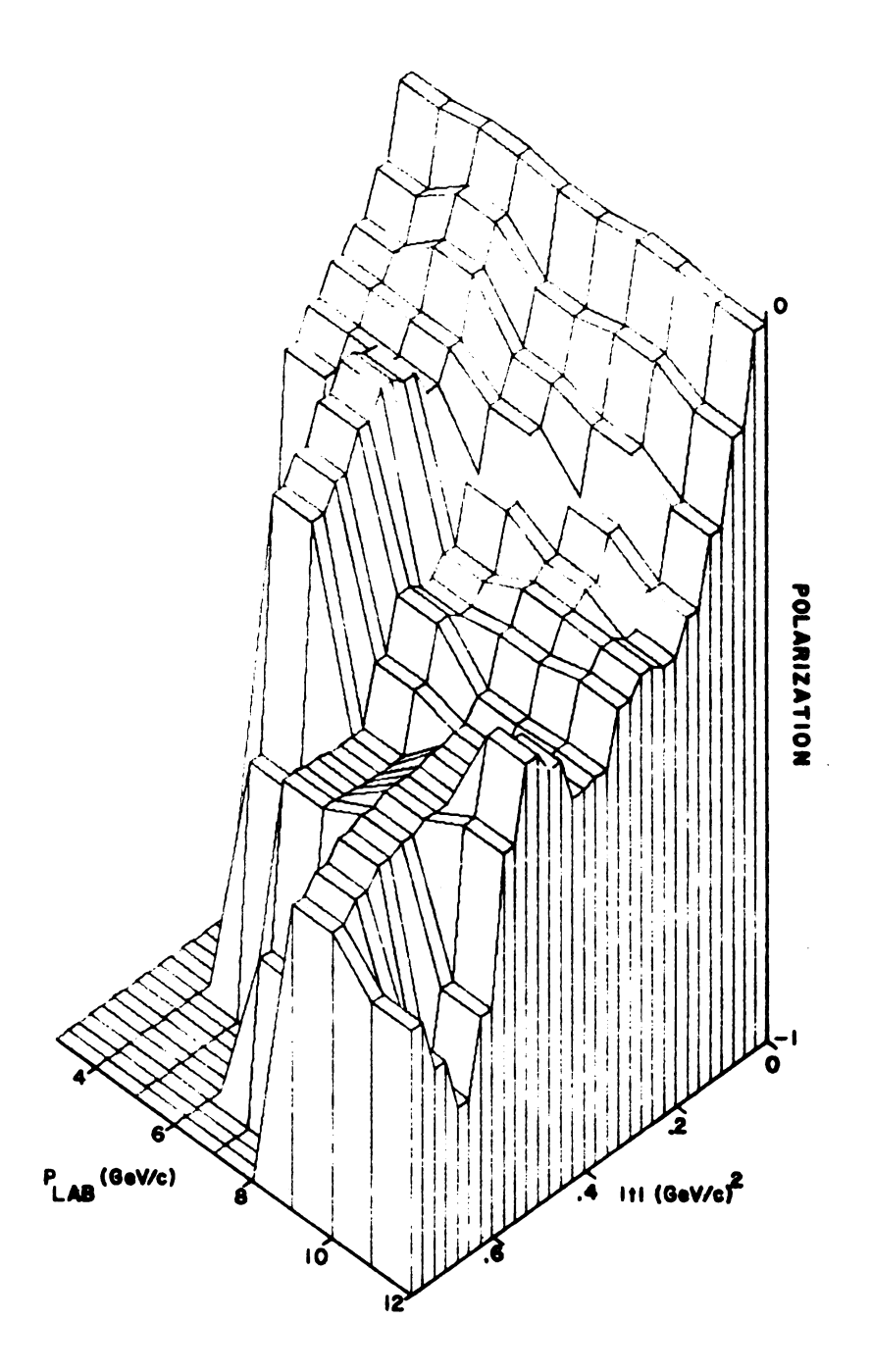


Figure 39. $P_0(P_{\rm LAB},t)$ vs $P_{\rm LAB}$ and |t|, Showing Experimental Acceptance.

CHAPTER V

Theoretical Interpretation

A. Preliminaries:

A correct theoretical description of the np \rightarrow pn system must reproduce the polarization parameter which is large $(|P_0| \sim 0.6 \text{ at } |t| \sim 0.6 (\text{GeV/c})^2)$ and essentially energy independent, must reproduce both the t and s dependence of the differential cross section, and must reproduce the polarization and differential cross section for the line reversed reaction $\bar{p}p \rightarrow \bar{n}n$.

The reaction np + pn involves two particles of spin 1/2 in both the initial and final states. If one writes down a transition amplitude $\phi = {}^{\lambda}_{3}{}^{\lambda}_{4} | M | {}^{\lambda}_{1}{}^{\lambda}_{2} > \text{ where the } {}^{\lambda}_{j}$ are the helicities of the external nucleons (see Figure 40), then one can construct 16 possible s-channel helicity amplitudes. However symmetry of the strong interaction under time reversal, parity, angular momentum, and isospin conservation reduce this number to five that are linearly independent. The conventional choices 27 for these five are:

		N	x
φ ₁ =	<++ m ++ >	0	0
ტე =	: <++ m >	0	2

$$\phi_{3} = \langle +-|m| +- \rangle \qquad 0$$

$$\phi_{4} = \langle +-|m| -+ \rangle \qquad 2$$

$$\phi_{5} = \langle ++|m| +- \rangle \qquad 1$$

where N = $|(\lambda_4 - \lambda_2) - (\lambda_3 - \lambda_1)|$ is the net helicity flip in the diagram, and x = $|\lambda_4 - \lambda_2| + |\lambda_3 - \lambda_1| - N$.

The differential cross section and polarization parameter are composed of bilinear combinations of these helicity amplitudes:

$$\frac{d\sigma}{dt} = \frac{1}{128\pi P_{cms}^2 s} \sum_{i=1}^{4} |\phi_i|^2 + 4|\phi_5|^2$$
 (1)

$$P_0 \frac{d\sigma}{dt} = \frac{2 \text{ Im} \phi_5^* \phi_0}{2}$$
, where $\phi_0 = (\phi_1 + \phi_2 + \phi_3 - \phi_4)$ (2)

It should be noted that the relative phase between ϕ_5^* and ϕ_0 is a crucial quantity. For the case in which ϕ_5^* , ϕ_0 are at right angles in an Argand diagram, $P_0 d\sigma/dt$ is maximized, conversely a relative colinearity of ϕ_5^* , ϕ_0 will imply very small polarization values.

Each helicity amplitude ϕ_j is a superposition of allowed particle exchange amplitudes. In particular for a π -meson to be exchanged, the equal masses of the proton and neutron require a spin flip at each nucleon vertex, restricting the pion to the ϕ_2 and ϕ_4 amplitudes only. Other leading exchanges, such as the natural spin-parity ρ and A_2 in general contribute to all five helicity amplitudes.

$$m_{\lambda,\mu}^{\text{TOTAL}}(s,t) = n_{\lambda} \frac{p_{\lambda} \lambda_{2}}{n_{\lambda} \lambda_{1}} \frac{n_{\lambda} \lambda_{4}}{p_{\lambda} \lambda_{3}}$$

Figure 40. Helicity Picture for n+p → p+n

$$\begin{split} \mathsf{M}_{\lambda,\mu}^{\mathsf{BORN}}(s,t) &= \frac{\mathsf{p}}{\mathsf{n}} \frac{\mathsf{p}}{\mathsf{p}} \\ \mathsf{M}_{\lambda,\mu}^{\mathsf{WEAK}}(s,t) &= \frac{\mathsf{p}}{\mathsf{n}} \frac{\mathsf{p}}{\mathsf{n}} \frac{\mathsf{p}}{\mathsf{p}} \frac{\mathsf{n}}{\mathsf{n}} \\ \mathsf{M}_{\lambda,\mu}^{\mathsf{QUASI-}}(s,t) &= \frac{\mathsf{p}}{\mathsf{n}} \frac{\mathsf{p}}{\mathsf{n}} \frac{\mathsf{p}}{\mathsf{p}} \frac{\mathsf{n}}{\mathsf{n}} + \frac{\mathsf{p}}{\mathsf{n}} \frac{\mathsf{n}}{\mathsf{p}} \\ \mathsf{M}_{\lambda,\mu}^{\mathsf{QUASI-}}(s,t) &= \frac{\mathsf{p}}{\mathsf{n}} \frac{\mathsf{n}}{\mathsf{n}} \frac{\mathsf{p}}{\mathsf{p}} + \frac{\mathsf{p}}{\mathsf{n}} \frac{\mathsf{n}}{\mathsf{p}} + \frac{\mathsf{p}}{\mathsf{n}} \frac{\mathsf{n}}{\mathsf{p}} \\ \mathsf{M}_{\lambda,\mu}^{\mathsf{REGGE-}}(s,t) &= \frac{\mathsf{p}}{\mathsf{n}} \frac{\mathsf{n}}{\mathsf{p}} \frac{\mathsf{p}}{\mathsf{n}} \\ \mathsf{N}_{\lambda,\mu}^{\mathsf{REGGE-}}(s,t) &= \frac{\mathsf{p}}{\mathsf{n}} \frac{\mathsf{n}}{\mathsf{p}} \\ \mathsf{n} &= \frac{\mathsf{n}}{\mathsf{n}} \frac{\mathsf{n}}{\mathsf{n}} \\ \mathsf{n} \\= \frac{\mathsf{n}}{\mathsf{n}} \\ \mathsf{n}$$

Figure 41. Helicity Amplitude Expansion in Terms of Particle Exchange.

From inspection of the expressions for do/dt and $P_0d\sigma/dt$, one can conclude: pion exchange alone can produce no polarization because it cannot contribute to ϕ_5 ; conversely the non-zero polarization data imply that natural spin-parity exchange be present -- hence large ρ , A_2 contributions (and perhaps other more low lying trajectories) are to be expected. However the pion, which is presumed to be the important factor in the forward peak of the differential cross section, 5 , 28 , 29 can influence the magnitude and sign of the polarization through its coupling strength and contribution to the overall phase of ϕ_0 . In the expression $P_0d\sigma/dt$ then, the ρ and A_2 exchanges will control the magnitude and phase of ϕ_5 , and π , ρ , and A_2 exchanges will determine ϕ_0 .

For each particle exchange there are two possible couplings, flip and nonflip, corresponding to the net nucleon helicity flip at the vertex in the Feynman diagram. Of the three particle exchanges considered, only the π -coupling is rigidly specified within the framework of these models: $g_{\text{nonflip}}^{\pi} = 0.0$, $g_{\text{flip}}^{\pi} = g_{n\pi p}$. The first is zero to satisfy parity conservation, the second is measured in pionnucleon scattering. 30

B. Models

A helicity amplitude may be written as a series of Feynman graphs (Figure 41). The simplest theoretical description is to consider only the Born term, a one particle exchange approximation. For the two amplitudes to which the

pion contributes, one gets:

$$\phi_2(t) = \phi_4(t) = g^2 \frac{|t|}{|t| + m_{\pi}^2}$$

which predicts a zero in the cross section at t=0. Since π -Reggeon exchange contains a similar functional form:

$$\phi_2(t) = \phi_4(t) = g^2 \frac{|t|}{|t| + m^2} \zeta(t) \frac{s}{s_0}$$

it too predicts a forward dip. Hence to get a useful description for $d\sigma/dt$ and P_0 one must look beyond the Born term and consider rescattering diagrams. By interference among the Regge poles and the additional contributions from rescattering, one hopes to fill in the forward dip in the differential cross section.

It should be mentioned that one must avoid a strictly dual picture for the nppn system as well, e.g., as the s-channel is exotic, the Dual Absorption Model³¹, ³² predicts the imaginary parts of all the helicity amplitudes to be zero (or very small), implying that $P_0(|t|) \sim 0$ for all |t|.

In what follows, only the Born term plus contributions from the Regge-Pomeron graphs (Figure 41) will be considered; Regge-Regge graphs will not be included. In particular, the Regge-Pomeron corrections will in general have sizeable real and imaginary parts.

After expanding a given particle exchange amplitude $m_{\lambda\mu}^{ex}$ (s,t) in partial waves, including elastic scattering with the Sopkovich prescription, 33 and rewriting the partial wave series as a Hankel transform over impact parameter b4

(see Appendix G for details), one gets:

$$m_{\lambda\mu}^{\text{TOTAL}}$$
 (s,b) = $m_{\lambda\mu}^{\text{Regge}}$ (s,b) S^{EL} (s,b)

where $S^{EL}(s,b) = 1 + \frac{i \ Pcms}{4\pi \sqrt{s}} \ m^{EL}(s,b)$, and λ , μ are the helicity flips of the external nucleons: $\lambda = \lambda_4 - \lambda_2$, $\mu = \lambda_3 - \lambda_1$. Combining expressions gives:

$$m_{\lambda\mu}^{\text{TOTAL}}(s,b) = m_{\lambda\mu}^{\text{REGGE}}(s,b) \left(1 + \frac{i \text{ Pcm s}}{4\pi \sqrt{s}} m^{\text{EL}}(s,b)\right).$$

The original Regge exchange amplitude is modulated by an elastic scattering correction term as yet to be specified. The various phenomenological models differ in their choice of parametrization of $m_{\lambda\mu}^{REGGE}$ (s,b) and m^{EL} (s,b) -- common variants are presented in Appendix G. Different combinations of these amplitudes were tried in an attempt to fit the polarization and cross section data.

1. Elastic Amplitudes:

Figure 42 shows attempted fits to the differential cross section using the various elastic amplitudes listed in Appendix G. Independent of the parametrization of the Regge amplitude, those elastic amplitudes which consider the first two rescattering graphs only in Figure 41 (weak cut), and hence do not estimate the contribution of the diffraction elastic intermediate states, cannot generate a strong forward peak. However if one includes an estimate of the remaining graphs (except Regge-Regge) which contain the diffractive intermediate states with the same internal quantum numbers as the nucleon, then one can generate a strong enough

cut. In the case of SCRAM,² the effect of the additional graphs was incorporated by taking the simple elastic absorption (G-1) and multiplying it by a coherent inelastic factor λ , where λ is greater than one and has in general different values for each particle exchange and helicity amplitude.³ The physical effect of $\lambda > 1$ is to enhance the absorption at small impact parameter, and sharpen the edge at r ~1 fm (see Figure 43). More recently, a model proposed by Hartley, Kane and Vaughn (HKV)³⁶⁻³⁸ splits the elastic scattering amplitude into two components, a central core and edge piece, with additional contribution from the diffraction elastic states included as an edge effect only. This is made explicit by two terms, P and D, in this parametrization (G-4). Each of these models (SCRAM and HKV) is capable of generating the forward peak in the cross section.

2. Regge Amplitudes:

The original motivation for the strong cut formulation was to generate dip structure in cross sections through diffractive means, rather than having to rely on nonsense-sense-signature-zeros of Regge amplitudes. Hence one should not use an NWSZ Regge amplitude with the strong cut formalism. (Attempts at trying to use both have resulted in the wrong sign and incorrect |t| behavior of the polarization parameter. The appropriate Regge pole forms are either G-6 or G-8 which have no NWSZ features. As shown in Figures 3 and 43, this model will fit both $d\sigma/dt$ and P_0 for |t| values less than 0.4, but fails for larger |t| primarily because of the

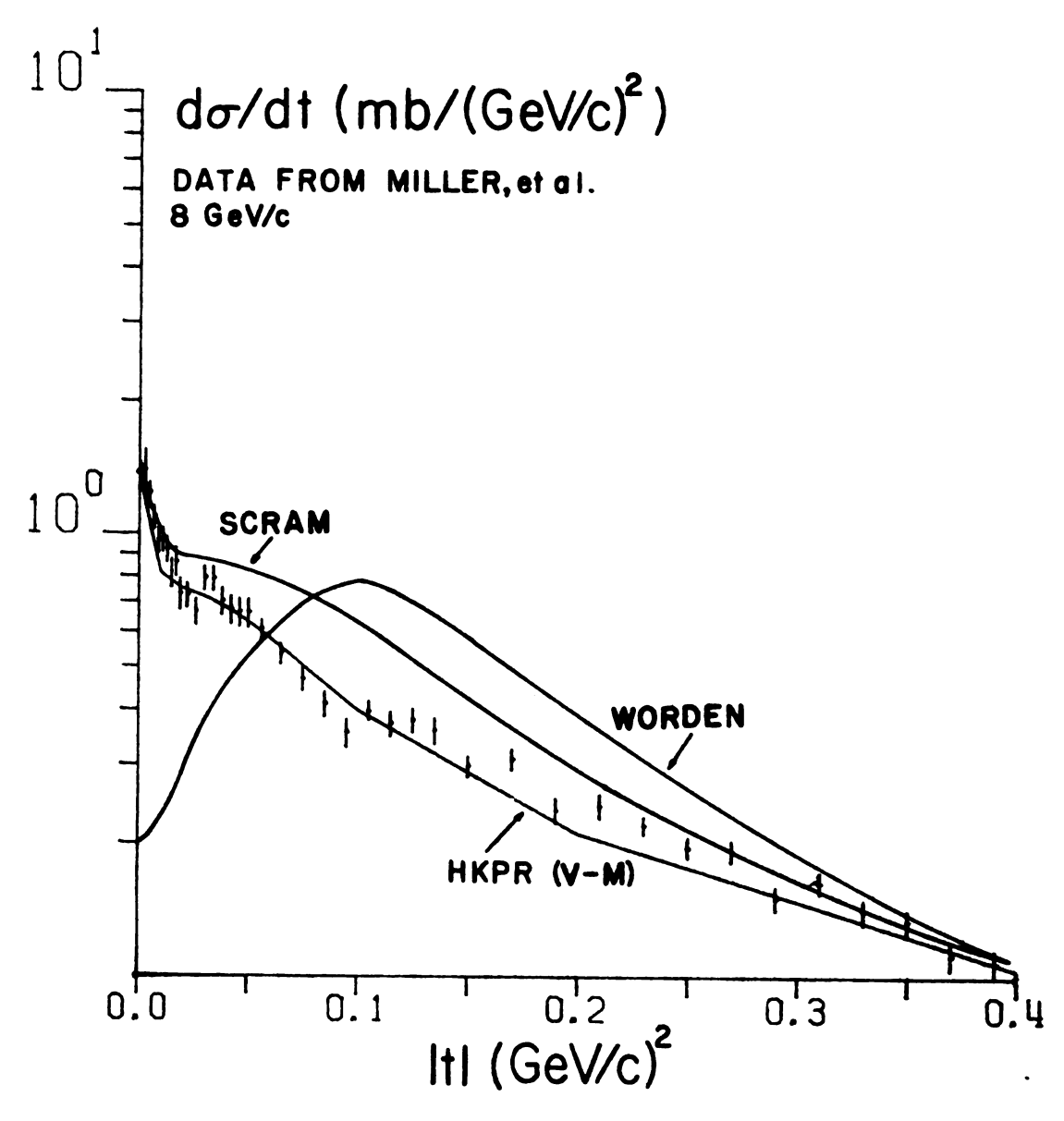


Figure 42. Fits to do/dt with Various Choices of meff(s,t).

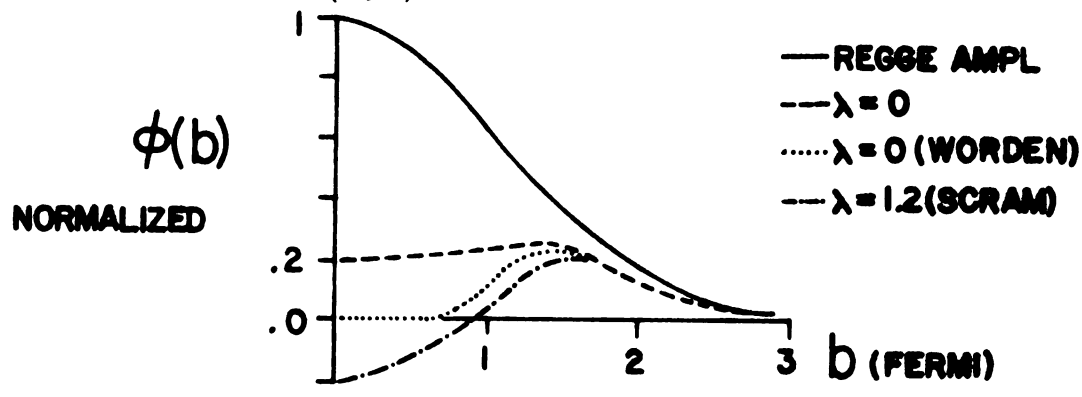


Figure 43. How Absorption Modifies a Helicity Amplitude.

large uncompensated pion cut. In addition the polarization is low for |t| > 0.4 where the differential cross section is too high.

The expression for the polarization parameter:

$$P_0 \frac{d\sigma}{dt} = 2 \operatorname{Im} \phi_5 * \phi_0 / (128\pi P_{\text{cms}}^2 \text{ s})$$

suggests several possibilities: First, the overly large values for $d\sigma/dt$ as determined from the fit for $|t|^2$ 0.4 may render P_0 small; second, ϕ_5 may become inherently small at large |t|; and third, the vectors ϕ_5^* and ϕ_0 may become relatively colinear as $|t| \to 1.0$.

A study of the first possibility requires forcing $d\sigma/dt$ to the correct slope and size. To do this the vertex-modified (V-M) form for the Regge amplitude (G-7) was employed which makes additional assumptions about the exchange amplitude coupling constants. They were treated as exponentially damped with |t|, the |t| dependence being different for a vertex with nucleon helicity flip or non-flip:

$$\tilde{g}_{v} = g_{v} \exp (\epsilon_{v}(t-m_{j}^{2}))$$

$$\tilde{g}_{T} = g_{T} \exp (\epsilon_{T}(t-m_{j}^{2}))$$

where g_V , g_T are the magnitudes of the vector, tensor (non-flip, flip) couplings, m_j is the exchange particle mass, and ε_V , ε_T depend only on helicity flip and not particle exchange. Such a choice preserves the form of the original amplitude near the particle pole and could possibly allow ρ and A_2 coupling constants to be more nearly equal. The technique

produces good fits to the differential cross section for \vec{nppn} over the range $0.0 \le |t| \le 1.0 (\text{GeV/c})^2$ and $3.0 \le P_{\text{LAB}} \le 24.0 \text{ GeV/c}$, but does not reproduce the differential cross section for $\vec{pp} + \vec{nn}^{40}$, where $\vec{pp} + \vec{n}^{40}$ very well (Figures 44 and 46). What the fits predict $P_0(\vec{np+pn})$ and $P_0(\vec{pp+nn})$ to be are shown in Figures 45 and 47.

However the relative phase between ϕ_5^* and ϕ_0 is considerably altered from the SCRAM case, and P_0 is much too small for $|t| \stackrel{>}{=} 0.2$ (see Figure 45). Hence the magnitude of ϕ_5 and the relative phase between ϕ_5^* and ϕ_0 are the key quantities — their dependence as functions of (t) are shown in Figures 48 and 49 for SCRAM and V-M models. The results show a relative colinearity of the phasers in the range $0.6 \stackrel{<}{=} |t| \stackrel{<}{=} 0.8$, and compounded with the relatively small size of $|\phi_5|$ at large |t|, P_0 is forced to die away for $|t| \stackrel{>}{=} 0.6 (\text{GeV/c})^2$.

The remaining options are: to revise the size of the A₂ contribution (the least peripheral exchange) and to introduce an appropriate t-dependent real part into the elastic scattering which will allow more flexibility in the phase determination of ϕ_5 and ϕ_0 , in an attempt to boost the large |t| values of P₀. One method devised with these ideas in mind is the previously mentioned HKV approach using G-4 and G-8 as the elastic and Regge amplitudes. In this model, the elastic scattering form (G-4) has been constructed to reproduce the high energy CERN ISR proton-proton elastic

scattering data, ⁴² and appears to be able to generate the differential cross section for $0.0 \le |t| \le 1.0 (\text{GeV/c})^2$ and sizeable polarization magnitudes for larger $|t| (\ge 0.6)$.

Typical fits for do/dt and $P_0(t)$ are shown in Figures 50-53.

A summary of the "merits" of the various phenomenological models is presented in Table 3; none except the HKV scheme appears to satisfactorily fit both the polarization and differential cross section. The form of the HKV Pomeron however, reveals that a detailed phenomenological description of the polarization in nucleon-nucleon scattering is complicated when treated as a strong cut Reggeized problem. Though one may obtain a fit to the data which is much improved over previous cut models, it is not clear one has gained insight into the mechanism(s) responsible for the polarization seen.

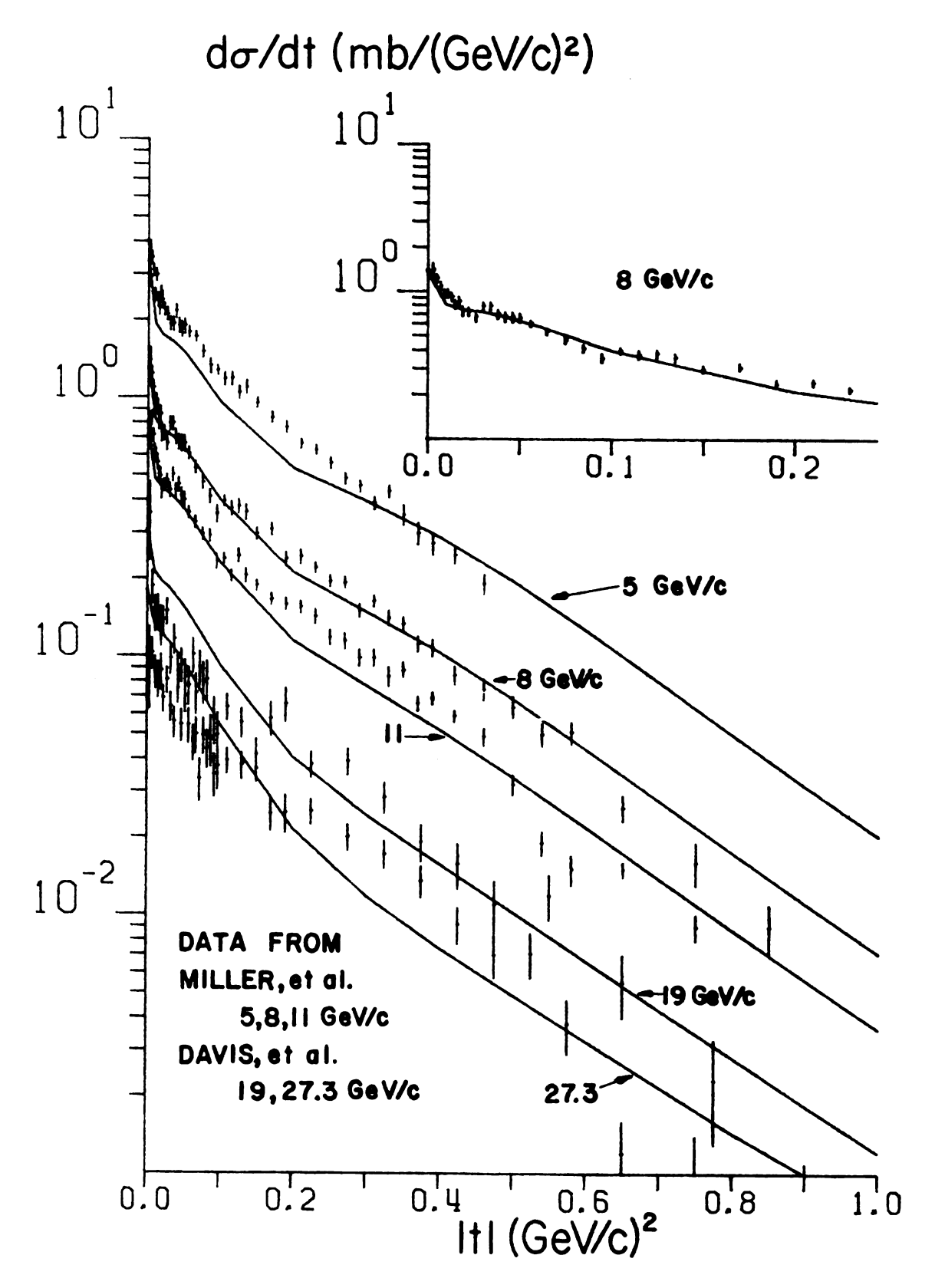


Figure 44. V-M Fits to $d\sigma/dt$ (n+p \rightarrow p+n).

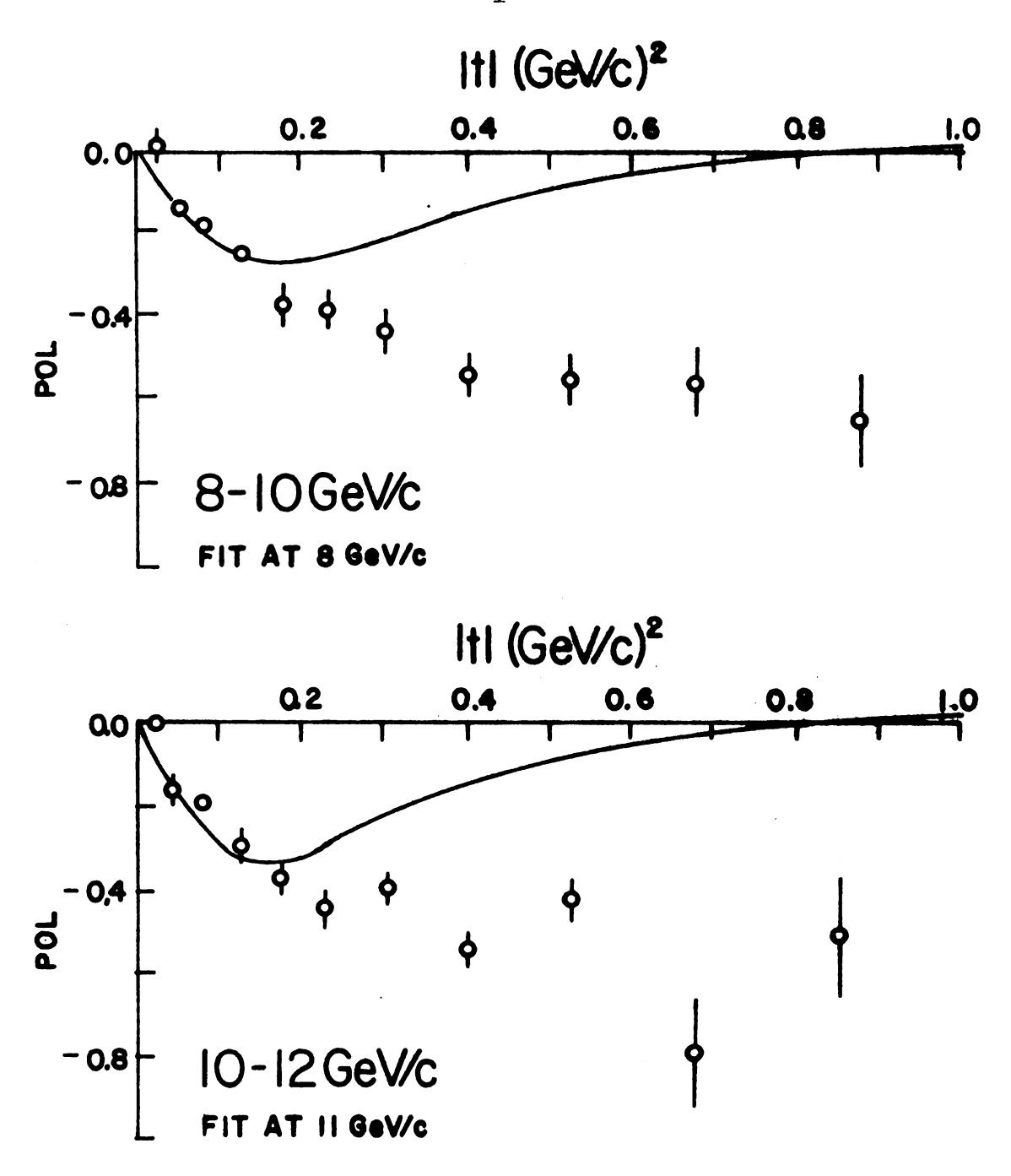


Figure 45. V-M Fits to $P_0(n+p \rightarrow p+n)$.

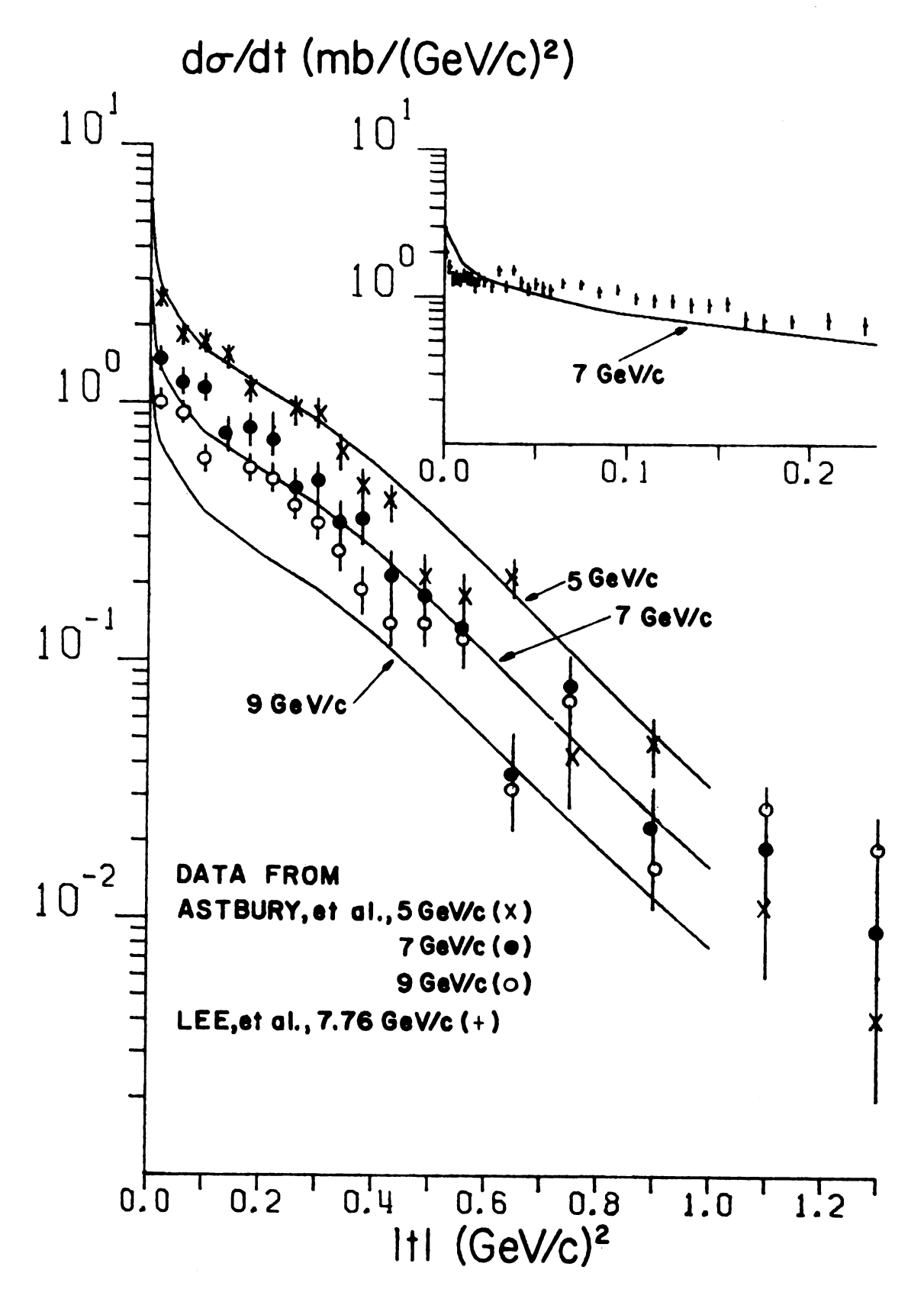


Figure 46. V-M Fits to do/dt ($\bar{p}+p \rightarrow \bar{n}+n$).

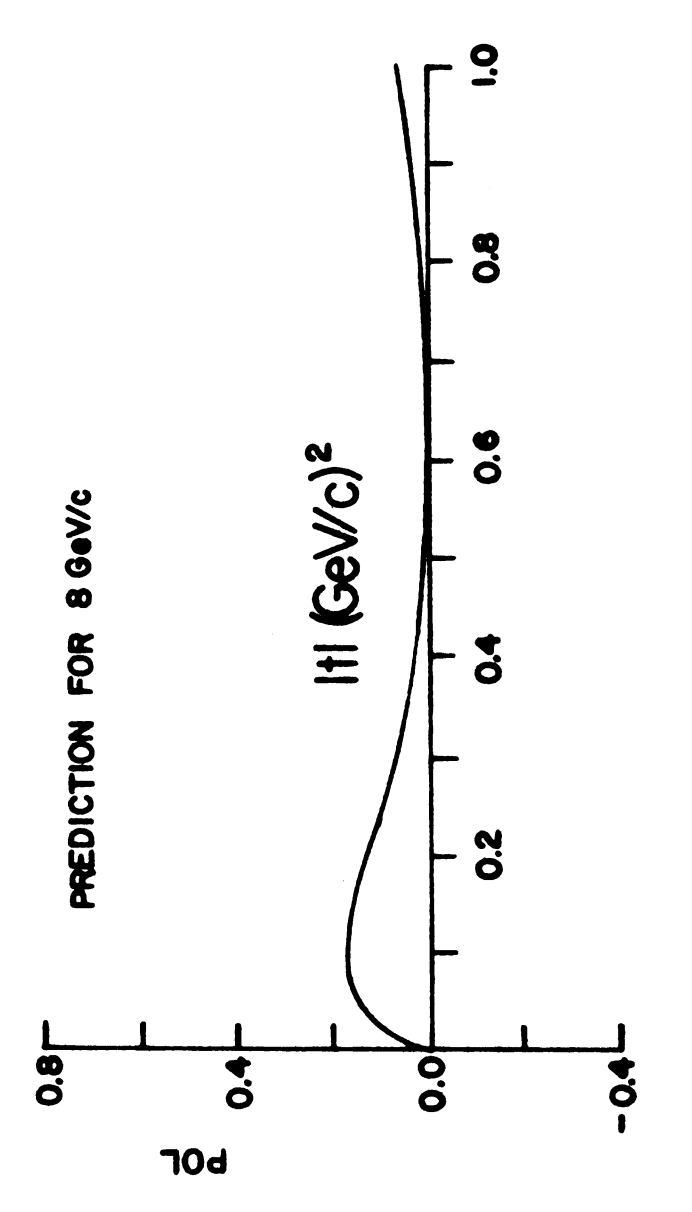


Figure 47. V-M Prediction for $P_0(\bar{p}+p + \bar{n}+n)$.

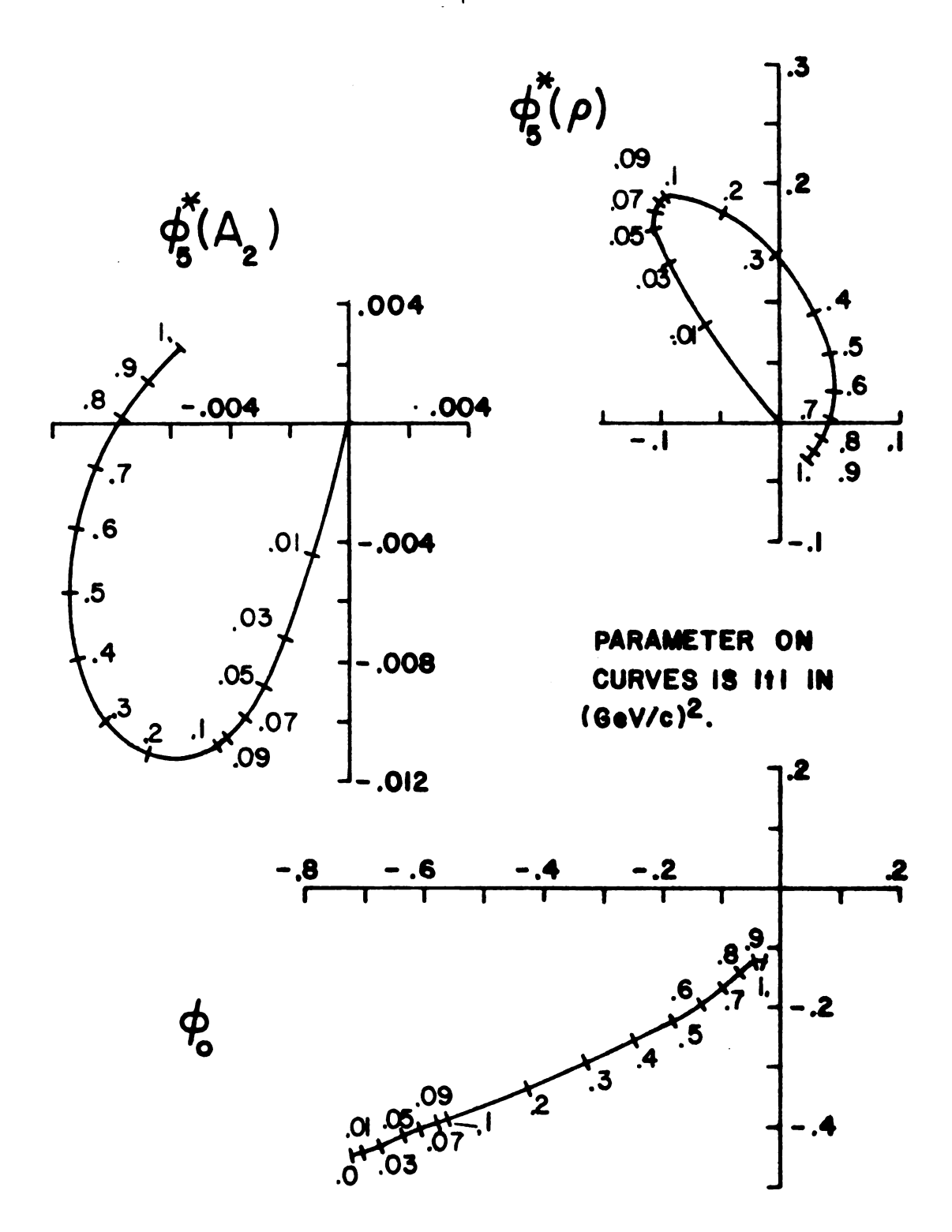


Figure 48. Argand Plots of ϕ_5^* and ϕ_0 for the SCRAM Model.

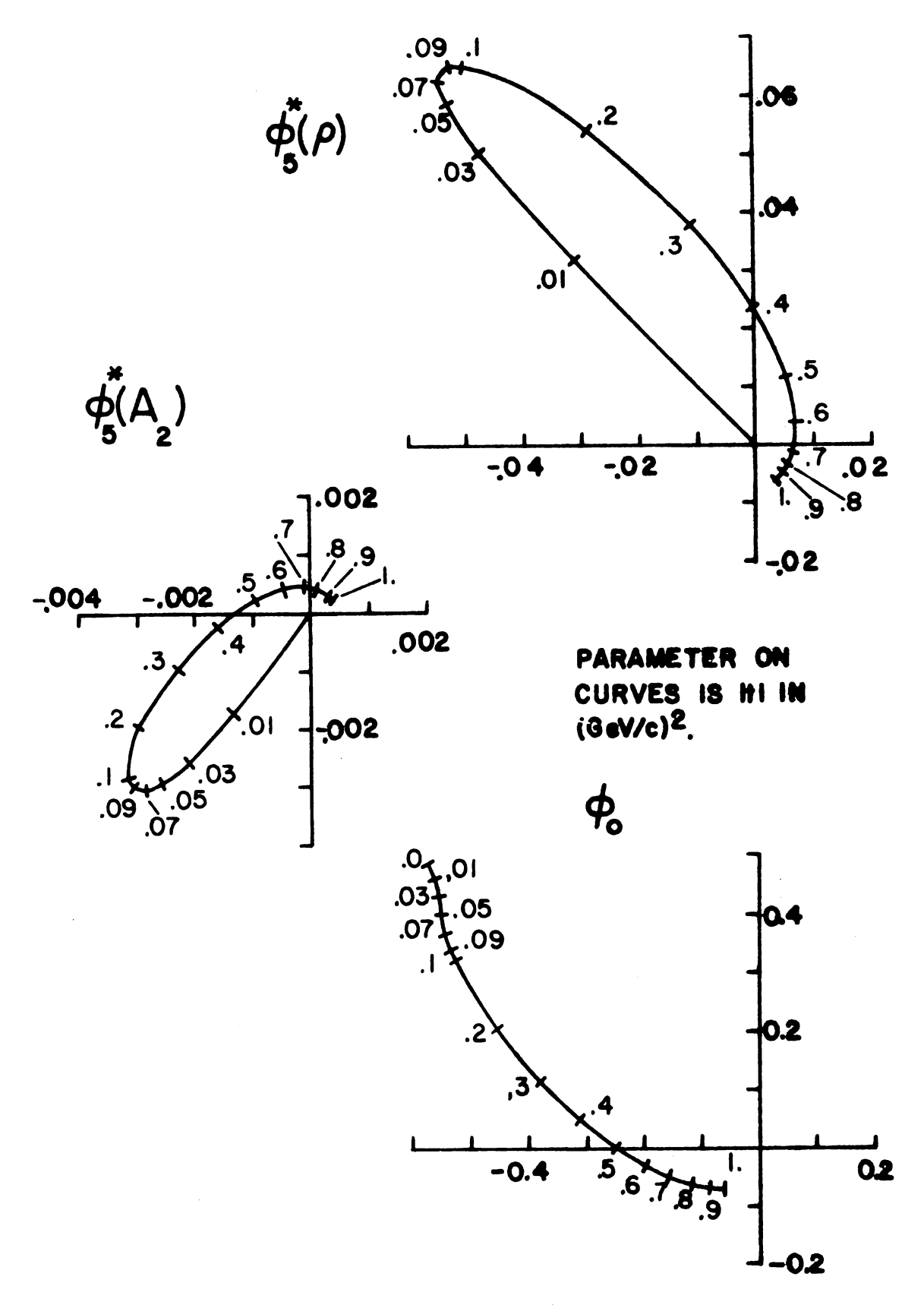


Figure 49. Argand Plots of ϕ_5^* and ϕ_0 for the V-M Model.

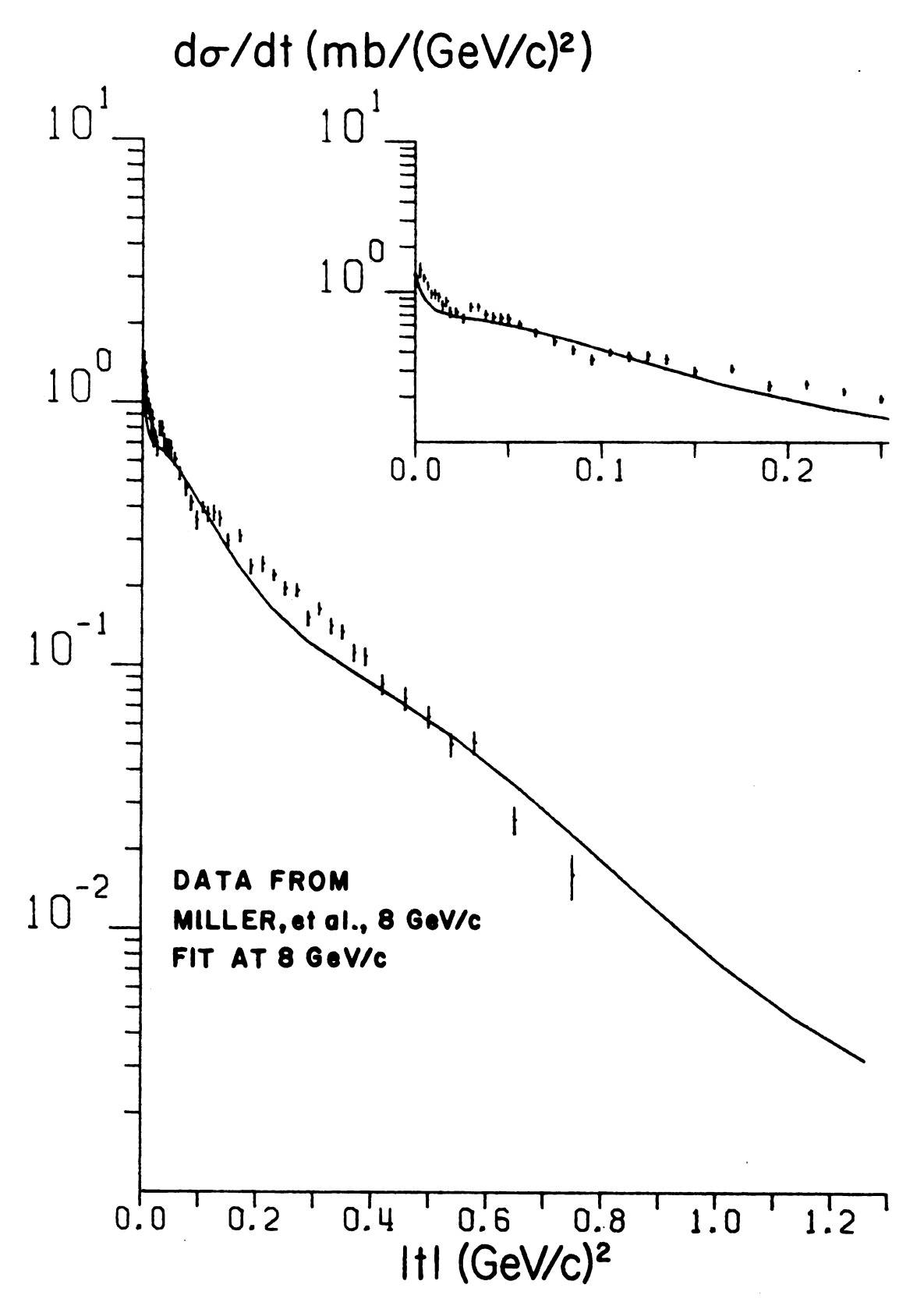


Figure 50. HKV Fit to $d\sigma/dt$ (n+p + p+n).

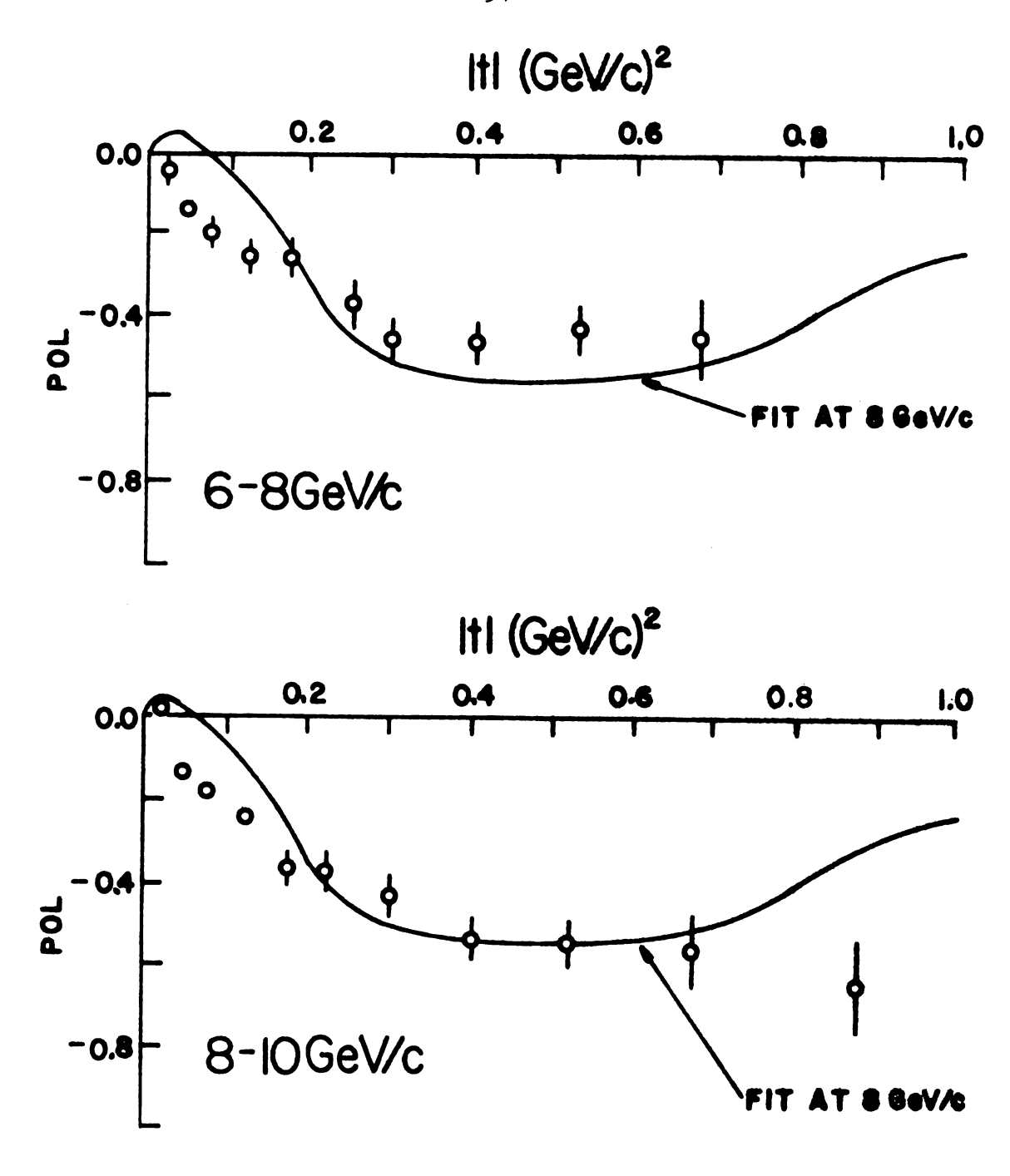


Figure 51. HKV Fit to $P_0(n+p \rightarrow p+n)$.

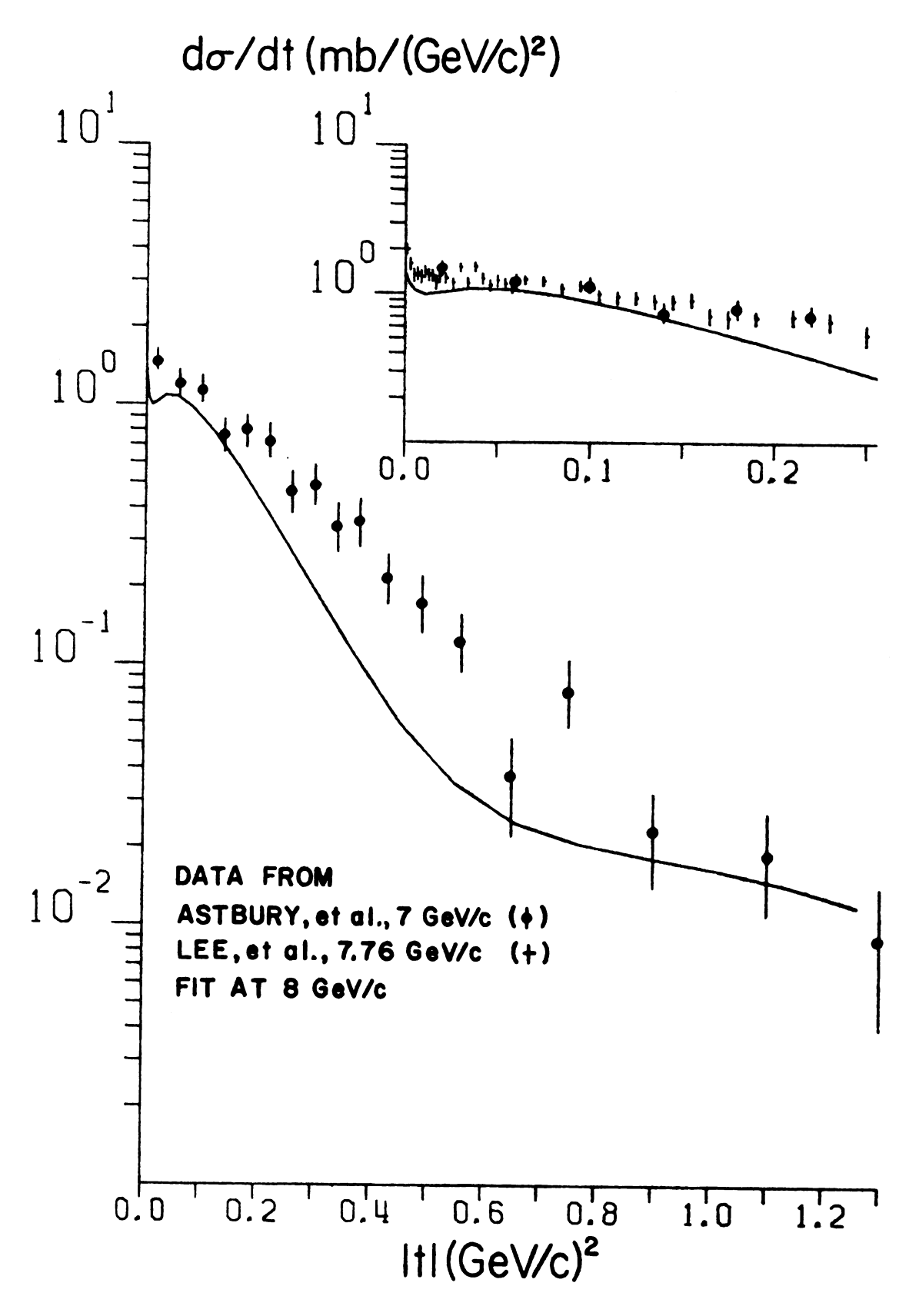


Figure 52. HKV Fit to $d\sigma/dt$ ($\bar{p}+p + \bar{n}+n$).

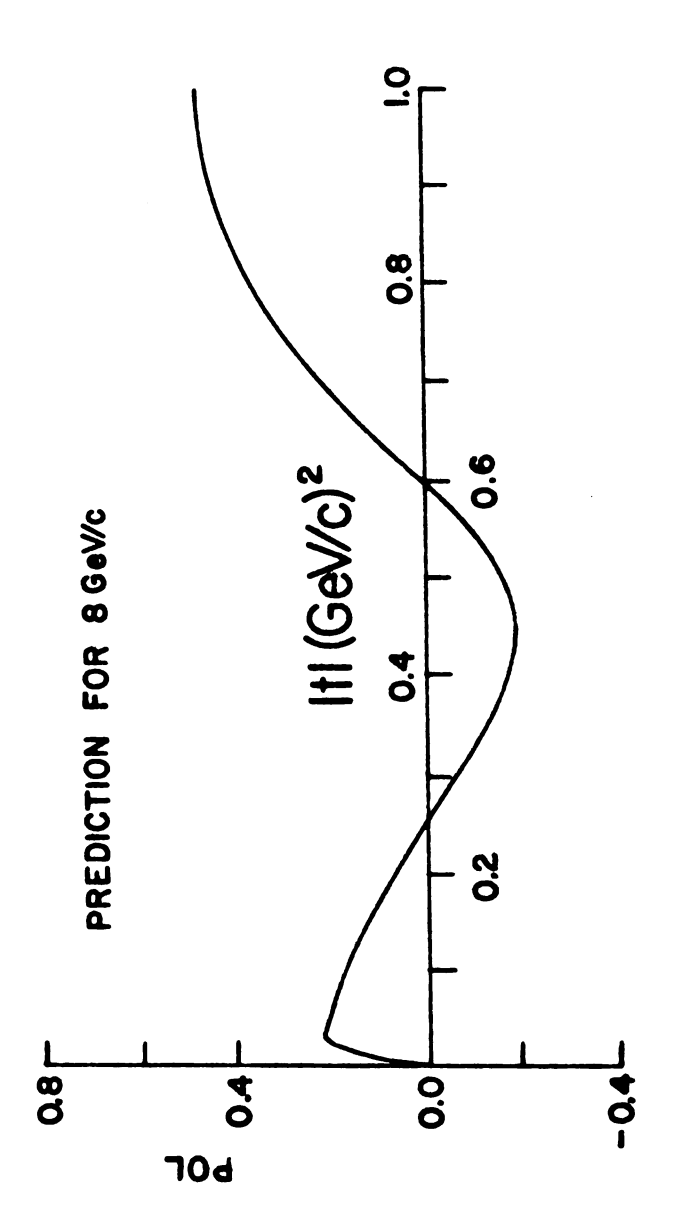


Figure 53. HKV Prediction to $P_0(\bar{p}+p + \bar{n}+n)$

Table 3. Table of Results of Phenomenological Models

Weak Cut Models:

do/dt: No forward peak of sufficient strength. Wide |t| (2 O.1(GeV/c) 2) Respectable.

POL: Can fit polarization with assumptions of additional exchanges such as AD HOC X-Meson.

Strong Cut Models:

SCRAM:

do/dt: Can fit small |t| ($\leq 0.4(\text{GeV/c})^2$) behavior; fails for larger |t| due to large pion cut. Correctly predicts energy dependence.

POL: Can fit small |t| ($\le 0.4(\text{GeV/c})^2$) behavior; fails for larger |t| with polarization too small.

V-M:

do/dt: Can fit behavior for $0.0 \le |t| \le 1.0 (\text{GeV/c})^2$; however forward peak predicted for $\bar{p}p\bar{n}n$ is too strong. Energy dependence is OK.

POL: Fit to polarization is useless for |t |

2 0.25(GeV/c)².

HKV:

do/dt: Good fits to 8 GeV/c for $0.0 \le |t| \le 1.0 (\text{GeV/c})^2$ for both nppn and $\bar{p}p\bar{n}n$.

POL: Fit to polarization is respectable with possible problems for $0 \le |t| \le 0.15 (\text{GeV/c})^2$ and $|t| \ge 0.8 (\text{GeV/c})^2$.

Comment: This model is superior to the other cut models tried.

CHAPTER VI

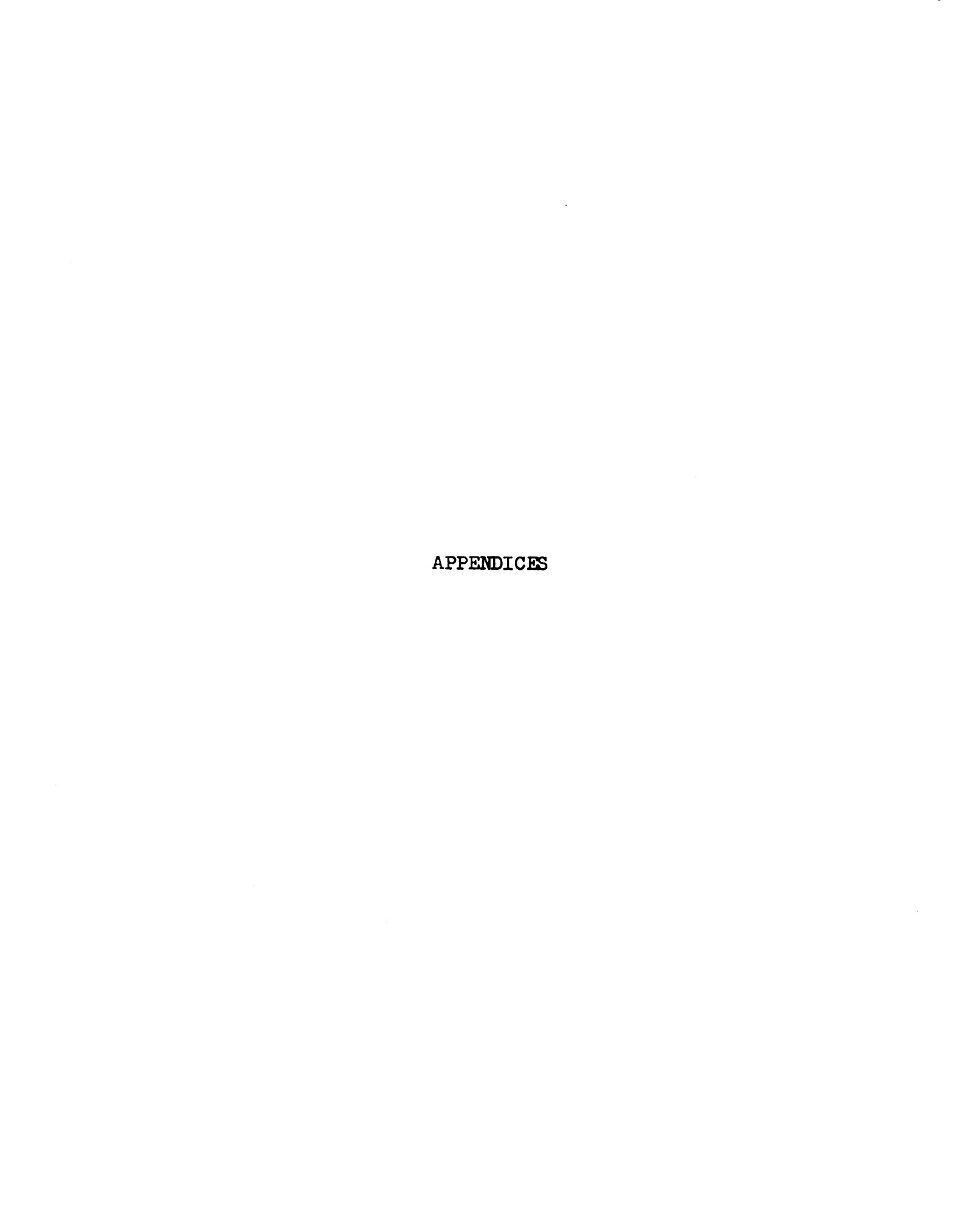
CONCLUSIONS OF THE EXPERIMENT

A. Experimental Implication

The polarization for the reaction n+p + p+n is roughly energy independent with a tendency toward slightly higher polarization values as incident momentum is increased over the measured range 2-12 GeV/c. The trend suggests that the polarization will be large at higher energies.

B. Theoretical Implication

The data imply important natural spin-parity contributions for the generation of polarization. It is also clear from the differential cross section measurements that an exchanged Reggeon must be accompanied by a complex elastic rescattering correction to obtain an adequate fit to the data for $0.0 \le |t| \le 1.0 (\text{GeV/c})^2$. Current strong cut parametrizations of the rescattering can yield fits to the neutron-proton charge exchange data; however in their present form they do not necessarily lead to an understanding of the underlying mechanisms of polarization observed in this reaction.



APPENDIX A

KINEMATICS FOR THE n+p + p+n SYSTEM

The kinematics for the reaction n+p + p+n may be specified by the Mandelstam variables:

$$s = (P_1 + P_2)^2$$

 $t = (P_1 - P_3)^2 = (P_2 - P_4)^2$
 $u = (P_1 - P_1)^2$

where the four momenta are defined in Figure Al. Specializing to the laboratory (Figure A₂), and using the equal mass approximation $m_p \approx m_n = m$ we can obtain:

$$s = 2m(m+E_1)$$

 $t=-2mT_{\downarrow\downarrow}$ where $T_{\downarrow\downarrow}$ is the kinetic energy of the outgoing neutron. Another useful quantity is the approximation:

t $\approx -p^2\theta_3^2$ for θ_3^2 small and $|\vec{P}_1| > m$, $|\vec{P}_3| > m_3$ and $|\vec{P}_1| - |\vec{P}_3| = P$, and where θ is the usual polar angle, measured relative to the direction \vec{P}_1 .

In this experiment all four momenta were known except for the incident beam $P_1 = (E_1, P_1)$. The three momentum of each particle in the reaction was described during various analyses by several different sets of variables. These choices are shown in Figure A3 for regular polar coordinates, online coordinates, and fitting program coordinates. Regular

cartesian reference axes are shown in each diagram, with \hat{z} the direction of the beam line, \hat{y} the vertical direction above the experimental floor and the direction of positive target polarization, and \hat{x} directed toward the neutron spectrometer.

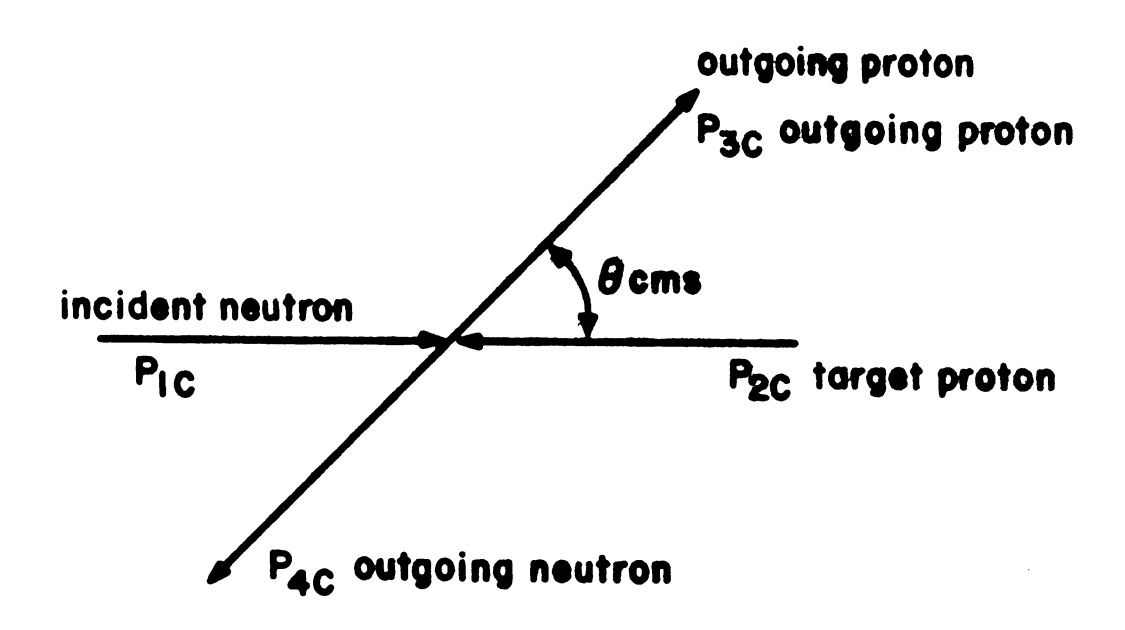


Figure A-1. Scattering in the Center of Momentum Frame.

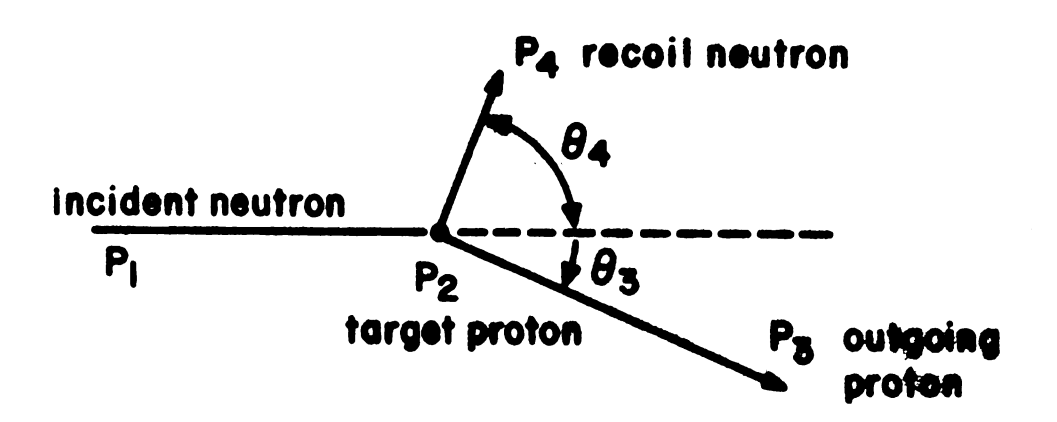


Figure A-2. Scattering in the Laboratory Frame.

Figure A-3. Coordinate Systems Used to Describe Particle Momenta: (a) Spherical Coordinates, (b) Online Constraint Variables, (c) Off-line Variables. The Reference Axes are: x̂, Toward Neutron Arm; ŷ, the PPT Magnetic Field Axis, ẑ, the Surveyed Beam Direction.

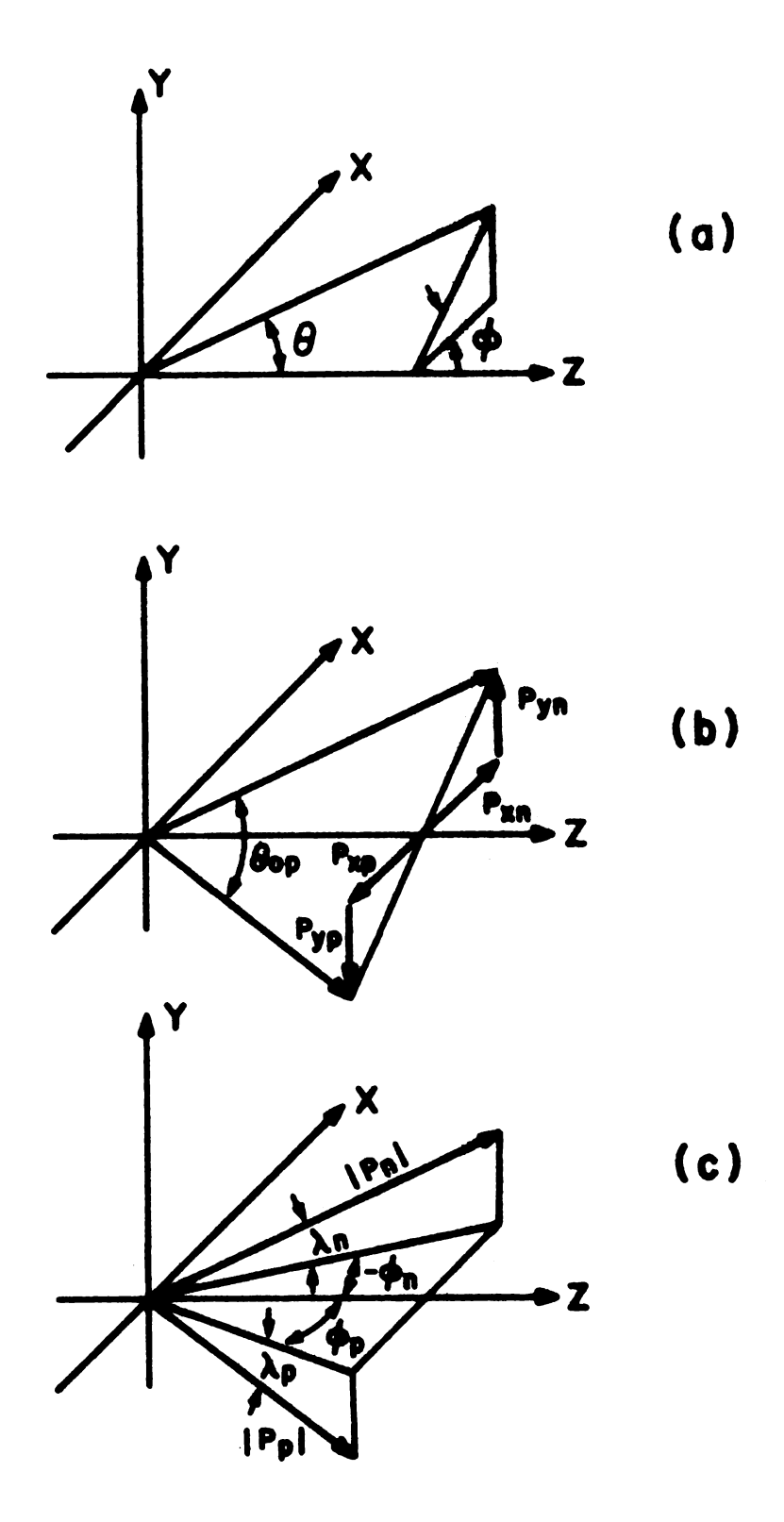


Figure A-3

APPENDIX B

NMR POLARIZATION CALCULATION

The enhanced target polarization is given as a frequency average over the imaginary part of the complex susceptibility, determined from the NMR measurement:

$$T = \xi \int_{0}^{\infty} \chi'' d\omega$$

where ξ is a proportionality constant determined from the thermal equilibrium target polarization and x = x' - jx'' is the target susceptibility. The NMR system used was a parallel circuit, constant current Q-meter. Hence one may write the circuit impedance as:

$$\frac{1}{Z} = \frac{1}{R + j\omega L_0(1 + 4\pi n\chi)} + j\omega C$$

where η is the filling factor, ω is the circuit frequency. ¹⁷ Using the assumption that x' is very small and using the usual definition $Q = \omega L_0/R$, one obtains

$$\frac{1}{Z} \sim \frac{1}{R} \frac{1}{1 + 4\pi Q \chi'' + jQ} + \frac{j}{RQ}$$

which after inversion becomes

$$Z = \frac{RQ(Q - j(1 + 4\pi Qx''))}{(1 + 4\pi Qx'')}$$

In the absence of microwaves, and with the NMR far from proton resonance, χ ' \approx χ " \approx 0 and:

$$Z_{Q} = RQ(Q - j)$$

and hence

$$\frac{Z}{Z_{O}} = \frac{\left(Q - j\left(1 + 4\pi Q X''\right)\right)}{\left(Q - j\right)\left(1 + 4\pi Q X''\right)}$$

Since we have a constant current Q-meter: $|V/V_0| = |Z/Z_0|$. Thus

$$\left|\frac{V}{V_0}\right|^2 = \frac{Q^2 + (1 + 4\pi Qx'')^2}{(1 + Q^2)(1 + 4\pi Qx'')^2}$$

which may be immediately solved for x'' (let $V/V_0 = |V/V_0|$)

$$4\pi Q X'' = \frac{V_0}{V} \left(\frac{(1 + Q^2)}{Q^2} - \frac{1}{Q^2} \left(\frac{V}{V_0} \right)^2 \right)^{-1/2} - 1$$

Assuming Q is very high and hence

$$\frac{1}{Q^2} \left(\frac{V}{V_0} \right)^2 \ll 1$$

one immediately obtains

$$X'' = -\frac{1}{4\pi Q} \left(\frac{V - V_O}{V} \right)$$

hence
$$T = \frac{-\xi}{4\pi Q} \int \frac{V - V_O}{V} d\omega = \kappa \int \frac{V - V_O}{V} d\omega$$

where $\kappa = -\xi/4\pi Q$. A similar expression will hold for the target polarization at thermal equilibrium P_{TE} :

$$P_{TE} = \kappa \int \frac{V_{TE} - V_{O}}{V_{TE}} d\omega$$

However we can now determine κ since we know P_{TE} from the Boltzmann distribution. 16

$$P_{TE} = \frac{\exp(+g\beta H/2kT) - \exp(-g\beta H/2kT)}{\exp(+g\beta H/2kT) + \exp(-g\beta H/2kT)}$$
$$= \tanh(g\beta H/2kT)$$

where g is the nuclear g factor, β is the nuclear magneton, H is the external magnetic field (25 kG), k is the Boltzmann factor, and T is the target temperature (~1.1°K).

Hence κ is determined and the enhanced polarization is obtained:

$$T = \frac{\tanh (+g\beta H/2kT)}{\int \frac{V-V_0}{V} d\omega} \cdot \frac{V_0}{V_{TE}} d\omega$$

APPENDIX C

WIRE CHAMBER SPECIFICATION

The wire spark chambers described here were built for use on a previous experiment.^{5, 8} Each chamber consisted of a 3/8 in. GlO frame upon which were stretched two orthogonal planes of aluminum wires, 24 per inch, with wire diameter depending on the module: .007 in. for the two modules upstream of the bending magnet and .010 in. for those downstream. To improve the characteristics of the large chambers, a 1 mil thick aluminum foil sheet was stretched behind each wire plane with an insulation layer of 2 mil mylar in between. The chamber volumes were maintained in a recirculated atmosphere of 90% Ne-10% He Gas.

The chambers were operated at 5.1-5.4 kV high voltage which was held on storage capacitors until the fast logic event trigger enabled a Marx generator to turn on a thyratron tube, firing the chambers. A d.c. clearing field of 35 V was applied to the chambers at all times except when the thyratron was turned on. After each spark chamber trigger, a 600 V, 4-5 msec post-clearing field was utilized to sweep the chamber volume of ionization products.

The spark chambers were equipped with magnetostrictive readout, and fiducial and spark information were digitized by a SAC 20 MHz quadscaler system. There were four scalers per plane in the upstream chambers, two per plane downstream.

Dimension and mass specifications for each chamber module are shown in Table C-1.

Table C-1. Table of Dimensions

Module number	Chamber active area	Wire diameter	Effective mass/cm ²
1	14" x 12"	.007"	.017 gm/cm ²
2	14" x 12"	.007"	.017 gm/cm ²
3	39" x 13"	.010"	.039 gm/cm ²
4	50" x 24"	.010"	.039 gm/cm ²

Resolution for the proton arm is shown in Figure C-1.

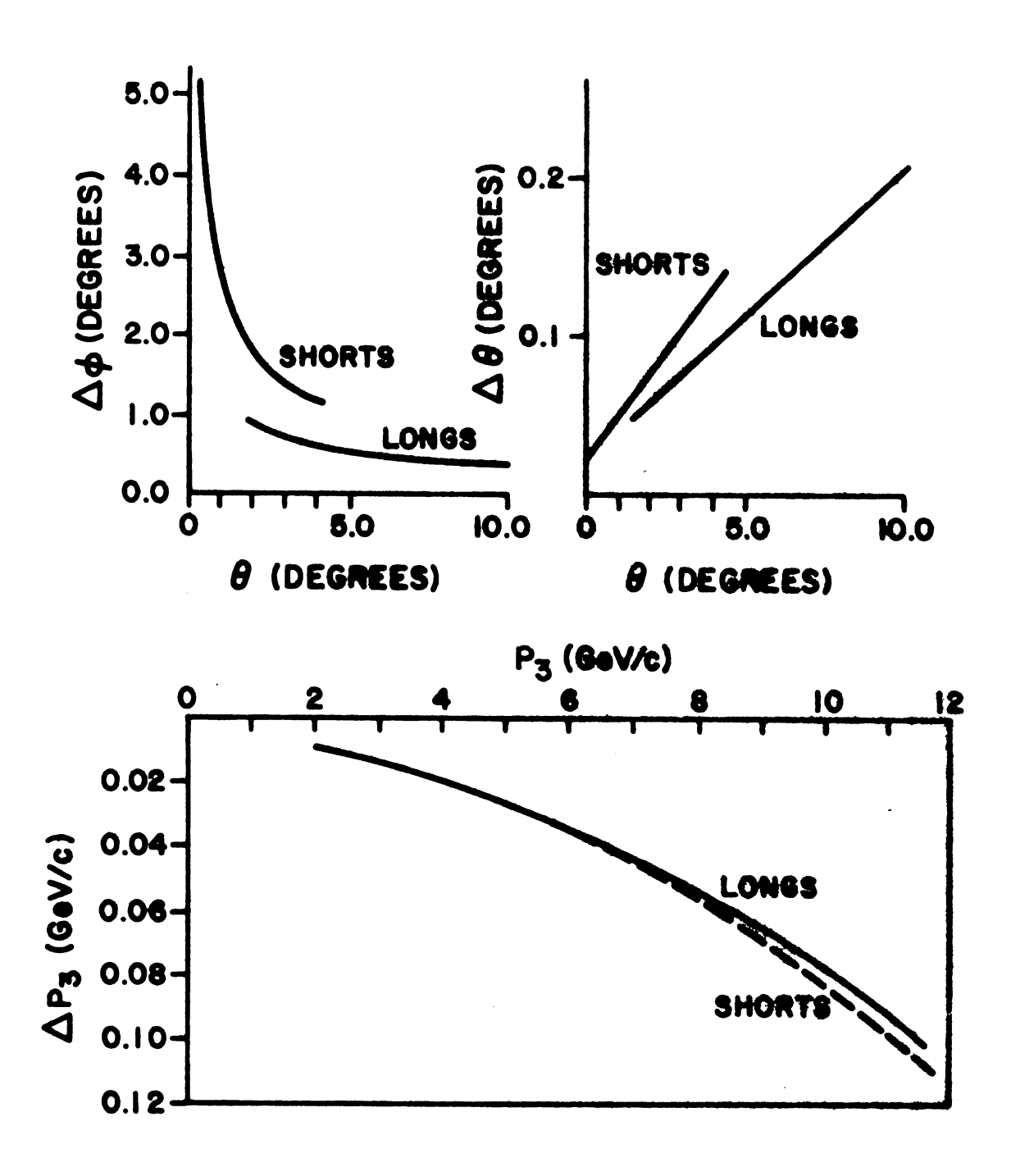


Figure C-1. Proton Arm Resolution.

APPENDIX D

NEUTRON COUNTER SPECIFICATION

Each neutron counter consisted of three active elements (see Figure D-5): a large block of Pilot Y Scintillator either 6" x 6" or 6" x 10" in cross sectional area and two 5 in. diameter Amperex 58 DVP photomultiplier tubes. To optimize the light collection at the photocathode of each tube, UVT Lucite blocks with Winston funnel light guides were used to match scintillator area to phototube area.

The negative high voltage supplied to the base of each phototube varied from counter to counter depending on tube quality, individual counter light transmission properties, and pulse height requirements which were different for the long and short counter banks. The gains of the tubes for a given array were set as nearly equal as possible; typical voltages were 1.75-2.0 kV (longs) and 2.0-2.35 kV (shorts).

From each tube base, anode and second dynode signals were extracted. The anode signal was used for timing and was used in the pulse height analysis if the signal was unsaturated. However if it was saturated, the dynode signal provided the measure of energy deposit in the counter.

Detection efficiencies for the neutron counters were calculated for given counter geometry, neutron energy, and counter discriminator threshold from a monte carlo program developed for a previous experiment (see Figure D-3). 43

Thresholds for the longs and shorts were 2.0 and 0.2 MeV respectively. Resolution for the neutron arm is shown in Figure D-4.

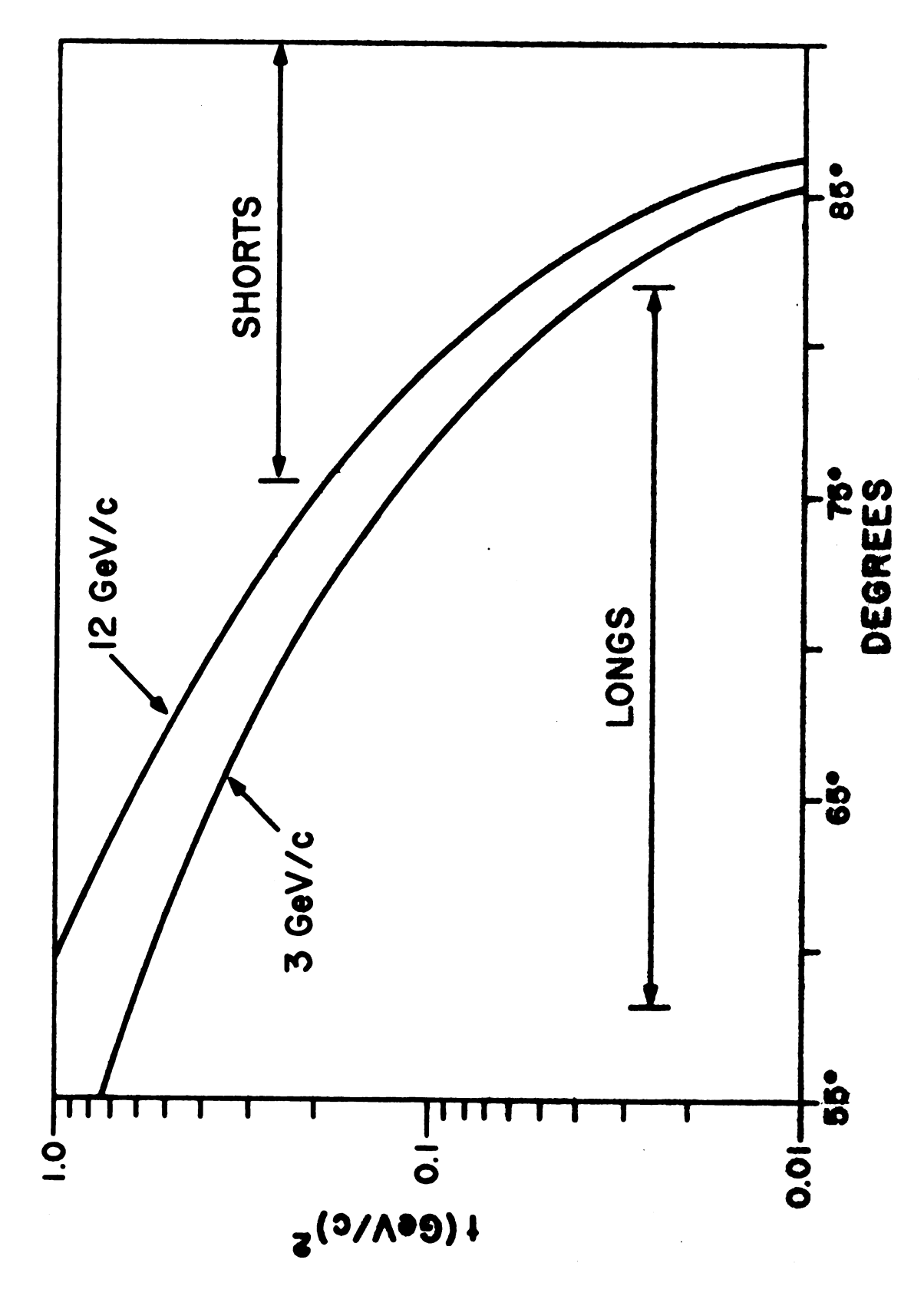
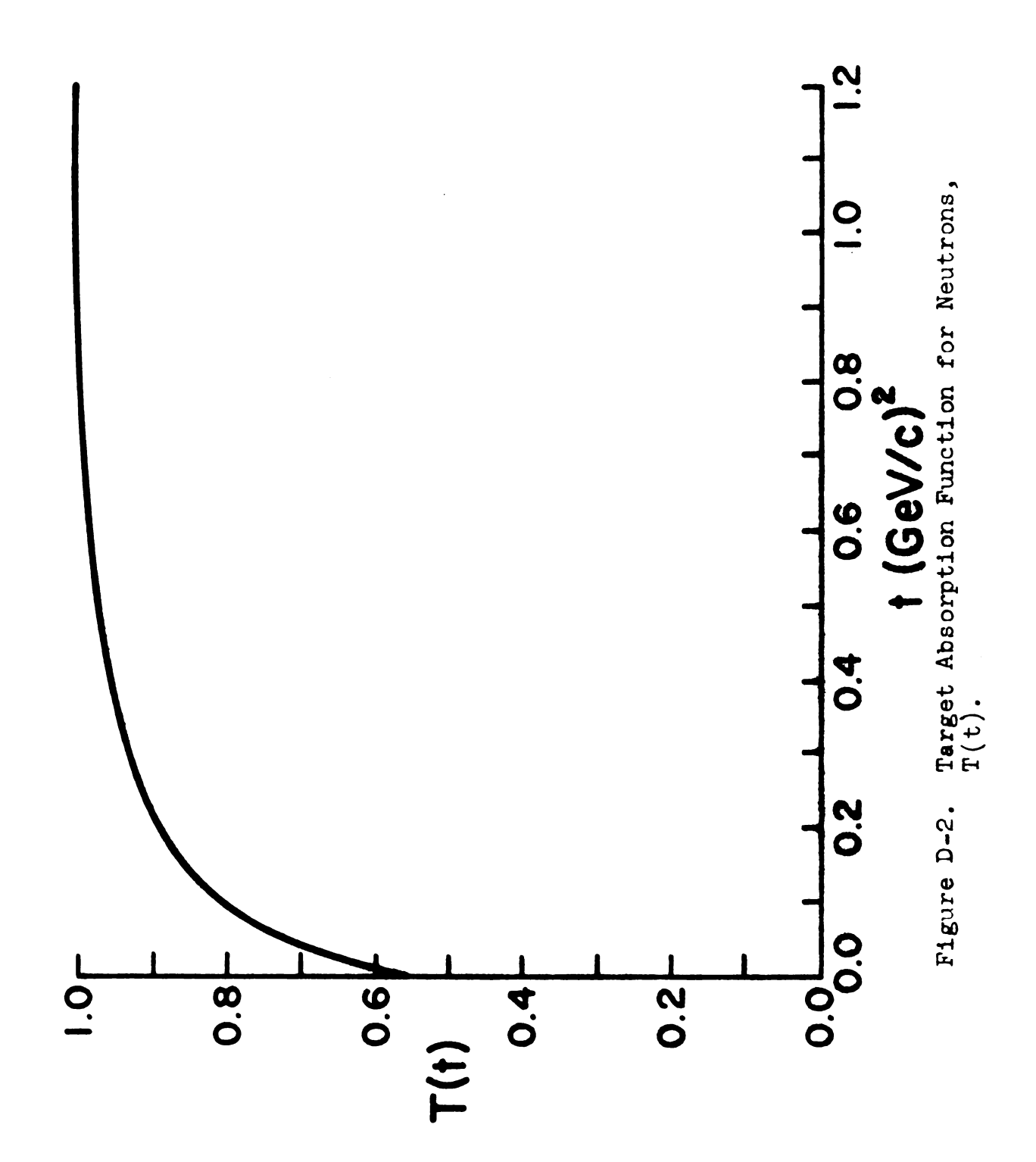
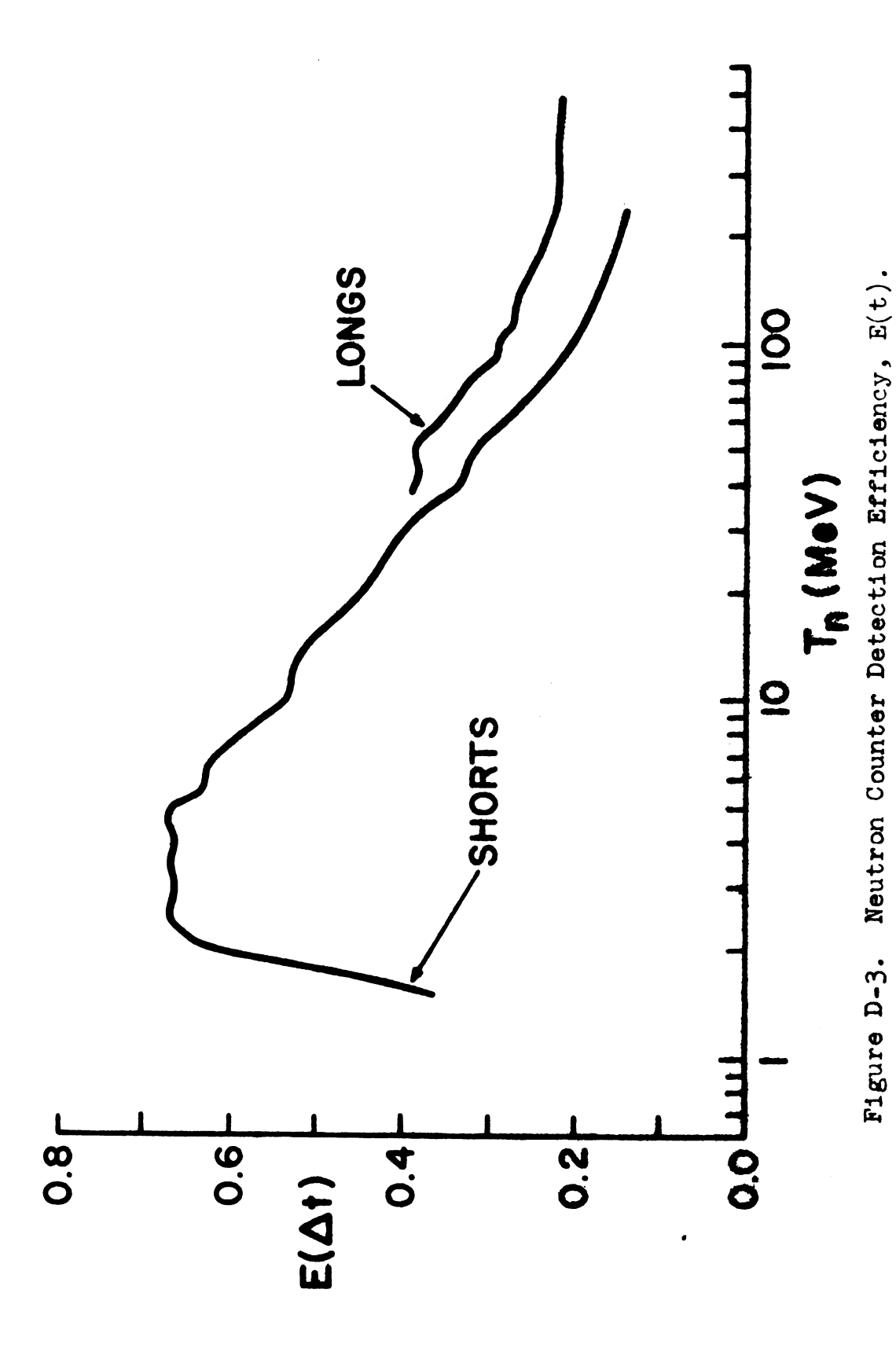


Figure D-1. Neutron Counter Acceptance, A(PLAB,t).





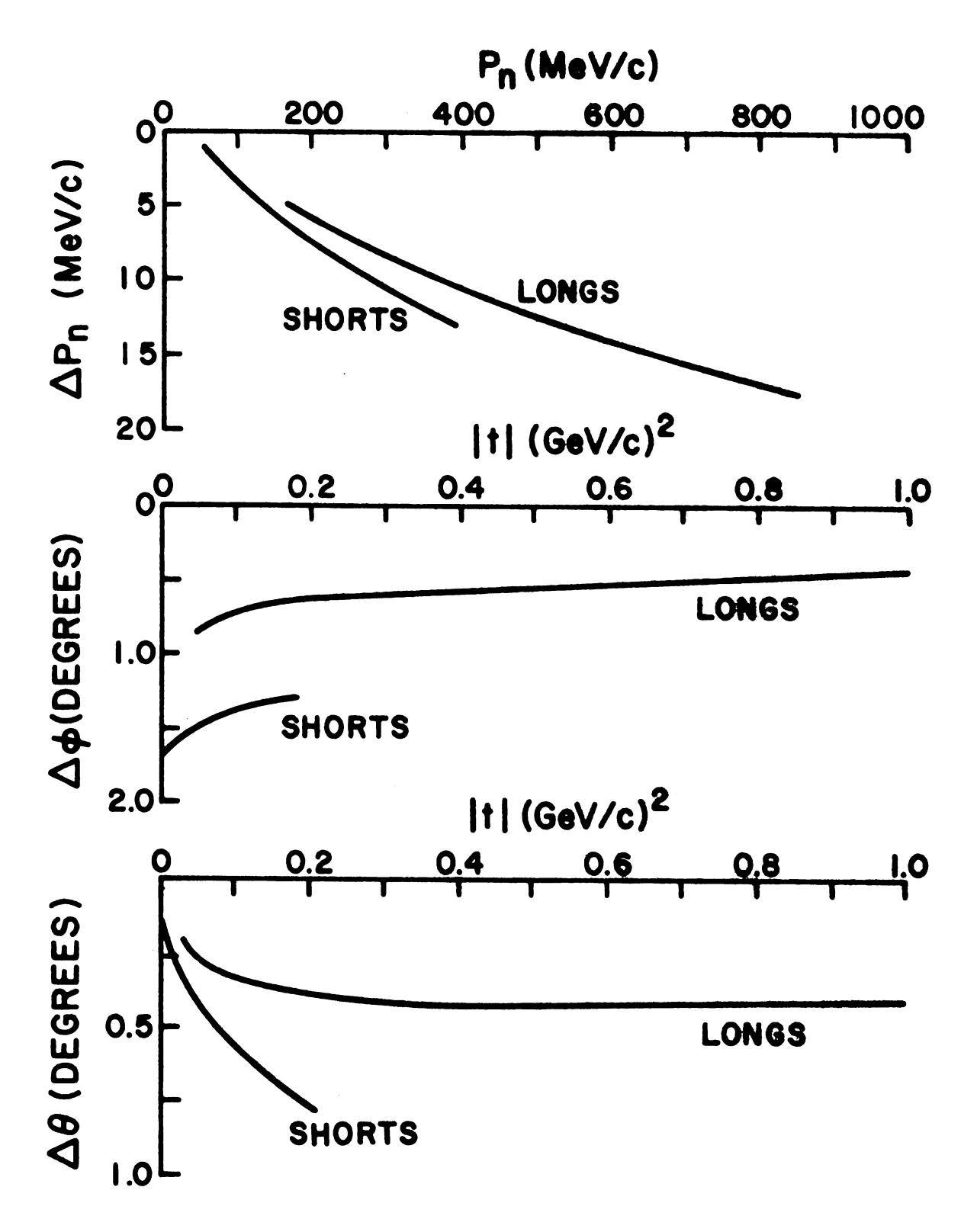


Figure D-4. Neutron Arm Resolution.

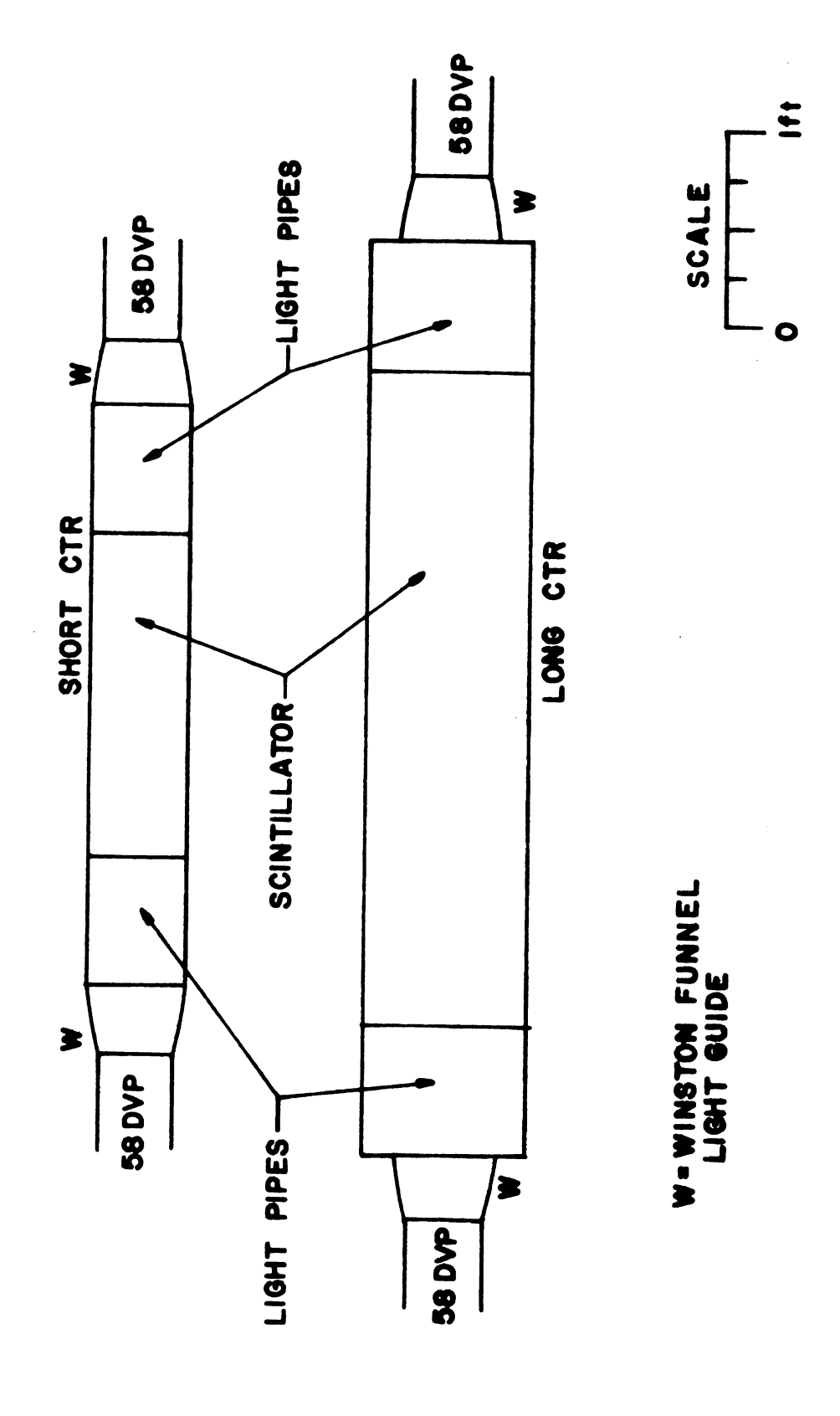


Figure D-5. Neutron Counter Design.

APPENDIX E

PROTON MOMENTUM ANALYSIS

A field map of the proton spectrometer bending magnet was available in a one-inch, 3-dimensional grid for both central and fringe fields, covering a volume $36 \times 10 \times 100 \text{ in}^3$, with only 20 x 10 x 60 in³ covered by magnet pole tips and coils. For each grid point B_x , B_y , B_z were known. Overall bending power was $\int \vec{B} \cdot d\vec{l} = 770 \text{ kG-inches}$ with a central field of 16.5 kGauss.

One thousand monte carlo events with momenta 3-12 GeV/c were ray traced through the magnet: First the particle momentum and field entrance vector were specified; then the proton was stepped through the field allowing the local Lorentz force to alter the proton direction at each increment until the particle left the field and the exit vector was specified.

Then given entrance and exit vectors to the field, an empirically determined 14-term polynomial was used to reproduce the proton momentum from the ray trace events, which it did to 1.5% full width at half maximum. 44 The polynomial was then used to compute the proton momentum from the experimental spark chamber tracks. A description of the polynomial is presented in Table E-1 and Figure E-1.

Table E-1. Polynomial for Proton Momentum Determination

Terms:	Terms:
1) 596.2/DS	8)00362(XI·X0) ² /DS
2) $189(XMPI + XMPO)^{2}/DS$	9)3531(X0) ² /DS
3) 2.244(XMPI + XMPO)/DS	10)1217(XI·YI·YO)/DS
4) .01249(X0·Y0) ² /DS	11) -201.5(XMPI - XMPO) ² /DS
5) .01921(YMPI + YMPO) ² /DS	12)00005841(XI) ⁶ /DS
6) .008411(XI) 4/DS	13) -3.635
7) .1078(XI·XO)/DS	14) 2.292(Y0) ²

Terms 13 and 14 are used only if |YO| > 3".

DS =
$$\frac{\text{XMPI-XI}}{\sqrt{(\text{XMPI-XI})^2 + (30)^2}} - \frac{\text{XO-XMPO}}{\sqrt{(\text{XO-XMPO})^2 + (30)^2}}$$

$$(\text{XMPO,YMPO})$$

$$(\text{XMPI,YMPI})$$

$$(\text{XI,YI})$$

$$(\text{XO,YO})$$

$$\text{SPECTROMETER BENDING}$$

$$\text{MAGNET}$$

Figure E-1. Polynomial Coordinates

INCIDENT PROTON

APPENDIX F

FERMI MOMENTUM CONSIDERATIONS

The main sources of bound protons in the glycol target are carbon and oxygen nuclei. Using a simple Fermi Gas approach, 45 one calculates the average momentum of a bound nucleon in the y (vertical) direction to be roughly 120 MeV/c (155 MeV/c is the maximum momentum).

The question of interest is whether or not we can separate free proton events from bound proton events experimentally. The neutron arm acceptance will allow detection of neutrons with momenta up to 930 MeV/c ($|t| \sim 1.0 (\text{GeV/c})^2$), and Fermi motion of a bound target proton can alter this appreciably.

If one considers the y-momentum balance constraint between the final state neutron and proton (a plot is shown in Figure 20(b))

$$\Delta p_{y} = \frac{p_{y}^{\text{neut}} + p_{y}^{\text{prot}}}{\sqrt{\frac{2}{\sigma_{\text{pyn}}^{2} + \sigma_{\text{pyp}}^{2}}}}$$
neut, prot are the y-momentum components of the neu-

where p_y^{neut} , p_y^{prot} are the y-momentum components of the neutron and proton, and σ_{pyn} , σ_{pyp} are their respective errors, one can estimate how Fermi motion effects will distribute events.

If we consider an event at $|t| = 1.0 (\text{GeV/c})^2$ for which $\sigma_{\text{pyn}} = 15 \text{ MeV/c}$ and $\sigma_{\text{pyp}} = 5 \text{ MeV/c}$, and consider the average Fermi momentum allowed the target (120 MeV/c), then

 $\Delta p_y = \pm 8 \, \sigma$ where σ is the standard deviation of Δp_y . Hence the events produced from bound protons will produce a broad smear across the range of Δp_y distinguishing them from the elastic events peaked within $\pm 2 \, \sigma$. Data obtained with the graphite dummy target and shown in Figures 20(b), 21 (a-b) bear out this expectation.

APPENDIX G

THEORY APPENDIX

If one considers a helicity amplitude for a particle exchange $m_{\lambda\mu}^{\rm ex}(s,t)$, where $\lambda=\lambda_3-\lambda_1$ and $\mu=\lambda_4-\lambda_2$ (helicity indices are shown in Figure 40, one may write it as an expansion over partial waves:

$$m_{\lambda\mu}^{\text{ex}}(s,t) = \sum_{J} (2J + 1) d_{\lambda-\mu}^{J}(z) m_{\lambda\mu}^{J \text{ex}}(s)$$

Using the Sopkovich prescription³³ for including elastic scattering yields a new total amplitude:

TOT
$$m_{\lambda\mu}(s,t) = \sum_{J} (2J + 1) d(z) m_{\lambda\mu}(s) S(s)$$

where S is the elastic S-matrix.

Now making the usual transformation: 46

$$\Sigma + \int_{0}^{\infty} P_{cms} db$$

$$J = P_{cms}b-1/2$$

is the total helicity flip defined on page 80, we obtain

$$\mathbf{TOT}_{\lambda\mu}(s,t) = \int_{0}^{\infty} (2P_{cms}b) P_{cms}db J_{\mathbf{n}}(b\sqrt{-t}) \mathbf{m}_{\lambda\mu}(s,b) S^{el}(s,b).$$

Then if one writes the formal expression:

$$m_{\lambda\mu}^{\text{TOT}}(s,t) = \int_{0}^{\infty} (2 P_{\text{cms}}^{2}) \text{ bdb } J_{\text{n}} (b \sqrt{-t}) m_{\lambda\mu}^{\text{TOT}}(s,b)$$

we get the prescription:

$$m_{\lambda\mu}^{TOT}(s,b) = m_{\lambda\mu}^{ex}(s,b) S^{el}(s,b)$$

where S^{el}(s,b) may be split into a piece with no scattering plus an interaction term:²

$$S^{el}(s,b) = 1 + \frac{i P_{cms}}{4\pi\sqrt{s}} m^{eff}(s,b)$$
hence $m_{\lambda\mu}^{TOT}(s,b) = m_{\lambda\mu}^{ex}(s,b) \left(1 + i \frac{P_{cms}}{4\pi\sqrt{s}} m^{eff}(s,b)\right)$.

What distinguishes the various models is their choice of Regge exchange amplitudes $m_{\lambda\mu}^{ex}(s,b)$ and effective rescattering amplitude $m^{eff}(s,b)$ presumably due to the Pomeron, elastic scattering corrections, etc.

1. Elastic amplitudes, meff(s,b)

Four main parametrizations were considered:

G-1 Elastic Absorption: 46

$$m^{eff}(s,t) = 4 P_{cms}^2 \sigma_T(i + \tilde{\rho}) e^{-At/2} \delta_{\lambda_1 \lambda_3} \delta_{\lambda_2 \lambda_4}$$

where A is the slope of the elastic cross section (~10) and $\tilde{\rho}$ is the ratio of real to imaginary parts in the elastic scattering (~30%). The delta functions emphasize that the pomeron flips no spins. The same will be true for all the other choices in this section and the δ 's will be dropped for convenience.

G-2 Worden Square Well: 35

$$m^{eff}(s,b) = \sum_{k=0}^{\infty} C_k A^{2k} \left(\frac{1}{A} \frac{d}{dA}\right)^k e^{-b^2/2A} \left(i + \tilde{\rho}\right)$$

G-3 Strong Cut (SCRAM-HKPR):², 3

$$m^{eff}(s,b) = 4P_{cms}^2 \lambda \sigma_T(i + \beta) e^{-At/2}, \lambda \stackrel{>}{\sim} 1.2 \text{ usually}$$

where λ is the estimate of contributions from diffraction elastic intermediate states (see Figure 41).

G-4 HKV: 36-38

$$m^{eff}(s,t) = P(s,t) + D(s,t)$$

where $P(s,t) = is(A_0e^{B_0t} + Ae^{Bt} J_0(R\sqrt{-t(ln\frac{s}{s_0} - i\frac{\pi}{2})})$ is the Pomeron and A_0 and A are related to σ_T by the optical theorem, and:

$$D(s,t) = is(A_2e^{B_2t} J_0(R_2\sqrt{-t(ln\frac{s}{s_0} - i\frac{\pi}{2})}) is$$

the contribution of the diffraction elastic intermediate states whose effect is entirely generated from the edge of the proton located at radius $R_2 \sqrt{\ln \frac{s}{s_0}}$.

2. Regge exchange amplitudes, $m_{\lambda,\mu}^{ex}$ (s,t):

Four different Regge prescriptions were used, each of which are listed below:

G-5 NWSZ:

The traditional form for the Regge amplitude which has periodic zeros in the denominator leading to non-sense wrong signature zeros:

$$\mathbf{m}_{\lambda\mu}^{\text{ex J}}(s,t) = (-t)^{\frac{N+x}{2}} \mathbf{g}_{\lambda 1 \lambda 3} \mathbf{g}_{\lambda 2 \lambda 4} (\frac{s}{s_0})^{\alpha_J} \frac{1 + \tau e^{-i\pi\alpha_J}}{\sin^2\alpha_J}.$$

G-6 Simplicity Choosing²

This is a form which has no forced amplitude zeros away from t=0 and is used in strong cut models:

$$m_{\lambda\mu}^{\text{exj}}(s,t) = \frac{(-t)^{\frac{N+x}{2}}}{(t-m_J^2)} g_{\lambda_1 \lambda_3} g_{\lambda_2 \lambda_4} \left(\frac{s-1/2 \, \text{Em}_{\text{ext}}^2}{S_0}\right)^{\alpha_J}$$

$$x \quad \exp(-i \frac{\pi}{2} \alpha_J^i \, (t-m_J^2))$$

G-7 V-M

This includes t -dependent vertex form factors to assist in fitting do/dt:

$$\begin{array}{l} \mathbf{m}_{\lambda\mu}^{\mathrm{ex}} \; (\text{s,t}) \; = \; \frac{(-\text{t})^{\frac{N+\mathbf{x}}{2}}}{(\text{t-m}_{J}^{2})} \; |\, \mathbf{g}_{\lambda_{1} \; \lambda_{3}} \; |\, \exp(\varepsilon_{\lambda}(\text{t-m}_{J}^{2})) \\ & \qquad \qquad \mathbf{x} \; |\, \mathbf{g}_{\lambda_{2}\lambda_{4}} \, | \; \exp(\varepsilon_{\mu}(\text{t-m}_{J}^{2})) \; (\frac{\text{s-1/2} \Sigma m_{\mathrm{ext}}^{2}}{S_{0}})^{\alpha_{J}} \end{array}$$

$$x \exp(-i \frac{\pi}{2} \alpha_J^! (t-m_J^2))$$

G-8 HKV³²

This form is numerically equivalent to G-6 with the exception of a slightly different energy factor.

$$\mathbf{m}_{\lambda\mu}^{\mathrm{ex}}(\mathrm{s},\mathrm{t}) = (-\mathrm{t})^{\frac{N+\mathbf{x}}{2}} \mathbf{g}_{\lambda_{1}\lambda_{3}}^{\lambda_{1}\beta_{2}\lambda_{4}} \left(\frac{\mathrm{s}}{\mathrm{s}_{0}} \mathrm{e}^{-\mathrm{i}\frac{\pi}{2}}\right)^{\alpha_{1}} \mathrm{e}^{\mathrm{i}\frac{\pi}{2}} \Gamma\left(\frac{\mathrm{J}-\alpha_{\mathrm{J}}}{2}\right).$$

All of these forms are equivalent when extrapolated to the particle poles (with the exception of a slight energy shift introduced by the term 1/2 Σ $m_{\rm ext}^2$, one-half of the sum of the external particle masses squared).

The factors $(-t)^{\frac{N+x}{2}}$ are for angular momentum and parity conservation; N and x are defined on page 80.

APPENDIX H

APPROXIMATE BEAM SPECTRUM

The raw beam spectrum for incident neutrons was not determined in this experiment. However based on the success of calculating the energy dependence of the differential cross sections, the spectrum is approximately that measured in a previous experiment^{5, 8} and shown in Figure H-1; the resolution in beam momentum determined from the present experiment is shown in Figure H-2.

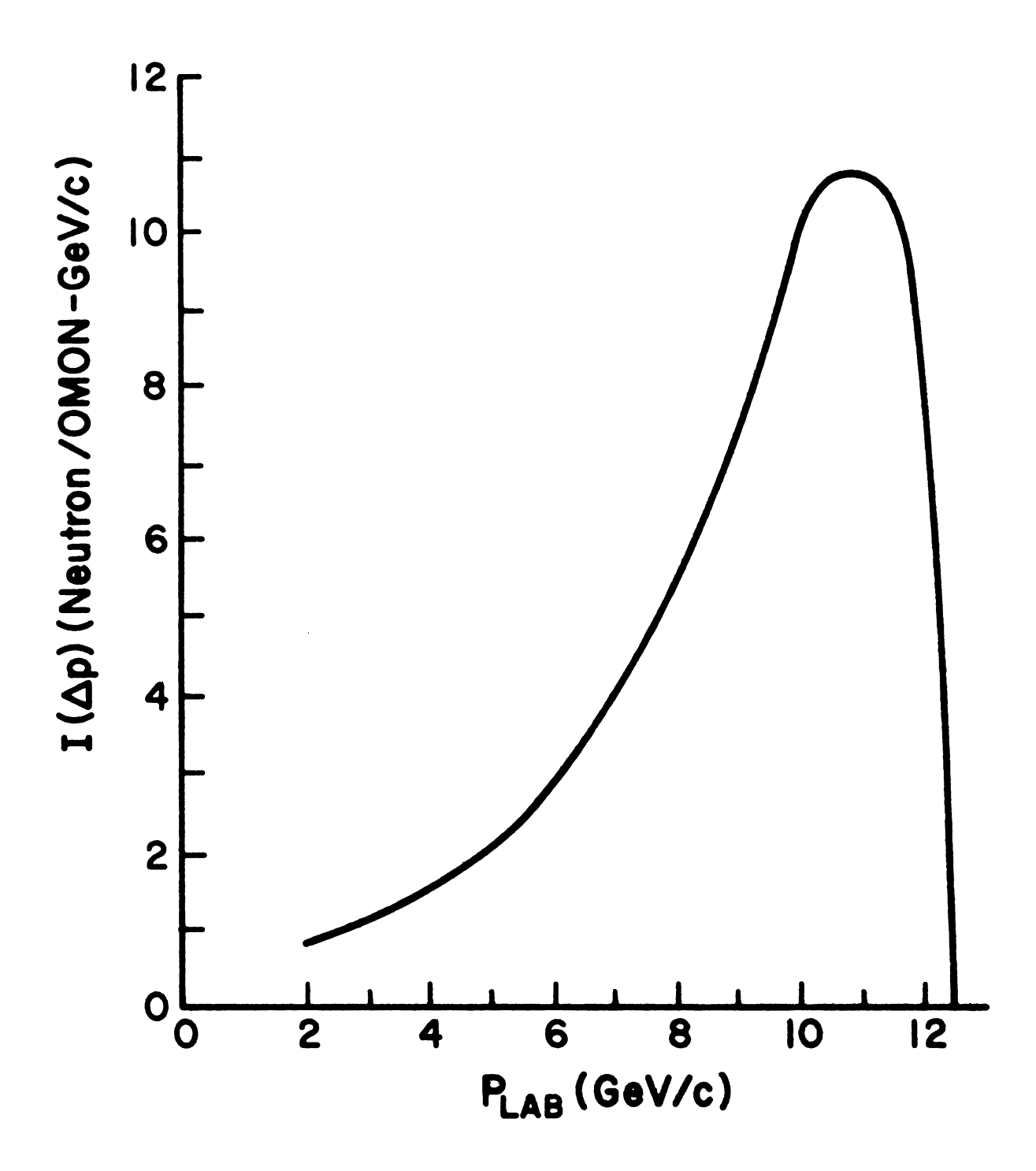


Figure H-1. Neutron Beam Spectrum, $I(P_{LAB})$.

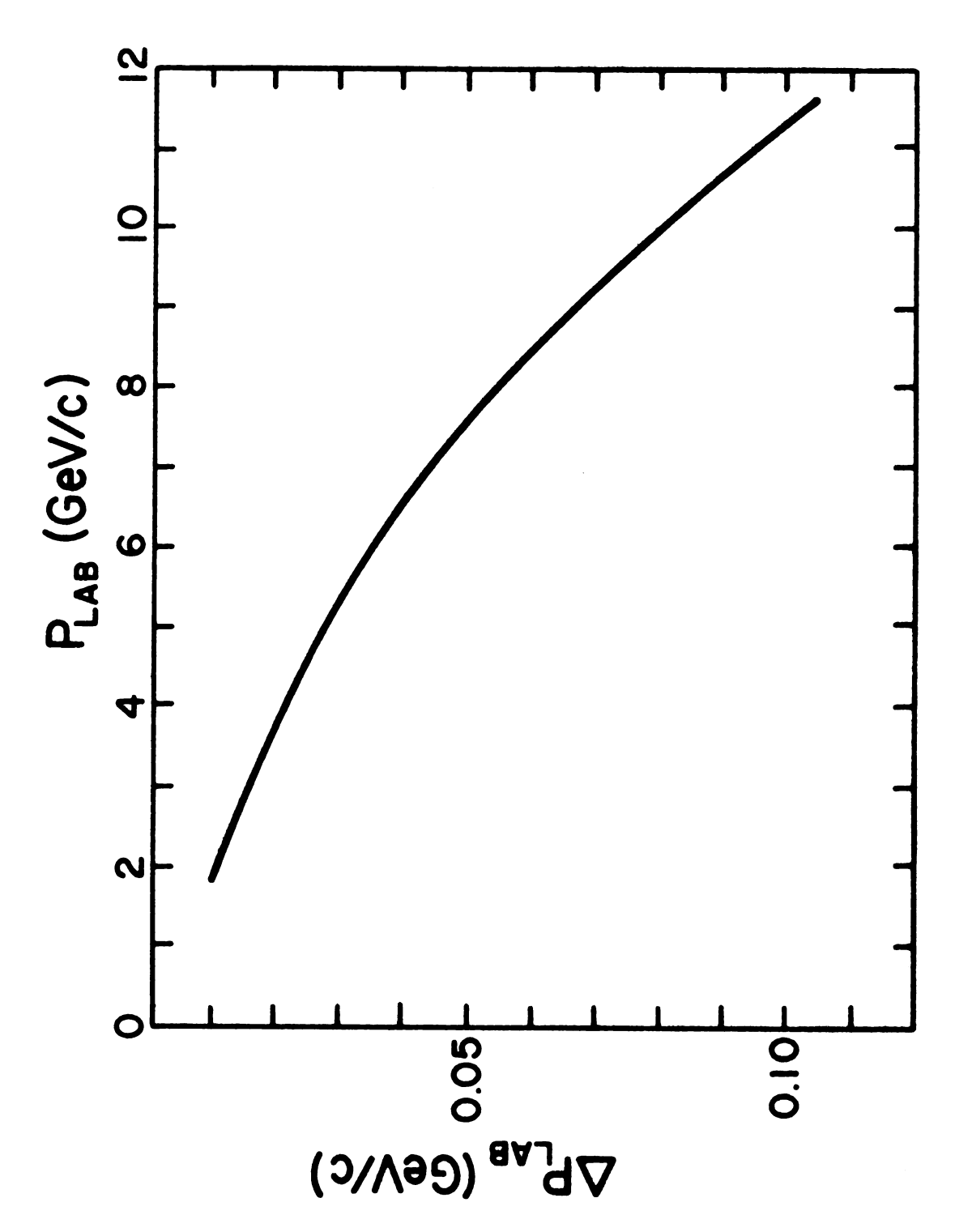


Figure H-2. Neutron Beam Resolution.

APPENDIX I

PPT-II FIELD MAP

A radial map of the field of the PPT-II magnet, measured in the horizontal, central plane at 25 kG field is shown in Figure I-1.

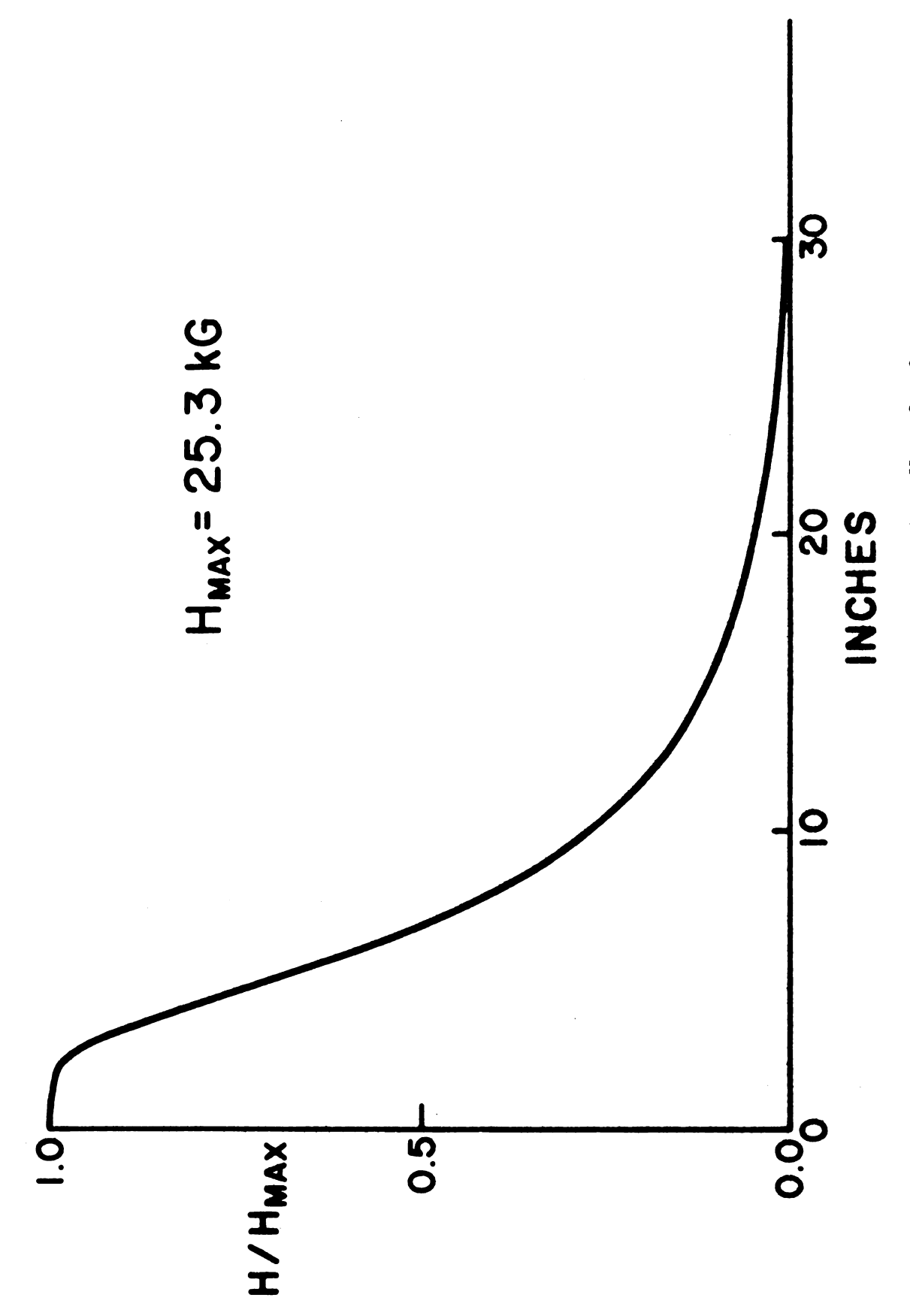


Figure I-1. PPT-II Magnetic Field Map for H = 25kG.



BIBLIOGRAPHY

- 1. P. R. Robrish, O. Chamberlain, R. D. Field, Jr., R. Z. Fuzesy, W. Gorn, C. C. Morehouse, T. Powell, S. Rock, S. Shannon, G. Shapiro, H. Weisberg, and M. J. Longo, Phys. Lett. 31B, 617 (1970).
- 2. F. S. Henyey, G. L. Kane, J. Pumplin, and M. H. Ross, Phys. Rev. <u>182</u>, 1579 (1969).
- 3. G. L. Kane, F. S. Henyey, D. R. Richards, M. H. Ross, and G. Williamson, Phys. Rev. Lett. 25, 1519 (1970).
- 4. M. H. Ross, F. S. Henyey, and G. L. Kane, Nucl. Phys. B23, 269 (1970).
- 5. E. L. Miller, M. Elfield, N. W. Reay, N. R. Stanton, M. A. Abolins, M. T. Lin, and K. W. Edwards, Phys. Rev. Lett. 26, 984 (1971).
- 6. Our internal target was also the extraction target for the external proton building EPB-I, allowing us to run compatibly with other experimenters.
- 7. The neutron beam is approximately the same as the one measured by the group in reference 5 and described in detail in reference 8.
- 8. E. L. Miller, Ph.D. Thesis, The Ohio State University, Columbus, Ohio (1971).
- 9. There is extensive literature on the Argonne PPT-II systems mainly in the form of preprints and unpublished leaflets, and these may be obtained from the Argonne Polarized Target Group under the direction of Dr. A. Yokosawa. For ease of reference in the text I have listed them individually in references 13-18.
- 10. B. Barnett, Ph.D. Thesis, University of Maryland, College Park, Maryland (1970).

- 11. M. Borghini, "Mechanisms of Nuclear Dynamic Polarization by Electron-Nucleus Dipolar Coupling in Solids", Second International Conference on Polarized Targets, Berkeley (1971).
- 12. H. Glattli, "Organic Materials for Polarized Proton Targets", Second International Conference on Polarized Targets, Berkeley (1971).
- 13. R. C. Niemann, F. S. Onesto, and O. J. Stover, Argonne Report ANL/HEP 6908 (1969).
- 14. D. Hill, R. C. Niemann, F. S. Onesto, and O. J. Stover, Operating Procedures for the ANL Polarized Target Mark II, Vacuum and Cryogenic Systems, (1971), unpublished.
- 15. R. C. Niemann, <u>Cavity</u>; <u>i.e.</u>, <u>Crystal Temperature Determination</u> (1968), unpublished.
- 16. A. Moretti and D. Hill, <u>Microwave System</u> (1970), unpublished.
- 17. J. J. Hill, Simple Dispersion Correction for Q-Meter Measurement of Proton Target Polarization (1972), unpublished.
- 18. G. E. Pake, <u>Paramagnetic Resonance</u> (W. A. Benjamin, New York, 1962), p. 35-38.
- 19. G. E. Pake, Op.Cit., pp. 41-42.
- 20. These values for the polarization include the effects of the real part of the susceptibility x', which introduces a small correction into the calculation, tending to equalize the values for positive and negative enhancement. For a detailed discussion see reference 17.
- 21. G. Burleson, D. Hill, S. Kato, P. F. M. Koehler, T. B. Novey, A. Yokosawa, D. Eartly, K. Pretzl, B. Barnett, A. Laasenen, and P. Steinberg, Phys. Rev. Lett. <u>26</u>, 338 (1971).
- 22. D. Hill, P. F. M. Koehler, T. B. Novey, B. Sandler, H. Spinka, A. Yokosawa, D. Eartly, K. Pretzl, G. Burleson, and H. Davis, Phys. Rev. Lett. 27, 1241 (1971).
- 23. D. Cheng, B. Macdonald, J. A. Helland, and P. M. Ogden, Phys. Rev. 163, 1470 (1967).

- P. R. Bevington, <u>Data Reduction and Error Analysis for the Physical Sciences</u> (McGraw-Hill, New York, 1969), p. 189.
- 25. P. R. Robrish, Ph.D. Thesis, University of California, Berkeley, California (1971).
- 26. M. Jacob and G. C. Wick, Ann. Phys. (N.Y.) 7, 404 (1959).
- 27. M. L. Goldberger, M. T. Grisaru, S. W. MacDowell, and D. Y. Wong, Phys. Rev. <u>120</u>, 2250 (1960).
- 28. J. Engler, K. Horn, F. Monnig, P. Schludecker, W. Schmidt-Parzefall, H. Schopper, P. Sievers, H. Ullrich, R. Hartung, K. Runge, and Yu. Galaktionov, Phys. Lett. 34B, 528 (1971).
- 29. M. B. Davis, B. G. Gibbard, M. N. Kreisler, T. Dobrowolski, M. J. Longo, D. D. O'Brien, T. Toohig, Phys. Rev. Lett. 29, 139 (1972).
- 30. A. Bohr and B. R. Mottleson, Nuclear Structure, Vol. I (W. A. Benjamin, New York, 1969), p. 4-5, and J. Hamilton and W. S. Woolcock, Rev. Mod. Phys. 35, 737 (1963).
- 31. H. Harari, Ann. Phys. (N.Y.) <u>63</u>, 432 (1971).
- 32. H. Harari, Phys. Rev. Lett. 26, 1400 (1971).
- 33. N. J. Sopkovich, Nuovo Cimento 26, 186 (1962).
- 34. The weak cut model was known to fail for the small t cross section and hence was not extensively used for any fits. However a considerable amount of work has been done in development of weak cut schemes -- some examples are E. K. Manesis, Argonne Report ANL/HEP 7214 (1972); R. C. Arnold; The Next Step in High Energy Phenomenology, Argonne Report ANL/HEP 6804 (1968); R. C. Arnold, Phys. Rev. 153, 1523 (1967); and reference 35.
- 35. R. Worden, Nucl. Phys. <u>B37</u>, 253 (1971).
- 36. G. L. Kane, Phys. Lett. <u>40B</u>, 363 (1972).
- 37. B. J. Hartley and G. L. Kane, <u>Toward a General Description of Two-Body Hadron Reactions</u>, <u>University of Michigan Preprint (1972)</u>, unpublished.
- 38. M. Vaughn and G. L. Kane, in preparation.

- 39. J. Froyland and G. A. Winbow, Nucl. Phys. <u>B35</u>, 351 (1971).
- 40. P. Astbury, G. Brautti, G. Finocchiaro, A. Michelini, D. Websdale, C. H. West, E. Polgar, W. Beusch, W. E. Fischer, B. Gobbi, M. Pepin, Phys. Lett. 23, 160 (1966).
- 41. J. G. Lee, A. Harckham, M. Letheren, W. Beusch, F. Bourgeois, E. Polgar, D. Websdale, K. Freudenreich, R. Frosch, F. X. Gentit, and P. Muhlemann, Nucl. Phys. <u>B52</u>, 292 (1973).
- 42. G. Barbiellini, M. Bozzo, P. Darriulat, G. Diambrini Palazzi, G. De Zorzi, A. Fainberg, M. I. Ferrero, M. Holder, A. McFarland, G. Maderni, S. Orito, J. Pilcher, C. Rubbia, A. Santroni, G. Sette, A. Staude, P. Strolin, K. Tittel, Phys. Lett. 39B, 663 (1972).
- 43. R. M. Edelstein, J. S. Russ, R. C. Thatcher, M. Elfield, E. L. Miller, N. W. Reay, N. R. Stanton, M. A. Abolins, M. T. Lin, K. W. Edwards, and D. R. Gill, Nucl. Instr. and Methods 100, 355 (1972).
- 44. The original work on the magnetic momentum analysis is contained in J. G. Horowitz, Masters Thesis, The Ohio State University (1969), unpublished.
- 45. A. Bohr and B. R. Mottleson, Op. Cit., p. 139-141.
- 46. B. E. Y. Svensson, CERN Report 67-24 (Vol. II), 1967.
- 47. G. Cohen-Tannoudji, Ph. Salin, and A. Morel, Nuovo Cimento 55A, 412 (1968).

